LOCALIZATION OF VENTRICULAR ACTIVATION ORIGIN USING PATIENT-SPECIFIC GEOMETRY

by

Shijie Zhou

Submitted in partial fulfilment of the requirements
for the degree of Doctor of Philosophy

at

Dalhousie University
Halifax, Nova Scotia
December 2017

I dedicate this work

to my wife Annie, and to my son Ethan

Table of Contents

List of Tables

List of Figures

Abstract

The clinical electrophysiological (EP) techniques of intracardiac recording and stimulation have emerged as invaluable tools for investigating and treating life-threatening cardiac arrhythmias. Computing technology plays a crucial role in making EP techniques possible. Two computational approaches designed to facilitate EP procedures are the subject of this dissertation: the first one is referred to as electrocardiographic imaging (ECGI); the second one is a novel statistical approach that enables a real-time guidance of the EP procedure based on the standard 12-lead ECG and a pace-mapping. Pre-ablation planning by means of ECGI can help to localize the origin of ventricular tachycardia (VT) and thus contribute to improving ablation-procedure outcome. The classical ECGI solves the inverse problem of electrocardiography by reconstructing epicardial potentials from multiple body-surface ECGs and patient-specific geometry of the heart and torso acquired by computed tomography. To overcome the inherent instability of the inverse problem, regularization methods must be used to constrain the solution. The present study assessed a data-driven Bayesian approach to the inverse solution that uses a novel algorithm for deriving dynamic spatio-temporal constrains for the solution. The encouraging results of validation experiments provide a strong incentive for pursuing the Bayesian method further. Next, a new statistical technique for real-time guidance of EP procedure was investigated. This technique supplements electroanatomic mapping—which provides patient's heart geometry—and it requires only the 12-lead ECG for a sufficient number of pacing sites with known coordinates to develop multiple linear regressions for predicting the origin of unknown activation sequence. The localization accuracy of the latter statistical method was superior to that achieved by the inverse solution and thus this approach to localizing the origin of ventricular activation offers an alternative to the pre-procedure inverse solution and its simplicity makes it practical for real-time applications.

List of Abbreviations and Symbols Used

3D – Three-dimensional

ACN – Adjusted Condition Number

AP – Action Potential

ARD – Automatic Relevance Determination

AV – Atrioventricular

BEM – Boundary Element Method

BSPM – Body Surface Potential Mapping

CART – Classification And Regression Trees

CC – Correlation Coefficient

CN – Condition Number

CT – Computed Tomography

DT – Decision Trees

ECG – Electrocardiogram

ECGI – Electrocardiographic imaging

EDL – Equivalent Double Layer

EGMs – Electrograms

EP – Electrophysiology

FOT – First-order Tikhonov (regularization)

FRA – Fastest Route Algorithm

GAT – Global Activation Time

ICD – Implantable Cardioverter Defibrillator

LAT – Local Activation Time

LBBB – Left Bundle Branch Block

Lead I – III – Standard limb leads of 12-lead ECG

LV – Left Ventricle

MAP – Maximum A Posteriori

MDCT – Multi-Detector Computed Tomography

MI – Myocardial Infarction

ML – Maximum Likelihood

MLR – Multiple Linear Regression

MRI – Magnetic Resonance Imaging

MSE – Mean Square Error

OOB – Out of Bag

P, Q, R, S, T – Nomenclature of the ECG waves

PTCA – Percutaneous Transluminal Coronary Angioplasty

PVCs – Premature Ventricular Contractions

R^2 – the coefficient of determination

RBBB – Right Bundle Branch Block

RBF – Radial Basis Function

RE – Relative Error

RF – Radio-Frequency (ablation)

RFR – Random Forest Regression

rms – Root Mean Square amplitude of a time-varying signal

RMSE – Root Mean Squared Error

RSS – Residual Sum of Squares

SA – Sino-atrial (node)

SBL – Sparse Bayesian Learning

SMAPE – Symmetric Mean Absolute Percentage Error

SNR – Signal-to-noise ratio

SOE – Sweep-operator Engine

SOT – Second-order Tikhonov (regularization)

SR – Sinus Rhythm

ST – ST segment of the ECG

SVR – Support Vector Regression

SVs – Support Vectors

TMPs – Transmembrane Potentials

V_1 – V_6 – Standard precordial electrode sites of the 12-lead ECG

VCG – Vectorcardiogram

VT – Ventricular Tachycardia

QEII – Queen Elizabeth II Health Sciences Centre

ZOT – Zero-order Tikhonov (regularization)

A – The matrix A

A^{-1} – Inverse of the matrix A

$A^{'}$ – Transpose of the matrix A

e – Euler's number

$\vec{J}$ – Current density vector

$\vec{E}$ – Electric field vector

I – Identity matrix

$\boldsymbol{n}$ – Outward unit normal of a surface

S_B – Outer surface of the torso

S_H – Closed heart surface

S_{H1} – LV endocardial surface

S_{H2} – RV endocardial surface

S_{H3} – Open epicardial surface

λ – Regularization parameter

mm – Millimeter

μs – Microsecond

μVs – Microvoltseconds

B – Volume conductor

Z_{BH} – Forward transfer coefficient matrix

∇ – Gradient operator

∇^2 – Laplacian operator

Γ – Potential gradients matrix

δ – Delta function

σ – Conductivity [Siemens m^{-1}]

ϕ – Electric potential [volt]

Φ – Vector of potential values

$d\Omega$ – Differential solid angle

Acknowledgements

It is my pleasure to acknowledge support, guidance and encouragement of my supervisor, Dr. Milan Horacek. My sincere gratitude goes to my clinical supervisor, Dr. John Sapp, to the members of my Supervisory Committee, Drs. Joshua Leon and Janie Wilson, and to Dr. Susan Howlett who provided challenging questions for my comprehensive exam. I greatly appreciate expert help of Jim Warren and Paul MacInnis, who were always there when I needed technical support and advice.

All members of the School of Biomedical Engineering—faculty, staff and students—have contributed to my positive graduate-student experience.

I am grateful to all those who assisted Dr. Sapp in the clinical studies, and I wish to extend my thanks and respect to patients who gave their consent to participate in those studies.

Last but not least, I wish to thank my broad family—my grandmother, my parents, and my parents-in-law—for their encouragement and attention. Above all, I thank my loving wife Annie for her support and love.

Financial support for my graduate program was contributed by the Nova Scotia Health Research Foundation (NSHRF), the Natural Sciences and Engineering Research Council of Canada (NSERC), the Faculty of Graduate Studies of Dalhousie University, the Nova Scotia Heart & Stroke Foundation (NSHSF), and by research grants awarded to Dr. Sapp by the Canadian Institutes of Health Researches and by Biosense Webster, Isracl.

Chapter 1

Introduction

1.1 The brief history of electrocardiography

Electrocardiography is a science and technology used daily in the clinical practice to record the electrical activity of the heart; these recordings are called *electrocardiograms* (ECGs). ECG recording is one of the most useful tests in modern medicine. In 1882, Augustus Waller obtained the first ECG, using his obliging dog Jimmy as a subject, and in May 1887 he recorded the first human ECG at the St Mary's Hospital in London. These early ECGs were recorded by using a capillary electrometer [1], which suffered from the poor frequency response caused by the heavy mercury column in the capillary. In 1895, Willem Einthoven—at the University of Leiden in Holland—refined the capillary electrometer, and then used a mathematical correction of the frequency response to predict P, QRS, T waves of the ECG as they are now known [2]. In 1901, Einthoven invented the string galvanometer, and one year later he recorded for the first time ECG tracings that show in real time the P, QRS, T waves [3]. The scheme for interpretation of ECGs—now called the Einthoven triangle—was introduced by Einthoven and his colleagues in 1913, and it is in clinical use to this date [4]. Einthoven's triangle represents the relationship between the heart's electric sources and field potentials under the assumption of a two-dimensional and infinite homogeneous medium surrounding the heart, represented by a single vector (electrical axis of the heart). In 1947, another Dutchman, Herman C. Burger, formalized a general theory of heart vector and lead vector that does not require restrictive assumptions regarding the volume conductor [5, 6, 7]. In the conventional clinical 12-lead ECG, there are six "unipolar" precordial leads (V1–V6) with electrodes placed on the chest, using the Wilson's central terminal (which approximates the potential at infinity) as a reference [8, 9]. The precordial leads view the heart's electrical activity in the transverse plane, perpendicular to the frontal plane of the Einthoven's triangle [10].

1.2 Genesis and interpretation of the electrocardiogram

Cardiac electrical activity can be represented by generators of bioelectric currents distributed in the heart region. The heart is a syncytial structure consisting of excitable muscle cells (cardiac myocytes); each cell undergoes an action potential (with a refractory period of different duration in different parts of the heart), followed by contraction. Fig. 1.1 (panel A) illustrates how the electrical excitation (depolarization followed by repolarization of individual cells) spreads as an activation wave through the entire heart; it starts at the sinoatrial (SA) node (pacemaker of the heart), spreads within 100 ms through atria, is delayed about 100 ms in the atrioventricular (AV) node, and spreads through the ventricular conduction system and ventricular muscle in about 100 ms; it takes about 300 ms for myocytes to repolarize. The activation wave front is an electrical double layer (with positive and negative side separated by about 1 mm) driving electrical current through the passive electrically conductive tissues surrounding the heart; Fig. 1.1 (panel B) illustrates the flow of electric current with the colored loops in a computer model of the human thorax [11]; these electric currents reach the body surface, creating time-varying potential differences that can be recorded as the ECGs.

In the 1950's, Durrer and van der Tweel studied excitation of the ventricular myocardium in dog and goat at the University of Amsterdam [13]. They used a plunge electrode to detect the passing activation wave front within the ventricular wall as shown in Fig. 1.2 (panel A). By inserting a large number of such electrodes at different locations in the ventricles, activity throughout the entire thickness of the ventricular wall could be recorded. Multi-channel recording allowed the exact time of a passing depolarization wave front to be detected (with reference to intracavitary electrode in the ventricles); this way, it was possible to reconstruct a three-dimensional (3D) isochronic map of ventricular depolarization. In 1968, Prof. Durrer's lab in Amsterdam studied 6 isolated human hearts, and published the composite findings in 1970 as a 3D isochronic map [14] that illustrates the activation of the human heart in Fig. 1.2 (panel B).

With the development of digital computers, it was possible to solve the forward problem of electrocardiography—defined as estimation of body-surface potential distribution from cardiac electrical sources—without the use of a phantom in 1964.

Miller and Geselowitz published a simulation of the ECG using multiple dipoles to illustrate the sequence of activation and the cardiac action potential for the normal heart as well as for infarction and ischemia in 1978 [15, 16]. In this laboratory at Dalhousie University, Leon and Horáček introduced a computer model of an idealized left ventricle to study excitation and recovery in anisotropic cardiac tissue [17, 18, 19]. This model had wall-thickness and fiber direction similar to that of the human heart. In 1998, Hren and co-workers at Dalhousie University demonstrated the role of fibrous structure in a 3D propagation model of the realistic human ventricular myocardium [20]. Fig. 1.3 (panels A and B) illustrates this realistic computer model of the human ventricular myocardium, which consisted of over 2 million cells, each with defined fiber direction (based on data from Auckland, New Zealand). In 2000, Simelius and co-workers simulated the ventricular activation based on Hren's realistic human heart [21] as shown in Fig. 1.3 (panel C). In this comparison of model simulations with isolated heart isochrones the right column in Fig. 1.3 (panel D) represents the ventricular activation of an isolated human heart as reported by Durrer and co-workers in 1970.

The clinical assessment of cardiac electrical function is usually performed by human interpretation of 12-lead ECG recordings, which is based on the vast experience of clinical electrocardiographers over many decades. The interpretation of ECG signals based on Maxwell's equations of electromagnetic theory constitutes the inverse problem of electrocardiography. The standard precordial leads over the thorax do not provide enough information for solving the inverse problem; therefore, with advancing electronic technology, body-surface potential mapping techniques were developed to provide a comprehensive view of non-invasively available information reflecting cardiac electrical activity [22].

1.3 Body-surface potential mapping (BSPM)

Body-surface potential mapping (BSPM) methodology has been evolving in this laboratory for over four decades. BSPM uses multiple electrodes (as many as 256) to record and measure cardiac electrical activity over the entire torso, providing a total time-varying potential distribution of heart-generated body-surface potentials. In our laboratory, Dalhousie standard torso grid is used to record 120-lead BSPM data

(Fig. 1.4).

To demonstrate how BSPM reflects the underlying electrical activity of the heart, we used mean potential values of 400 normal subjects. Figs. 1.5–1.8 show a sequence of measured body-surface potential maps corresponding to normal ventricular activation. Fig. 1.5 shows the body-surface potential distribution at the onset of the QRS complex at 0 ms. As the small initial wave front spreads thought the septum in a left to right direction in the heart, BSPM shows a maximum appearing on the right shoulder or in mid-sternal area and a minimum in a lower position on the left thoracic wall. During 4 ms to 34 ms of ventricular activation, phase I in Fig. 1.6, the minimum migrates dorsally and towards the right shoulder, finally appearing anteriorly in the right clavicular area, while the maximum moves downward to the left. We can imagine that initial activation wave front is in the interventricular septum, spreading throughout it, with a mean direction from base to apex. At this time, activation is spreading in an endo-epicardial direction through the walls of both ventricles. Later on, during the second phase of activation, as shown in Fig. 1.7, from 36 ms to 66 ms, a new minimum suddenly appears in the midsternal region and soon merges with the existing right-clavicular one to form a broad anterior negative region. Meanwhile, a new maximum moves towards the left thoracic wall and then dorsally. Ventricular activation continues as a wave front directed towards the apex by the Purkinje fibers, generating a leftward electrical force (because of a larger mass of the LV). Finally, at the phase III as shown in Fig. 1.8, during 68 ms to 98 ms, there are two positive areas; the sternal maximum can be attributed to late excitation of basal areas of the ventricles.

1.4 Electrocardiographic imaging (ECGI)

Body-surface potential mapping data non-invasively acquired from multiple thoracic sites can be used, along with a numerical model that accounts for the torso geometry and electrical properties, to reconstruct electrical events on the heart surface (epicardial or endocardial surface) by solving an inverse problem of electrocardiography. The inverse problem of reconstructing heart surfaces' potentials from body-surface potential measurements is often referred to as *electrocardiographic imaging* (ECGI). It requires—along with inverse-solution techniques—processed body-surface potential

mapping data, computational techniques for the forward calculation of body-surface potentials from heart-surface potentials, and a patient-specific anatomical representation of the epicardial or endocardial surface and outer torso surface [25, 26]. Patient-specific anatomical data have been increasingly made available by multi-detector computed tomography (CT or MDCT) and by magnetic resonance imaging (MRI). A pre-procedural thoracic computed tomography (CT) scan provides cardiac geometry and torso electrode positions in the same reference frame. The methodology of ECGI has already shown its potential, demonstrated in theoretical and experimental studies [27], and has been successfully applied in clinical studies [28, 29, 26, 30, 31].

There are currently two commercial ECGI systems along with electrode vests: CardioInsight (Medtronic Inc, Minneapolis, MN, USA) and EP Solutions (Yverdon-les-Bains, Switzerland). Recently, several papers addressed the clinical validation of these systems [32, 33, 34]. In spite of these advances, the inverse solution of electrocardiography remains a challenging problem; the search for a reconstruction approach which would deliver sufficiently accurate results with the highest clinical value is still on.

1.5 Clinical cardiac electrophysiology

Implantable cardioverter defibrillator (ICD) therapy is widely used for patients suffering from recurrent ventricular tachycardia (VT). Unfortunately, ICDs do not prevent the recurrence of VT [35]. The adverse prognosis and symptoms associated with ICD shocks drive the continued need to find ways to effectively suppress VT [36]. Radiofrequency (RF) catheter ablation has been demonstrated to be an effective treatment strategy to reduce recurrent scar-related ventricular tachycardia (VT) and related hospitalizations [35, 37, 38]. This therapy has recently been demonstrated to be superior to escalated antiarrhythmic-drug treatment for patients with prior myocardial infarction [39].

Three-dimensional (3D) electroanatomic mapping is a non-fluoroscopic mapping technique frequently used to study cardiac arrhythmias. The electroanatomic systems allow sequential acquisition of intracardiac electrical information at multiple anatomical locations within a chamber of interest, which enables reconstruction of the electroanatomic maps of the respective chamber. Two types of electroanatomic

mapping systems are in general use: Carto© (Biosense Webster, Diamond Bar, CA, USA) and EnSite™ (St Jude, St Paul, MN, USA), to localize cardiac electric sources and facilitate catheter navigation.

Localizing VT exit sites is a pre-requisite for the successful ablation of VT. A variety of methods have been developed to ablate VT. Point-by-point activation and entrainment mapping is effective in aiding ablation of inducible, hemodynamically tolerated VT, but is not applicable in the majority of patients; the majority of scar-related VTs are poorly hemodynamically tolerated, may be difficult to induce and frequently transform to other tachycardias during catheter mapping [40]. Three-dimensional substrate-based techniques are frequently the preferred alternative, since it may be advantageous to focus ablation efforts on abnormal tissue with the highest likelihood of being culprit substrate, typically including a significant patch of myocardial scar. These approaches may target specific regions of ventricular scar [41, 42], regions of arrhythmogenic isthmuses within the scar [40, 43], regions of local abnormal ventricular activity [44, 45, 46], discrete channels [43, 47, 48], or all low-voltage areas. Some investigators have attempted to homogenize the entire scar [49, 50], although this has not been proven to be superior to a strategy which focuses more specifically on all inducible VTs, and may diminish the amount of procedure time dedicated to higher yield sites within the scar. However, the procedure is restricted by the limitations of point-by-point catheter mapping, even with newer multipolar rapid mapping techniques. A common method for the identification of sites likely to participate in clinically relevant VTs is to create a 3D map of the arrhythmogenic substrate, induce VT, and identify portions of the scar which harbor exit sites. This depends upon rapid interpretation of the 12-lead ECG, sometimes combined with pace-mapping to identify areas from which the myocardium is activated. Efforts may then be focused on ablating the sites within the scar which are contiguous with the exit site. Rapid ECG interpretation requires significant expertise and could be facilitated with a computerized method to automatically locate the site of origin of ventricular activation.

1.6 Thesis organization

This dissertation is organized as follows:

Chapter 2 presents the required mathematical models of the forward-problem solution that are a prerequisite to solving the inverse problem. Two surface-source models, heart-surface potential and equivalent-double-layer (EDL) models are used to formulate the relationship of potential distribution on epicardial/endocardial surface to measured body-surface potential distributions.

Chapter 3 presents a novel hierarchical Bayesian approach to solving the inverse problem, using an automatic relevance determination (ARD) model to derive dynamic spatio-temporal *a priori* constrains. The Bayesian method was applied to 4 patients suffering from scar-related VT.

Chapter 4 presents an improved algorithm for evaluating the global activation time constructed from measurements of propagation delay for pairs of computed electrograms at neighboring locations. The new method to detect activation times was assessed by correlation with known activation maps obtained by contact mapping.

Chapter 5 presents a simplified method based on the properties of sparse representation of the equivalent-double-layer (EDL) model that employs a sparse Bayesian learning approach to the inverse solution, which makes use of the spatio-temporal features of the cardiac action potential to localize the origin of LV activation from body-surface potentials. The approach was applied to 3 patients with healthy myocardium to localize the origin of the pacing site on the left-ventricular endocardial surface.

Chapter 6 further explores the regression model using the generic LV geometry introduced previously and seeks new methods of localization performance from the 12-lead ECG in the generic LV geometry. In particular, two machine-learning methods are assessed with regard to their localization performance based on the generic LV geometry.

Chapter 7 compares the localization performance of two approaches: (1) The classical inverse solution of Tikhonov type reconstructing cardiac potentials using BSPM data and patient-specific geometry obtained from CT imagines, and; (2) The intra-procedure statistical method, requiring only the 12-lead ECG for pacing sites with known origin and patient-specific geometry of the endocardial/epicardial surface obtained by electroanatomic mapping. For 7 patients undergoing cardiac mapping and

simultaneous 120-lead BSPM, the pre-procedure method was compared to localization performance using the intra-procedure statistical method based on acquisition of 12-lead ECG for pacing sites with known location.

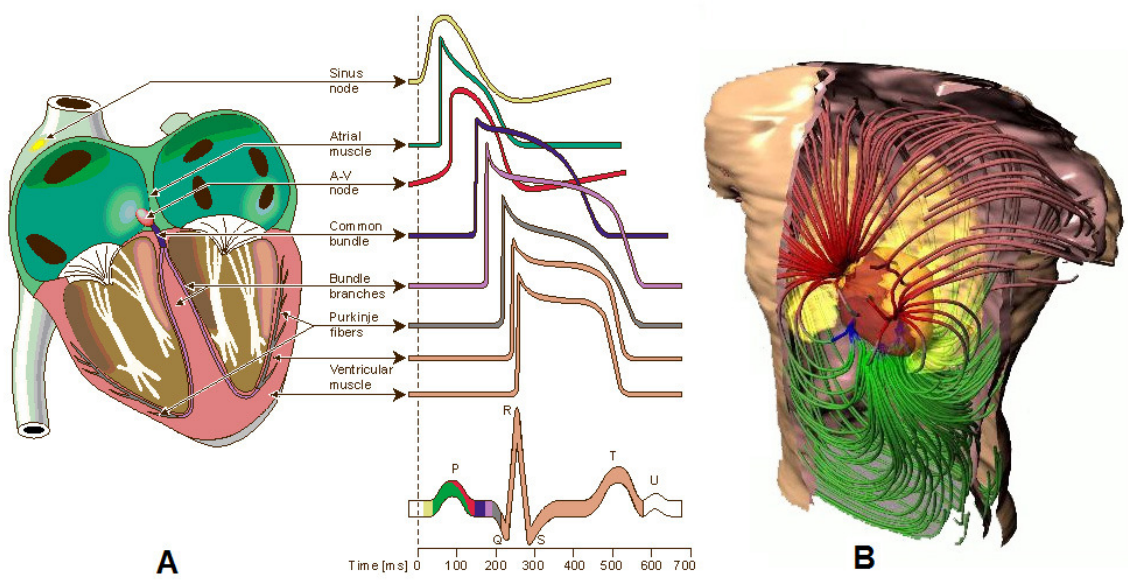

Figure 1.1: A: Electrophysiology of the heart. The different waveforms for each of the specialized cells found in the heart are shown [12]; B: A graphical representation of the geometry and electrical current flow in a model of the human thorax [11]

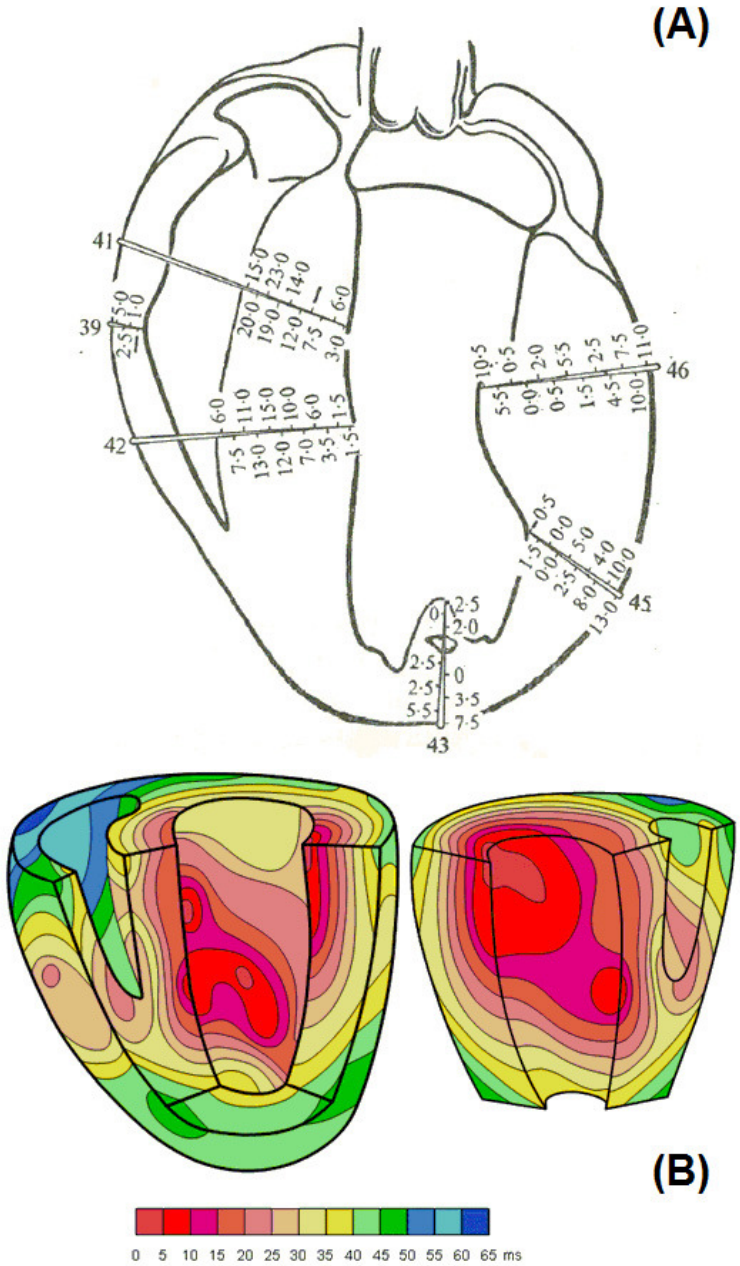

Figure 1.2: A: Durrer's measurement of isochronic surfaces of ventricular activation measurement. A section of ventricular wall of a dog heart showing approximate intramyocardial plunge electrodes for measuring the arrival times of the propagation wave front. B: 3D isochronic representation of the ventricular activation of an isolated human heart. Each color represents a 5-ms interval. Zero time is the beginning of the left-ventricular intracavitary potential [14].

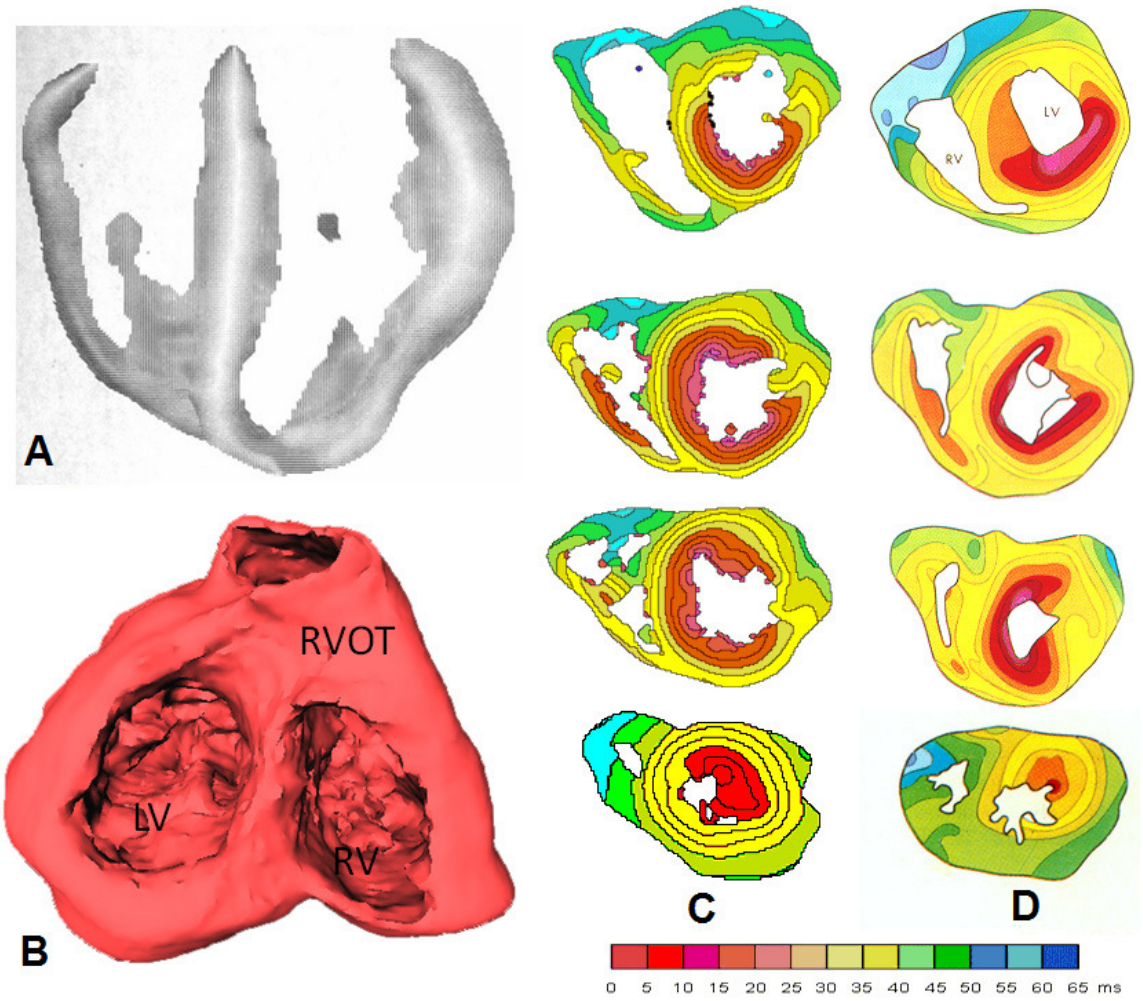

Figure 1.3: A: intramural white band in the realistic computer model indicates fibers running in the perpendicular direction to the section, B: the whole ventricular structure viewed from the base of ventricles (Note that only excitable myocardium is shown, less connective tissue, fat, etc.), C: corresponding simulated activation maps of ventricular activation sequence produced by Dalhousie heart model, D: the pattern of ventricular activation in a 3D presentation [14]; each color corresponds to a 5-ms interval. The isochronic surfaces show that activation starts from the endocardium of the LV and proceeds radially towards the epicardium.

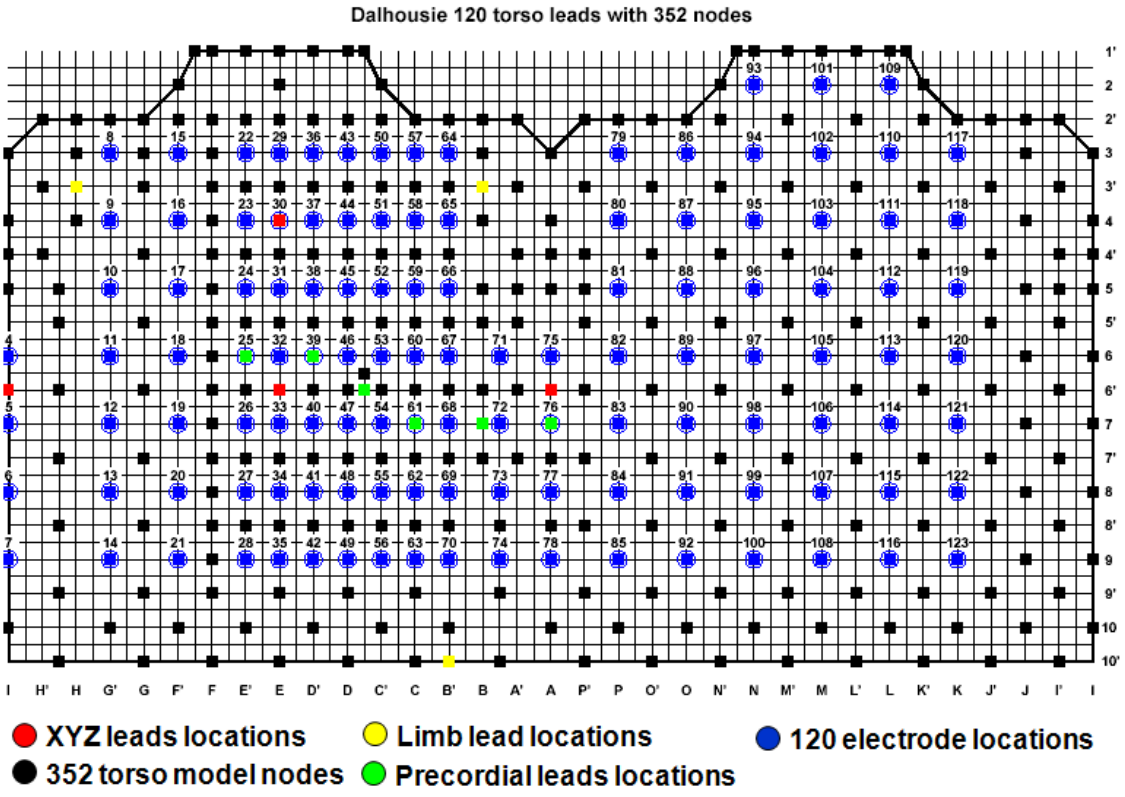

Figure 1.4: Dalhousie standard arrangement of 120 leads on the torso for BSPM. Left half represents anterior surface, right half the posterior surface of the chest. Transverse levels (labeled $1', 2, \ldots, 10'$) are 1-inch apart from neck to waist; potentials at 352 nodes (solid squares) are interpolated from potentials recorded at a set of 120 sites (blue circles); green squares indicate sites of precordial leads V1–V6; yellow squares mark sites where electrodes of Mason-Likar [23] substitution for extremity leads are placed; red squares are sites of EASI leads [24].

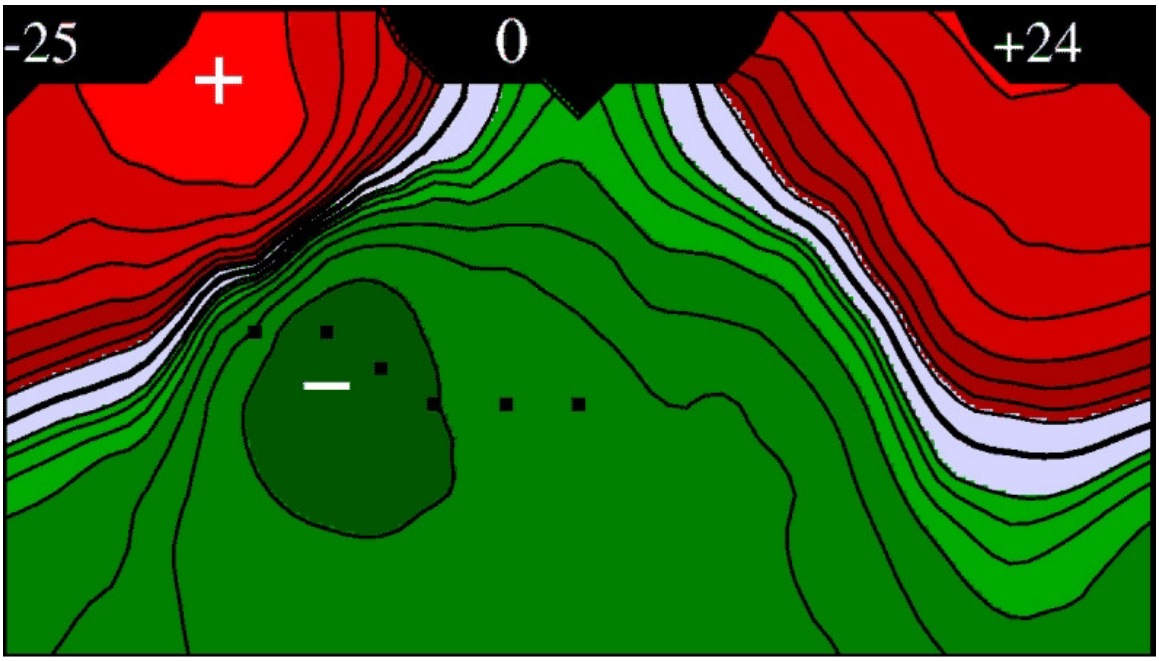

Figure 1.5: Body-surface potential map for normal human heart activation. The Phase 0 of ventricular activation is at the onset of QRS complex at 0 ms.

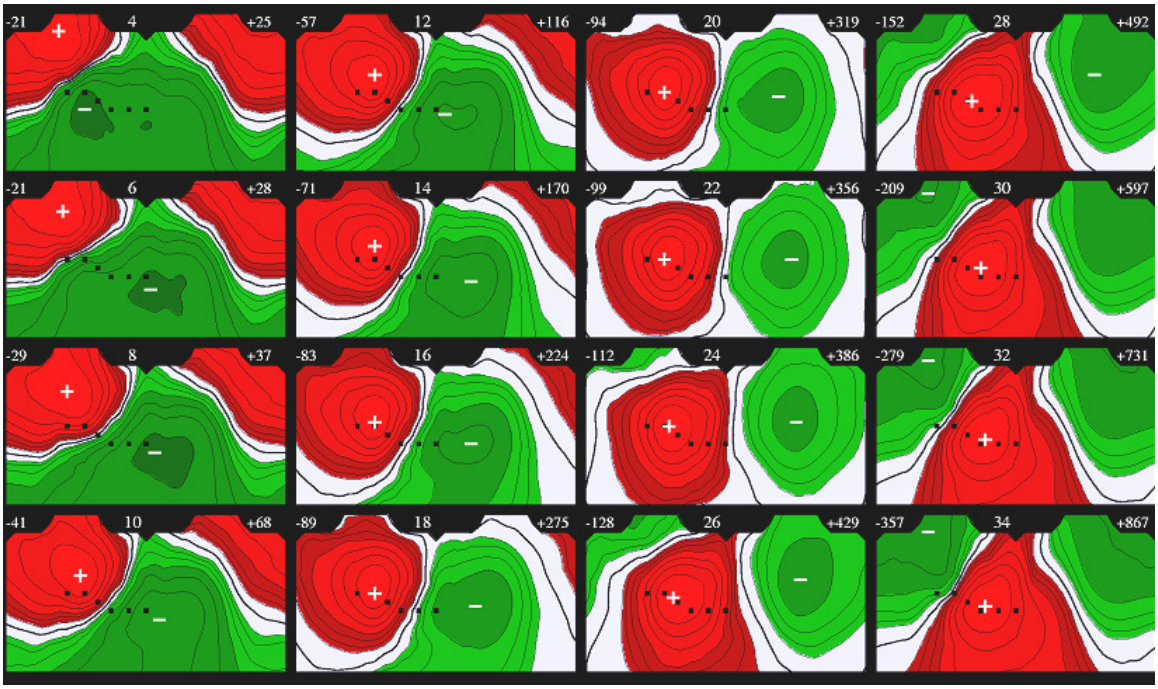

Figure 1.6: Body-surface potential maps for normal human heart activation. The Phase I of ventricular activation is from onset of QRS complex during 4 ms to 34 ms.

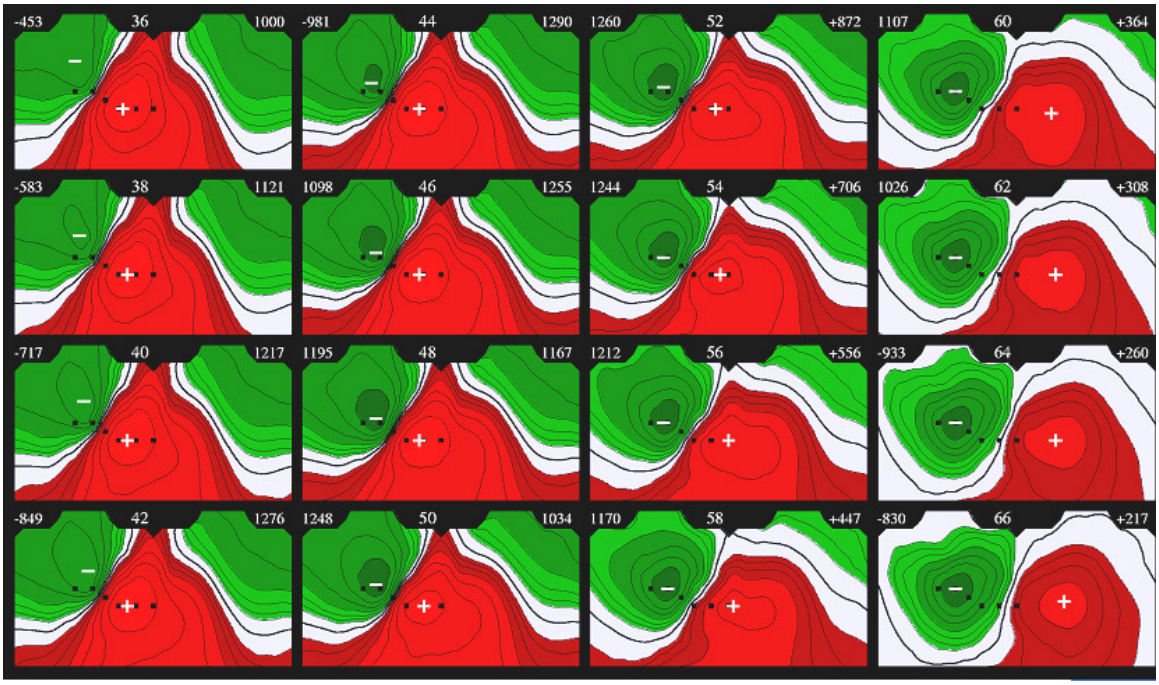

Figure 1.7: Body-surface potential maps for normal human heart activation. The Phase II of ventricular activation is from 36 ms to 66 ms.

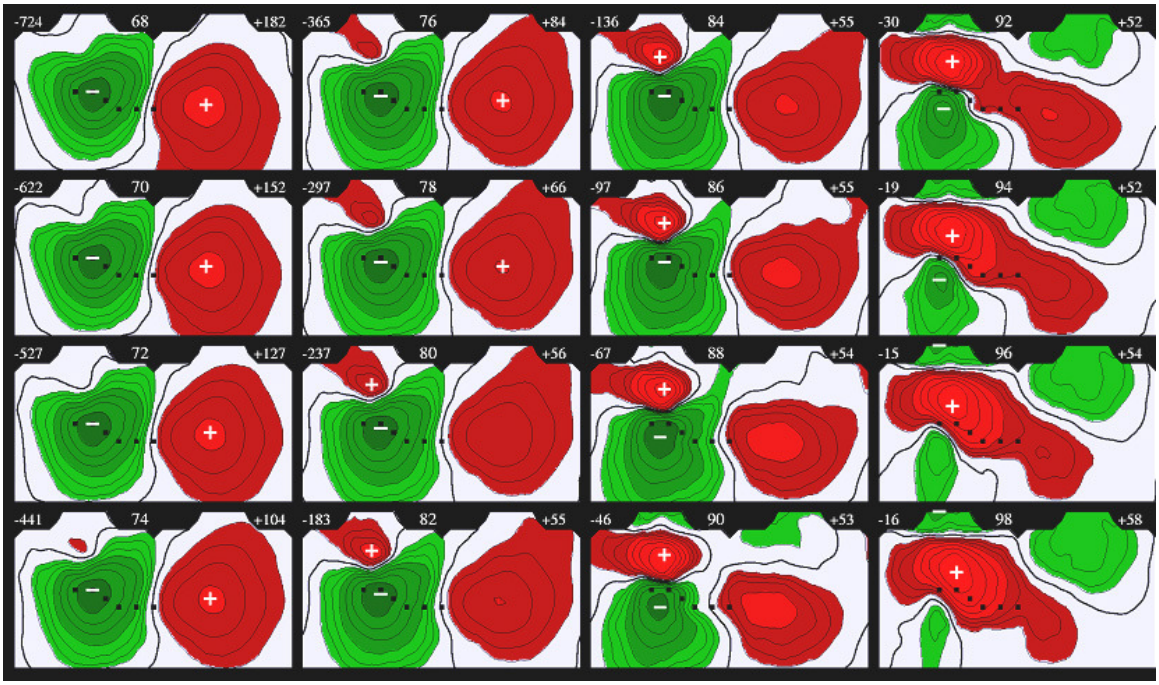

Figure 1.8: Body-surface potential maps for normal human heart activation. The Phase III of ventricular activation is from 68 ms to 98 ms.

Chapter 2

The Forward Problem of Electrocardiography

2.1 Introduction

In this chapter, the forward problem of electrocardiography is formulated as a calculation of body-surface potentials from epicardial or endocardial distributed sources, given patient-specific geometry obtained from CT imaging. Although the main purpose of clinical electrocardiography is to estimate the electrical activation of the cardiac sources via body-surface potential measurements, which is the so-called inverse problem of electrocardiography, the forward problem plays a fundamental role in determining the relationships between electrical sources within the heart and their body-surface potential manifestations on the torso.

Numerical methods for solving the forward problem of electrocardiography for arbitrarily-shaped volume conductors have been used since the 1960s [56, 57, 58]. The forward problem of electrocardiography is to compute, for given cardiac sources, the electric potential field within the torso and on the torso surface. The most frequently used distributed source models in electrocardiographic modeling are the electric-potential model [59, 60] and the equivalent-double-layer (EDL) model [61, 62, 63, 64]. Using the the potential theory and Green's theorem, we derived the source-field relationships between the torso surface and heart surface—or segmented heart surface—generating a forward transfer-coefficient matrices adopted in inverse-problem calculations.

2.2 Cardiac electric sources and the volume conductor

During the process of propagated excitation in the heart, the sources of electrical activity arise from the membrane currents of the individual cardiac cells. These sources can be summed up as an impressed current density $\vec{J}_i$ [57] distributed in the heart region, which is surrounded by the volume conductor that provides an electrical

load to these primary sources. The impressed current density and the volume current in the thorax are varying with time during the heart's activation sequence. The fundamental problem in electrocardiology is to estimate the relationships between the currents generated by the cardiac excitation and the potentials measured on the surface of the torso. We assume that the volume between the heart and the body surface is a homogeneous volume conductor with a constant value σ (Siemens/m), and that the volume conductor is electrically isotropic, which means the electrical conductivity at any point is a scalar quantity.

The potential distribution in the volume conductor changes with time and space, because of the spatial-temporal feature of the impressed current density. The capacitive and inductive properties of the tissues can be considered negligible in the frequency range of interest to electrocardiography (less than 1 kHz). Therefore, for all practical purposes, electromagnetic propagation effects can be neglected. In summary, the electrocardiographic forward problem can be seen as a quasi-static problem—for calculating potential distributions for time-varying current sources within a volume conductor, which is well approximated as linear, piecewise homogeneous, and isotropic.

Thus, in terms of Maxwell's equations, since the torso outside the heart region can be assumed to be resistive, and the relationship between current density ($\vec{J}$) and electric field ($\vec{E}$) can be considered linear,

$$\vec{J} = \sigma \vec{E}, \tag{2.1}$$

where σ is constant and represents conductivity at any point outside the heart volume. Since the spatial charge is neutralized almost instantaneously, neglecting the propagation effects, we assume quasi-static conditions to define the electric field as the negative gradient of a scalar potential ϕ:

$$\vec{E} = -\boldsymbol{\nabla}\phi. \tag{2.2}$$

The total current density $\vec{J}$ at any point in the volume conductor is equal to the sum of the impressed current density, $\vec{J_i}$, generated by cardiac sources, and conduction (ohmic) current density $\sigma\vec{E}$:

$$\vec{J} = \vec{J_i} + \sigma\vec{E}. \tag{2.3}$$

In this expression, $\sigma\vec{E}$ is the passive response in the volume conductor to the primary sources which are represented by $\vec{J}_i$. Furthermore, since $\vec{J}$ is solenoidal, the divergence of $\vec{J}$ forms closed loops of current flow. In other words, there is no net charge generated and the divergence of the current density vanishes, leading to

$$\boldsymbol{\nabla} \cdot \vec{J} = \boldsymbol{\nabla} \cdot (\vec{J}_i + \sigma\vec{E}) = 0. \tag{2.4}$$

Hence, the forward problem of electrocardiography is to calculate the extracardiac field from the given cardiac sources, which is governed by a Poisson's equation:

$$\boldsymbol{\nabla} \cdot \sigma\boldsymbol{\nabla}\phi = \boldsymbol{\nabla} \cdot \vec{J}_i. \tag{2.5}$$

2.3 Forward problem formulation

The forward problem solution is based on *Green's Second Identity* [65] that states that

$$\int_V (u\boldsymbol{\nabla}^2 v - v\boldsymbol{\nabla}^2 u)dV = \int_S (u\boldsymbol{\nabla}v - v\boldsymbol{\nabla}u) \cdot \boldsymbol{n}\, dS, \tag{2.6}$$

where the volume V is bounded by the surface S and $\mathbf{n}$ is the outward unit normal to S, dS is the scalar element of area of the integrating surface. We define the function u as $1/r$, where r is the distance from the source point $\boldsymbol{q}$ to an arbitrary field point $\boldsymbol{p}$, called the observation point, and the function v as the scalar electrical potential, ϕ. With these substitutions, the Green's identity becomes

$$\int_V \left[\phi\boldsymbol{\nabla}^2\frac{1}{r} - \frac{1}{r}\boldsymbol{\nabla}^2\phi\right] dV = \int_S \left[\phi\boldsymbol{\nabla}\frac{1}{r} - \frac{1}{r}\boldsymbol{\nabla}\phi\right] \cdot \boldsymbol{n}\, dS. \tag{2.7}$$

Consider a heart region H embedded in a homogeneous bounded volume conductor B, as in Fig. 2.1. The closed surface S_H is the union of the endocardial and epicardial surfaces of the left and right ventricles. S_B is the body surface and B the volume bounded by S_H and S_B.

Theorem 1. *In an infinite homogeneous conducting medium of conductivity σ in $\mathbb{R}^3$, the potential $U_\infty(\boldsymbol{p})$ at the field point $\boldsymbol{p}$ due to an elementary dipole source density $\vec{J}_i$ (which vanishes outside V) is given by*

$$\phi = U_\infty(\boldsymbol{p}) = \frac{1}{4\pi\sigma}\int_V \vec{J}_i \cdot \boldsymbol{\nabla}\frac{1}{r}dV \tag{2.8}$$

where $\boldsymbol{r} = \boldsymbol{q} - \boldsymbol{p}$, $r = |\boldsymbol{r}|$, $\boldsymbol{p}$ is the field point and $\boldsymbol{q}$ the source point.

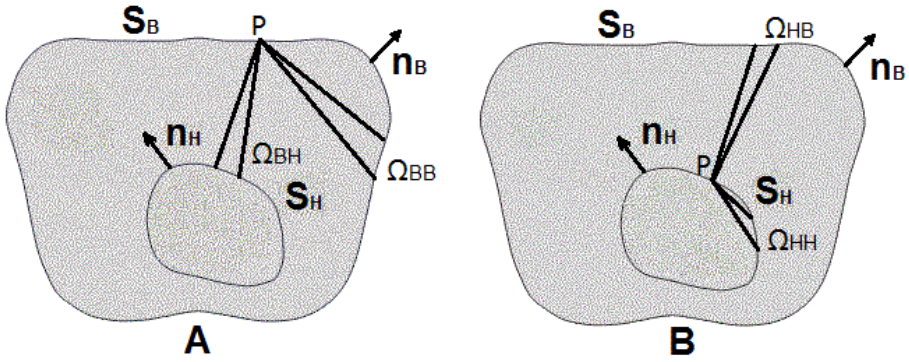

Figure 2.1: Transverse sketch of the torso and closed heart surface boundaries for the potential-based forward problem formulation. S_H and S_B are smooth surfaces with outward unit normals. A: the observation point P is located on the outer bounding body surface, S_B; B: P is placed on the inner bounding closed heart surface S_H. The Ω defines the solid angle.

The H region will strictly contain all "impressed" current sources, and a non-conducting boundary condition on the surface S_B will apply. There are no active sources outside the heart region, the right hand side of Eq. 2.5 can be set to zero in passive extracardiac domains, resulting in the Laplace equation

$$\boldsymbol{\nabla} \cdot \sigma \boldsymbol{\nabla} \phi = 0 \quad \in B. \tag{2.9}$$

This means that we now have

$$\boldsymbol{\nabla} \cdot (\sigma \boldsymbol{\nabla} \phi(\boldsymbol{p})) = \sigma \boldsymbol{\nabla}^2 \phi(\boldsymbol{p}) = 0 \qquad \boldsymbol{p} \in B, \tag{2.10}$$

for any field point $\boldsymbol{p}$ in B. The conductivity of air surrounding region B is zero ($\sigma = 0$), leading to normal component of current flow across outer torso boundary being

$$\sigma \boldsymbol{\nabla} \phi(\boldsymbol{p}) \cdot \boldsymbol{n}_B = 0 \qquad \boldsymbol{p} \in S_B, \tag{2.11}$$

where S_B is the human-torso surface bounding a homogeneous and isotropic volume conductor, and containing the heart region H, $\phi(\boldsymbol{p})$ is the electric potential at a field point $\boldsymbol{p}$, $\boldsymbol{n}_B$ is a unit normal oriented outward with respect to body surface S_B [59].

Theorem 2. *The solution to the forward problem (Eqs. 2.10 and 2.11) for $\boldsymbol{p} \in S$ is given by*

$$\phi(\boldsymbol{p}) = 2U_\infty(\boldsymbol{p}) - 1/2\pi \int_{S_B^-} \phi \boldsymbol{\nabla} \frac{1}{r} \cdot \boldsymbol{n} dS \tag{2.12}$$

with $\boldsymbol{r} = \boldsymbol{q} - \boldsymbol{p}$ *and* $r = |\boldsymbol{r}|$*, where* S_B^- *denotes the surface area excluding the singularity, that is, the integral is proper-valued and must be evaluated excluding the singularity at* $r = 0$*.*

Theorem 3. *The equivalent integral formulation for the following problem,*

$$\boldsymbol{\nabla} \cdot \sigma \boldsymbol{\nabla} \phi(\boldsymbol{p}) = \nabla \cdot \vec{J}_i = 0, \boldsymbol{p} \in B; \quad \boldsymbol{\nabla} \phi(\boldsymbol{p}) \cdot \boldsymbol{n}_B = 0, \quad \boldsymbol{p} \in S_B$$

is

$$\begin{aligned} c(\boldsymbol{p})\phi(\boldsymbol{p}) = &- \textstyle\int_{S_B} \phi \nabla r^{-1} \cdot \boldsymbol{n}_B dS - \int_{S_H} r^{-1} \nabla \phi \cdot \boldsymbol{n}_H dS \\ &+ \textstyle\int_{S_H} \phi \nabla r^{-1} \cdot \boldsymbol{n}_H dS, \end{aligned} \tag{2.13}$$

where $\boldsymbol{r} = \boldsymbol{q} - \boldsymbol{p}$ *(*$\boldsymbol{p}$ *is again the field point and* $\boldsymbol{q}$ *the source point) and* $r = |\boldsymbol{r}|$*,* $c(\boldsymbol{p}) = 2\pi$ *for* $\boldsymbol{p} \in S_B$ *and* $c(\boldsymbol{p}) = 4\pi$ *for* $\boldsymbol{p} \in B$ *and* $\boldsymbol{n}_B = \boldsymbol{n}$ *on* S_B *and* $\boldsymbol{n}_H = -\boldsymbol{n}$ *on* S_H*.*

2.3.1 Heart-surface potential model

Eqs. 2.10 and 2.11 state a boundary-value problem for Laplace's equation, which can be solved for any arbitrarily-shaped volume conductor by means of the boundary-element method (BEM), as the BEM formulation only requires a geometric representation of surfaces. The BEM method requires the application of Green's second identity (Eq. 2.7) to transform Eqs. 2.10 and 2.11 into an equivalent boundary-integral equation for the potential ϕ at any field point $\boldsymbol{p}$ on $S_B \cup S_H$ [59, 66]. The following derivation follows that of Horáček and Clements [60], which defines field potentials *directly* on surfaces with singularity removed from integration. Usually, we just consider a volume B bounded by body surface $S = S_B$ and closed epicardial surface S_H. To define the boundary condition between heart and body surfaces, we use the geometry of closed heart surface as a whole boundary to solve the Eqs. 2.10 and 2.11. From Theorem 3, the forward solution can be obtained by calculating the potential ϕ on the surface $S_B \cup S_H$, which gives

$$2\pi\phi(\boldsymbol{p}) = -\int_{S_B^-} \phi_B \boldsymbol{\nabla} \frac{1}{r} \cdot \boldsymbol{n}_B dS + \int_{S_H^-} \phi_H \boldsymbol{\nabla} \frac{1}{r} \cdot \boldsymbol{n}_H dS - \int_{S_H^-} \frac{1}{r} \boldsymbol{\nabla} \phi_H \cdot \boldsymbol{n}_H dS, \tag{2.14}$$

where S_B^- and S_H^- denote integration over the surfaces S_B and S_H, with the singularity removed; $dS = dS(\boldsymbol{q})$ is the differential of the integration surface; and the term

$\boldsymbol{\nabla}\frac{1}{r}\cdot\boldsymbol{n}dS = (1/r^3)\boldsymbol{r}\cdot\boldsymbol{n}dS$ is the incremental solid angle $d\Omega$, with $\boldsymbol{r} = \boldsymbol{q} - \boldsymbol{p}$ being the directed distance from the field point $\boldsymbol{p}$ to the source point $\boldsymbol{q}$ and $r = |\boldsymbol{r}|$.

To rewrite Eq. 2.14, two observation points are placed on $S_B \cup S_H$, respectively:

(1) Observation point i on S_B,

$$-\frac{1}{2\pi}\int_{S_H^-}\phi_H d\Omega^i_{BH} - \frac{1}{2\pi}\int_{S_H^-}\frac{1}{r^i}\nabla\phi_H\cdot\boldsymbol{n}_H dS_H + \frac{1}{2\pi}\int_{S_B^-}\phi_B d\Omega^i_{BB} - \phi^i_B = 0$$

(2) Observation point i on S_H,

$$-\frac{1}{2\pi}\int_{S_H^-}\phi_H d\Omega^i_{HH} - \frac{1}{2\pi}\int_{S_H^-}\frac{1}{r^i}\nabla\phi_H\cdot\boldsymbol{n}_H dS_H + \frac{1}{2\pi}\int_{S_B^-}\phi_B d\Omega^i_{HB} - \phi^i_H = 0$$

Here, $d\Omega^i_{PQ}$ is the solid angle subtended by elemental area of integration over the surface Q at an observation point i on the surface P.

We transform 2.14 in a discretized form, which can then be used to relate the potentials on the body surface to those on heart surface. These integrals can be given in its discretized form by

$$-\frac{1}{2\pi}\int_{S_H^-}\phi_H d\Omega^i_{BH} = \sum_{j=1}^{N_H} p^{ij}_{BH}\phi^j_H$$

$$-\frac{1}{2\pi}\int_{S_H^-}\frac{1}{r^i}\nabla\phi_H\cdot\mathbf{n}dS_H = \sum_{j=1}^{N_H} g^{ij}_{BH}\Gamma^j_H$$

$$\frac{1}{2\pi}\int_{S_B^-}\phi_B d\Omega^i_{BB} - \phi^i_B = \sum_{j=1}^{N_B} p^{ij}_{BB}\phi^j_B$$

and

$$\frac{1}{2\pi}\int_{S_B^-}\phi_B d\Omega^i_{HB} = \sum_{j=1}^{N_B} p^{ij}_{HB}\phi^j_B$$

$$-\frac{1}{2\pi}\int_{S_H^-}\frac{1}{r^i}\nabla\phi_H\cdot\mathbf{n}dS_H = \sum_{j=1}^{N_H} g^{ij}_{HH}\Gamma^j_H.$$

$$-\frac{1}{2\pi}\int_{S_H^-}\phi_H d\Omega^i_{HH} - \phi^i_H = \sum_{j=1}^{N_H} p^{ij}_{HH}\phi^j_H$$

where $\Gamma_H^j = \nabla\phi_H^j \cdot \boldsymbol{n}_H$, $j = 1, ..., n$. Therefore, the entire system of linear algebraic equations, written in the discretized equivalent forms based on $S_H \cup S_B$, is:

$$p_{HB}^i \Phi_B + p_{HH}^i \Phi_H + g_{HH}^i \Gamma_H = 0 \tag{2.15}$$

$$p_{BB}^i \Phi_B + p_{BH}^i \Phi_H + g_{BH}^i \Gamma_H = 0, \tag{2.16}$$

where i refers to a specific observation point on either the heart surface or the body surface. If we rewrite Eqs 2.15 and 2.16 for each point on the body and heart surface, two sets of equations result, which in matrix notation can be written as:

$$P_{HB}\Phi_B + P_{HH}\Phi_H + G_{HH}\Gamma_H = 0 \tag{2.17}$$

$$P_{BB}\Phi_B + P_{BH}\Phi_H + G_{BH}\Gamma_H = 0. \tag{2.18}$$

The approach to solving the system defined by Eqs. 2.17 and 2.18, which has been used by Barr *et al.* [59] has been to obtain the system

$$Z_{BH} = (P_{BB} - G_{BH}G_{HH}^{-1}P_{HB})^{-1}(G_{BH}G_{HH}^{-1}P_{HH} - P_{BH}), \tag{2.19}$$

where Z_{BH} is the transfer coefficient matrix that directly relates the heart-surface potentials to body-surface potentials. Once the matrix has been calculated, the forward problem can be solved by converting heart-surface potentials into body-surface potentials using simple matrix multiplication.

2.3.2 Equivalent Double Layer (EDL) model

The equivalent-double-layer (EDL) model introduced by Cuppen *et al.* [61] represents the sources by a layer of current dipoles on the closed ventricular surface. The forward transfer function $K(\boldsymbol{p}, \boldsymbol{q})$ can be computed from Theorems 1 and 2. Let $K(\boldsymbol{p}, \boldsymbol{q})$ be the body-surface potential at $\boldsymbol{p}$ due to a double layer element (i.e., elementary current dipole) at $\boldsymbol{q}$ on S_H and directed outward from S_H. Then it can be given by

$$\begin{aligned} K(\boldsymbol{p}, \boldsymbol{q}) &= 2U_\infty(\boldsymbol{p}, \boldsymbol{q}) - \frac{1}{2\pi}\int_{S_B} K(\boldsymbol{p}, \boldsymbol{q})\boldsymbol{\nabla}(1/r) \cdot \boldsymbol{n} dS \\ &= 2U_\infty(\boldsymbol{p}, \boldsymbol{q}) + \frac{1}{2\pi}\int_{S_B} K(\boldsymbol{p}, \boldsymbol{q}) d\Omega_{BB}. \end{aligned} \tag{2.20}$$

where $\boldsymbol{n}_B = \boldsymbol{n}$ on S_B and $\boldsymbol{n}_H = -\boldsymbol{n}$ on S_H, the term $\boldsymbol{\nabla}(1/r) \cdot \boldsymbol{n}\, dS = -(1/r^3)\boldsymbol{r} \cdot \boldsymbol{n}\, dS$ is the incremental solid angle $d\Omega$. Thus, for N source points $\boldsymbol{q}_j$ on S_H,

$$A = A_{i,j} = K(\boldsymbol{p}_i, \boldsymbol{q}_j), \quad i = 1, \ldots, M, j = 1, \ldots, N \tag{2.21}$$

is the potential at $\boldsymbol{p}_i$ due to an elementary source at $\boldsymbol{q}_j$ and A is the required transfer matrix. Based on Theorem 2, each A_{ij} is given by

$$-A_{i,j} + \sum_{k=1}^{M} p_{BB}^{ik} A_{kj} \approx 2U_{\infty}(\boldsymbol{p}_i, \boldsymbol{q}_j). \tag{2.22}$$

where $\sum_{k=1}^{M} p_{BB}^{ik}$ denotes the solid angle subtended by a differential of the integration surface S_B at the ith node $\boldsymbol{p}_i$ on the surface S_B. To deal with the singularity in the Eq. 2.22, the Wielandt deflation technique was used to reduce the singular system to a stable nonsingular system [67].

2.3.3 Segmented forward-transfer matrices

For a closed heart surface, as shown in Fig. 2.1, two covers of both cavities (representing mitral valve and tricuspid valve) can be constructed, generating left and right endocardial surfaces. Hence, the closed surfaces S_H can be divided into three independent parts illustrated in Fig. 2.2, which consists of LV endocardial surface S_{H_1} with N_1 nodes, RV endocardial surface S_{H_2} with N_2 nodes and epicardial surface S_{H_3} with N_3 nodes.

The forward problem of electrocardiography considered here is formulated as a calculation of the potentials $\Phi_B = (\phi_B^{1:t}, \ldots, \phi_B^{m:t})$ at M nodes on the body surface S_B from the observed electric potentials, $\Phi_H = (\phi_H^{1:t}, \ldots, \phi_H^{n:t})$ at N nodes on the closed heart surface S_H that consists of LV endocardial surface with N_1 nodes, right ventricular (RV) endocardial surface with N_2 nodes, and epicardial surface with N_3 nodes, where ": t" indicates the t-th time constant of the estimated cardiac source $\Phi_H^{:t}$ and the collected electrical field data $\Phi_B^{:t}$. A forward transfer matrix calculated by one of two source models can be discretized into three sub-matrices in terms of the coefficients which depend only on the geometry of S_B and S_H based on different boundaries with $S_{H_1} \cup S_B$, $S_{H_2} \cup S_B$ and $S_{H_3} \cup S_B$, giving for each $i = 1, \ldots, N$ on S_H and each $j = 1, \ldots, M$ on S_B.

2.4 Conclusions

In this chapter, we formulated two alternative solutions to the forward problem of electrocardiography based on two source models, given a patient-specific geometry.

We have shown how a forward transfer coefficient matrix calculated by these two source models can be partitioned into three sub-matrices by directly relating different segmented heart surface and body surface.

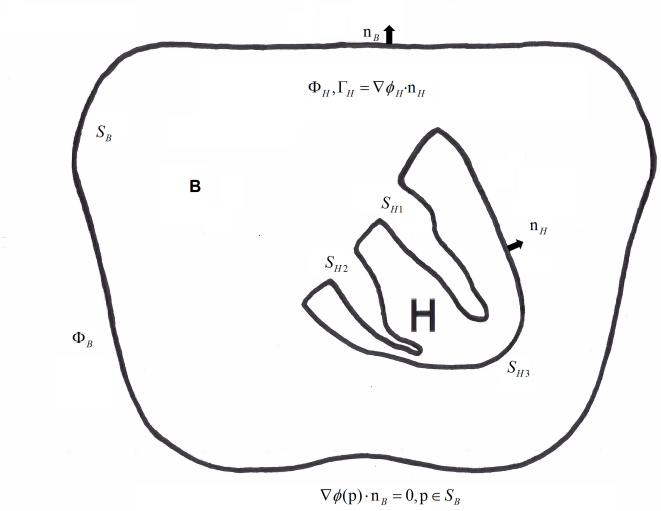

Figure 2.2: Transverse sketch of the torso and closed heart-surface boundaries for the potential-based forward problem formulation. B is the volume conductor region encompassing the region of cardiac sources H. The closed heart surfaces S_H that consists of left ventricular endocardial surface S_{H1}, right ventricular endocardial surface S_{H2} and open epicardial surface S_{H3}, and torso surface S_B are smooth surfaces with outward unit normals n_H and n_B

Chapter 3

Inverse Solution by Empirical Bayesian Method

3.1 Introduction

Catheter ablation of scar-related ventricular tachycardia (VT) has been demonstrated to reduce VT recurrence and thus it has become an effective treatment option, even though this therapy still faces challenges [42]. The main challenge of VT ablation procedure is to find the site of VT origin. To this end, pre-ablation planning of the electrophysiological procedures by ECG imaging (ECGI) [27] can be performed to estimate the site of origin of VT and thus contribute to improving ablation outcome [68]. The ECGI is a non-invasive technique that combines body-surface potential mapping (BSPM) with patient-specific geometry obtained from computed tomography (CT) or magnetic resonance imaging (MRI) to reconstruct epicardial potentials by solving the inverse problem of electrocardiography.

The inverse problem is mathematically ill-posed; therefore, various regularization algorithms have been applied to circumvent its ill-posedness. Usually, assumptions concerning either spatial and/or temporal properties of cardiac sources are used to constrain the solution space [26, 29, 55, 59, 69, 70, 71, 72, 73, 74, 75, 76]. Such *a priori* assumptions are often considered to be fixed, but a fixed *a priori* model often does not adequately predict complex spatio-temporal changes of cardiac sources under pathological conditions. Bayesian models can potentially overcome this limitation and they can be advantageously applied to solving the electrocardiographic inverse problem [77]. The earliest Bayesian study in electrocardiography was published by Martin and co-workers [78], who used statistical constraints to reconstruct the epicardial potential distribution over a 4-cm sphere surrounding the heart. Subsequently, Barr and Spach [79] presented a simplified probability model akin to zero-order Tikhonov regularization. In the late 1990s, several papers incorporated Bayesian concepts in reconstructing endocardial electrical activity from intracavitary potentials acquired by a multielectrode probe [80], and in visualizing cardiac arrhythmias [81]. In 1999,

van Oosterom utilized the maximum-a-posteriori (MAP) estimator to compute the epicardial potential distribution by assuming known *a priori* information (based on incorporating the spatial covariance of the epicardial potentials) [82, 83]. Greensite [84] used a data-driven approach to present an "Isotropy" condition that combines temporal and spatial constraints to estimate temporal and spatial covariances under certain restrictive assumptions; the method can be interpreted as learning the distribution of temporal waveforms of the solution — a type of empirical prior. A similar approach was later proposed by Erem and co-workers [85], who used a data-driven nonlinear dynamic parametrization, which offers a more flexible and stable representation of the temporal dynamics than the Isotropy method. The MAP was used to estimate the unknown epicardial potential distribution with a known *a priori* probability-distribution function by maximizing its *a posteriori* probability-density function in subsequent studies [86, 87, 88]. The method of Dössel and co-workers [89], based on the MAP, used QRS-integral features to localize the origin of premature beats; the MAP requires building a statistical basis for possible sources, which in its turn relies on certain assumptions about the source nature. Rahimi and co-workers [90] used Bayesian analysis to evaluate the impact of prior models by learning a prior of the p-norm distribution in transmural electrophysiologic imaging; they used an automatically adaptive set of models to deal with model-data mismatch and to achieve consistent performance in reconstructing sources with different spatio-temporal properties.

Modern Bayesian methodology does not attempt to select the "right" priors nor employ the fixed or known priors. Rather, *empirical prior* incorporating Bayesian concepts are used to describe flexible *a priori* distributions developed by learning from the particular system's properties in terms of a set of unknown hyperparameters that must be estimated from the data. To pragmatically learn *a priori* constraints, it is important to regularize the ill-conditioned problem of ECGI. In a real heart, initial pacing is more likely to fire neighboring nodes than those placed further apart, which means that initial cardiac propagation contains a small group of potentially relevant features for spatio-temporally changing properties of cardiac sources. With this in mind, one way to model local spatial connections of this type is to incorporate spatial smoothing in the form of an average window function into the prior distribution.

We propose a hierarchical Bayesian approach with a smoothing Automatic Relevance Determination (ARD) model [91] used to incorporate local spatial interactions on the epicardial surface. The smoothing ARD model determines the relevant features of cardiac sources, based on the temporal integral of the QRS complex extracted from BSPM data, to dynamically guide the search for appropriate spatio-temporal *a priori* constraints.

The aim of this chapter was to localize the origin of epicardial activation in patients who underwent epicardial pacing at known pacing sites or in patients who had VT with known exit sites. A spatio-temporal Bayesian approach was applied to solving this problem. We compared the performance of the Bayesian method with that of the ℓ_1-norm [55] and ℓ_2-norm (second-order Tikhonov [SOT]) methods in *in vivo* clinical studies and in *in silico* experiments.

3.2 Materials and Methods

3.2.1 Problem formulations

Let us assume that the body-surface potentials are sampled at M_y nodes for obtaining a temporal set of recordings at times $\Delta t_{t=1}^{T}$, where Δ is the sampling time interval and T is the total number of measurements in time. The relationship based on time series ($t = 1, \ldots, T$) between the measurement vector y and the epicardial sources x at N_x nodes is given by:

$$y_{:t} = Ax_{:t} + v_{:t} \quad t = 1, \ldots, T \tag{3.1}$$

where $y_{:t} \equiv [y_{1:t}, y_{2:t}, \ldots, y_{m:t}]'$ denotes the $M \times 1$ vector of potential measurements at all nodes of body surface at time t, and $x_{:t} \equiv [x_{1:t}, x_{2:t}, \ldots, x_{n:t}]'$ denotes the $N \times 1$ vector of cardiac electrical activity in all nodes of epicardial surface at time t; the apostrophe ' denotes the transpose; A is the transfer matrix between the epicardial-surface and the torso-surface potentials computed by the forward calculation using a quasi-static approximation from the Maxwell's equations; $v_{:t}$ represents modeling and measurement errors, independent from $x_{:t}$ for all time instants. Eq. 3.1 can be transferred into a time-integral linear system given by:

$$\bar{y} = A\bar{x} + \epsilon \quad \text{with} \quad \bar{x} = \sum_{t=1}^{T} x_{:t} \quad \text{and} \quad \bar{y} = \sum_{t=1}^{T} y_{:t}, \tag{3.2}$$

where ϵ is a measurement noise.

3.2.2 Forward calculation

The forward problem of electrocardiography is to compute for given cardiac sources the electric potentials within the torso and on the torso surface. In the present study, the heart-surface potential source model introduced in Chapter 2 was used to derive the transfer matrix A by solving the boundary-integral formulation of Laplace's equation in the source-free volume conductor between the epicardial and torso surfaces, using the boundary-element method (BEM) [92].

3.2.3 Inverse problem: ℓ_2-norm method

The conventional ECG inverse problem was used to estimate the cardiac source $\bar{x}$ in the Eq. 3.2 from the time-integral collected electrical field data $\bar{y}$ using Tikhonov regularization [93], which can be derived by minimizing an error function that combines data fit with a penalty defined by

$$\min_{\bar{x}}\{\|\bar{y} - A\bar{x}\|_2 + \lambda\|R\bar{x}\|_2\}, \tag{3.3}$$

where R is the regularizing operator, λ is the regularization parameter, and the subscript 2 means ℓ_2-norm used. The $\bar{x}$ can be estimated by minimizing the cost function 3.3. The first term of the Eq. 3.3 represents the reconstruction error named data fit, which measures the difference between the measured ECG signal and the reconstructed ECG data calculated from the estimated cardiac source. The second term places a penalty or constraint on the regularization method, depending on the choice of the regularization operator R. Also, choice of the penalty function affects the solution. Various regularization algorithms have been applied to the ECG inverse problem, mostly based on Tikhonov regularization that imposes ℓ_2-norm constraints. For the ℓ_2-norm solution, R is usually taken as the identity matrix (zero-order Tikhonov), the discretized gradient matrix (first-order Tikhonov), or the Laplacian differential matrix (second-order Tikhonov). Parameter λ is chosen by the L-curve [94] method, CRESO method [95] or Zero-crossing method [96]; λ controls a trade-off between fitting the data and minimizing the regularization term, which tunes the balance between stability of the solution and its capability to explain the measured data.

3.2.4 Inverse problem: ℓ_1-norm method

The ℓ_1-norm regularization method is to penalize the ℓ_1-norm of the gradient function which is based on the normal derivative of the epicardial surface potentials. The cost function is given by:

$$\min_{\bar{x}}\{\|A\bar{x}-\bar{y}\|_2+\lambda\|\frac{\partial\bar{x}}{\partial n}\|_1\}, \tag{3.4}$$

where λ is the regularization parameter, and the subscript 1 indicates ℓ_1-norm. The normal derivative of the epicardial surface potentials can be derived to relate a normal derivative matrix F with epicardial surface potentials:

$$\frac{\partial\bar{x}}{\partial n}=F\bar{x}. \tag{3.5}$$

Therefore, the cost function can be expressed as:

$$\min_{\bar{x}}\{\|A\bar{x}-\bar{y}\|_2+\lambda\|F\bar{x}\|_1\}, \tag{3.6}$$

where the normal derivative matrix F can be derived from the geometric relationship between the epicardial-surface potentials and the body-surface potentials, given by $F=-G_{HH}^{-1}P_{HH}$ solved in Chapter 2, where P_{HH} represents the solid angles on the epicardial surface, and G_{HH} is the gradient of heart potentials on the epicardial surface (see the details in Chapter 2). Ghosh, *et al.* [55] presented an iterative method to calculate non-linear Eq. 3.6 because of non-differentiability of the ℓ_1-norm penalty function.

To solve the non-differentiability of the ℓ_1-norm penalty function in Eq. 3.6, an estimated solution can be obtained by [55]:

$$\bar{x}=(A'A+\lambda F'WF)^{-1}A'\bar{y}, \tag{3.7}$$

where W is the weight matrix of $\bar{x}$, and $F=-G_{HH}^{-1}P_{HH}$ is equal to the normal derivative. The diagonal weight matrix W is obtained by:

$$W=\frac{1}{2}(\frac{1}{\sqrt{(\|F\bar{x}\|_1+\zeta)}}), \tag{3.8}$$

where ζ is a small positive constant chosen 10^{-5}, which can guarantee that the denominator of each element in the W is nonzero. The ℓ_1-norm of $F\bar{x}$ was simplified

to choose the maximum from the absolute sum of each column of $F\bar{x}$, which is given by:

$$\|F\bar{x}\|_1 = \max_{1\leq j\leq N} \sum_{j=1}^{N} |H_{ij}|, \tag{3.9}$$

where H_{ij} is element locating in ith row and jth column of $F\bar{x}$.

3.2.5 Inverse problem: empirical prior Bayesian method

Bayesian Theorem

Since a classic regularization framework provides us only with a single deterministic solution (such as that obtained by the Tikhonov-type methods), a principal focus of ECGI investigations shifted recently to obtaining a whole distribution of solutions. Given the stochastic nature of noise affecting the data, it is natural to view inverse problems as statistical inference problems. The model uncertainty problem has been widely treated in the Bayesian literature in the last decade. Meanwhile, several solutions have been proposed and applied in many other fields of scientific research. The ill-posed inverse problem can be tackled by using Bayes' theorem. The core of this approach is to model the data as a random variable. Therefore, the Bayesian approach would not only provide us with a maximum likelihood (ML) framework to estimate the probability distribution of the data when the unknown is viewed as a set of parameters, but also with an entire probability distribution that we can evaluate to study sources of uncertainty, given the data.

In the Bayesian framework, on the other hand, $\bar{x}$ is viewed as the realization of the random variable rather than as a parameter, and it is given a prior distribution; this prior is then combined with the likelihood through Bayes theorem to produce the so called posterior distribution, *i.e.*, the probability distribution for the unknown, conditioned on the realization of the data. The solution of the inverse problem is here defined to be the posterior distribution of the unknown, which can then be used to compute point estimates and bounds. More specifically, let $p(\bar{x})$ be the prior probability distribution for the unknown, embedding all the information which is known *a priori*, before the data are collected; let $p(\bar{y}|\bar{x})$ be the likelihood function, the same function that is used in the maximum likelihood framework; the posterior

distribution is given by Bayes theorem as

$$p(\bar{x}|\bar{y}) = \frac{p(\bar{y}|\bar{x})p(\bar{x})}{p(\bar{y})}. \tag{3.10}$$

Let us briefly consider a linear inverse problem with additive zero-mean Gaussian noise ϵ, with standard deviation δ. In the ML framework, the likelihood function is

$$p(\bar{y}|\bar{x}) = \frac{1}{\sqrt{2\pi}\delta} \exp(-\frac{\|\bar{y} - A\bar{x}\|^2}{2\delta^2}). \tag{3.11}$$

In Bayesian terms, the posterior distribution under zero-mean Gaussian prior for the unknown turns out to be:

$$p(\bar{x}|\bar{y}) \propto \exp(-\frac{\|\bar{y} - A\bar{x}\|^2}{2\delta^2}) \exp(-\frac{\|\bar{x}\|^2}{2\eta^2}), \tag{3.12}$$

where η is the standard deviation of the prior. Comparison of equations 3.12 and 3.3 suggests that the minimizer of the Tikhonov functional is the mode of the posterior distribution. And the regularization parameter is identified with the ratio between the noise variance and the variance of the prior distribution $\frac{\delta^2}{\eta^2}$. Constraints are therefore applied to the problem by specifying probability distributions for the noise and sources, called *likelihood* and *prior* respectively. The parameters describing these two distributions will be referred to as the *hyperparameters* in the text. By adjusting the hyperparameters using the data in $\bar{y}$ the posterior probability can be determined, which specifies the most probable value for the sources.

Hierarchical Bayesian Method

We consider Eq. 3.2 consisting of M_y nodes with corresponding target measurement $\bar{y}$ and N-dimensional source vectors $\bar{x}$. For the probability distribution based on an empirical Bayesian framework, the posterior distribution can be used as representation of unknown sources given the measured $\bar{y}$,

$$p(\bar{x}|\bar{y}) = \frac{p(\bar{y}|\bar{x})p(\bar{x})}{p(\bar{y})}, \tag{3.13}$$

where the model evidence $p(\bar{y})$ is the marginal likelihood which is important for model comparison. The likelihood model $p(\bar{y}|\bar{x})$ is assumed to be Gaussian with a noise variance [97], which is given by

$$p(\bar{y}|\bar{x}) = (\frac{2\pi}{\beta})^{-M/2} \exp(-\frac{\beta\|\bar{y} - A\bar{x}\|^2}{2}), \tag{3.14}$$

where β is the reciprocal of the noise variance.

During the epicardial pacing, the activation is progressing smoothly from an initial node to its neighboring nodes, as shown in Fig. 3.1. For each node and its nearest neighbors a class is defined by a weighting function. The epicardial surface is divided into N_x overlapping classes centered around each source node. The parametric form of the proposed method's weight prior combines each source and its nearest neighbors as follows:

$$p(\bar{x}_i; \gamma_i) \propto \exp(-\frac{1}{2} \sum_{i=1}^{N} \gamma_i (\bar{x}_i^2 + \frac{1}{p_i} \sum_{j=1}^{p_i} (\bar{x}_j^*)^2)), \tag{3.15}$$

where for each source $\bar{x}_i (i = 1, \ldots, N)$, p_i is the number of neighboring sources $\bar{x}_j^*$. To find the normalization factor, the prior also can be rewritten as

$$p(\bar{x}_i; \gamma_i) \propto \exp(-\frac{1}{2} \sum_{i=1}^{N} (\gamma_i + \psi_i) \bar{x}_i^2), \tag{3.16}$$

where $\gamma_i + \psi_i$ are used to control each class of the sources $\bar{x}_i$ $(i = 1, \ldots, N)$ as groups of hyperparameters; the variable $\psi_i (i = 1, \ldots, N)$ is defined as an average of its closest neighboring sources, which is given by

$$\psi_i(\gamma_1^*, \ldots, \gamma_j^*; p_1^*, \ldots, p_j^*) = \frac{\gamma_1^*}{p_1^*} + \cdots + \frac{\gamma_j^*}{p_j^*}, \tag{3.17}$$

where $\gamma_j^* (j = 1, \ldots, p_i)$ defines the hyperparameters that are centered around the neighboring nodes $\bar{x}_j^*$ of $\bar{x}_i$, and p_j^* is the number of neighbors for each $\bar{x}_j^*$. The prior then takes the form

$$p(\bar{x}_i; \gamma_i, \forall i) \sim \mathcal{N}_{\bar{x}}(0, \Gamma) \tag{3.18}$$

where Γ is

$$\Gamma = \begin{bmatrix} \gamma_1 + \psi_1 & \cdots & 0 \\ \vdots & \ddots & \vdots \\ 0 & \cdots & \gamma_N + \psi_N \end{bmatrix}.$$

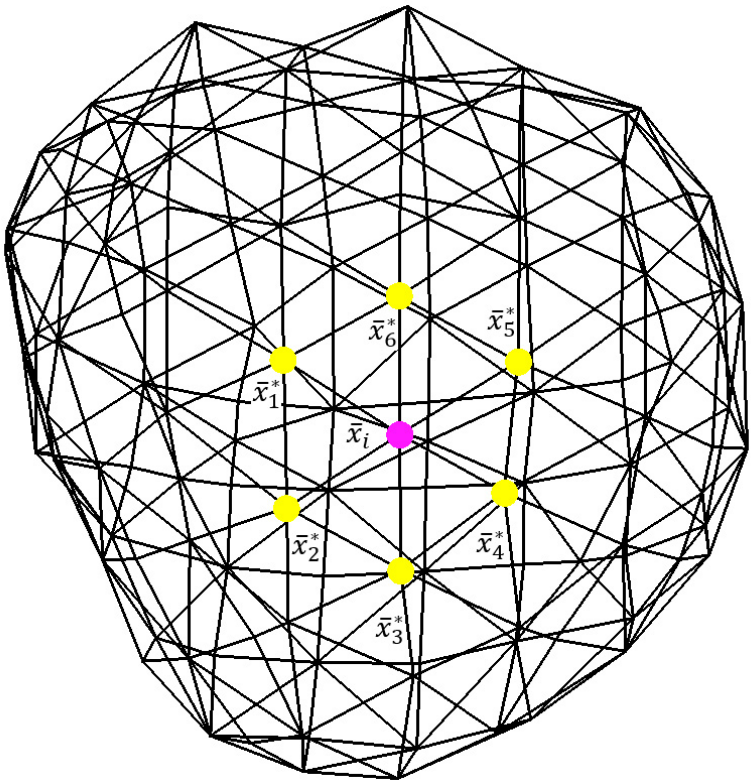

Figure 3.1: The reconstructed epicardial surface is depicted as a triangulated mesh interconnecting source nodes. Source node $\bar{x}_i$ (purple) is surrounded by its nearest neighbors (yellow) denoted $\bar{x}_j^*(j = 1, \ldots, 6)$

The posterior probability of the $\bar{x}$ over the weights is also Gaussian,

$$p(\bar{x}|\bar{y};\beta,\Gamma) = \frac{1}{\int \exp(-L(\bar{x}))d\bar{x}} \exp(-L(\bar{x})), \tag{3.19}$$

where $L(\bar{x}) = \frac{\beta}{2}|\bar{y} - A\bar{x}|^2 + \frac{1}{2}\bar{x}'\Gamma\bar{x}$. To minimize the $L(\bar{x})$, the most probable value of $\bar{x}$ can be estimated as

$$\bar{x}_{MP} = (A'A + \frac{1}{\beta}\Gamma^{-1})^{-1}A'\bar{y}. \tag{3.20}$$

The covariance $\Sigma_{\bar{x}}$ evaluated at $\bar{x}_{MP}$ is then

$$\Sigma_{\bar{x}} = (\nabla^2 L(\bar{x},\Gamma,\beta))^{-1} = (\Gamma + \beta A'A)^{-1}, \tag{3.21}$$

where ∇ denotes the gradient in the space of $\bar{x}$. Using evidence approximation [91], the marginal likelihood written by integrating the hyperparameters between Eq. 3.14 and Eq. 3.16 can be written as

$$\begin{aligned} p(\bar{y};\beta,\Gamma) &= \int p(\bar{y}|\bar{x}_{MP};\beta)p(\bar{x}_{MP};\Gamma)d\bar{x} \\ &= (\frac{2\pi}{\beta})^{-\frac{M}{2}}(2\pi)^{-\frac{N}{2}}\prod_{i=1}^{N}(\alpha_i + \psi_i)^{1/2} \\ &\cdot \int \exp(-L(\bar{x}_{MP}))d\bar{x}. \end{aligned} \tag{3.22}$$

To estimate the hyperparameters β and Γ by maximizing the marginal likelihood Eq. 3.22, we employed the expectation–maximization (EM) algorithm to iteratively update the β, Γ by taking the natural log of Eq. 3.22, and differentiating this expression with respect to $\gamma_i (i = 1, \ldots, N)$ to find the optimum:

$$\frac{\partial}{\partial\gamma_i}\log p(\bar{y};\Gamma,\beta) = \frac{1}{2\gamma_i} - \frac{\bar{x}_i^2}{2} - \frac{1}{2}\mathrm{Tr}(\Sigma_{\bar{x}}). \tag{3.23}$$

Setting the derivative with respect to γ_i to zero gives the following identity for γ_i, which maximizes the evidence

$$\gamma_i^{\mathrm{new}} = \frac{1}{\bar{x}_i^2 + \Sigma_{ii}} \quad i = 1, \ldots, N, \tag{3.24}$$

where Σ_{ii} is the i-th diagonal element of the $\Sigma_{\bar{x}}$.

Many learning rules for β have been proposed [98]. However, in noisy environments some of the learning rules cannot provide an optimal β, thus leading to degraded performance. To localize a pacing/VT-exit site on the epicardial surface, we only attempt to identify a node on the epicardial surface. Therefore, we assigned a value to β, calculated by using the conventional Bayesian linear inverse problem method (see 3.2.5), and then we used it to find the diagonal values of Γ and the source estimates $\bar{x}_{MP}$. The proposed method ignores the irrelative nodes and pairs of nodes, keeping only the most relative ones. In practice, during the iterative estimation, each hyperparameter γ_i can be modified to obtain an optimal value using the evidence approximation. If there is not enough evidence in the data that the i-th parameter should be non-zero, the prior variance will have a large value of γ_i, which means that the i-th parameter in effect will be "switched off" [98]. Thus, most of γ_i are pruned out from the model when γ_i exceeds the given threshold value. This way, the inverse prior variance γ_n^{-1} for nodes that remain increases and a sparse solution is accelerated.

Hyperparameter β Estimation

In Eq. 3.2, the sum-of-squares error function $E_{\bar{y}} = \frac{1}{2}\|\bar{y} - A\bar{x}\|^2$ is chosen; the noise ϵ on the measured data is assumed to have Gaussian distribution with zero mean, with variance $\frac{1}{\beta}$; the likelihood model then takes the form of Eq. 3.14. So, the posterior distribution under zero-mean Gaussian prior based on the decay function $E_{\bar{x}} = \frac{1}{2}\|\bar{x}\|^2$ for the unknown turns out to be:

$$p(\bar{x}|\bar{y};\beta,\alpha) \propto \exp(-\frac{\beta\|\bar{y} - A\bar{x}\|^2}{2}) \exp(-\frac{\alpha\|\bar{x}\|^2}{2}), \tag{3.25}$$

where α is the inverse variance of the priori distribution. The most probable value of $\bar{x}$ can be calculated by finding the maximum of the posterior distribution. It is more convenient to maximize the posterior by minimizing the negative logarithm of the posterior distribution, because of a monotonic increasing property of logarithm. Since two hyperparameters (α, β) are independent of $\bar{x}$, we can minimize $-\log(p(\bar{x};\beta,\alpha))$ given by

$$-\log p(\bar{x}|\bar{y}) = \frac{\beta}{2}|\bar{y} - A\bar{x}|^2 + \frac{\alpha}{2}|\bar{x}|^2. \tag{3.26}$$

Differentiation gives

$$-\frac{\partial}{\partial \bar{x}} \log p(\bar{x}|\bar{y}) = \frac{\partial}{\partial \bar{x}}(\frac{\beta}{2}|\bar{y} - A\bar{x}|^2) + \frac{\partial}{\partial \bar{x}}(\frac{\alpha}{2}|\bar{x}|^2)$$
$$= \beta(A^T\bar{y} - A^TA\bar{x}) - \alpha\bar{x} = 0, \tag{3.27}$$

resulting in the most probable value

$$\bar{x}_{MP} = (A^TA + \frac{\alpha}{\beta}I)^{-1}A^T\bar{y}. \tag{3.28}$$

To find two hyperparameters $\Theta(= \alpha, \beta)$, the marginal probability density function (pdf) can be written as

$$p(\bar{y};\Theta) = \int p(\bar{y}|\bar{x}_{MP};\beta)p(\bar{x}_{MP};\alpha)d\bar{x}$$
$$= (\frac{2\pi}{\beta})^{-\frac{M}{2}}(\frac{2\pi}{\alpha})^{-\frac{N}{2}}$$
$$\cdot \exp(-L(\bar{x}_{MP}))(2\pi)^{\frac{N}{2}} \det(H)^{-\frac{1}{2}}, \tag{3.29}$$

where $L(\bar{x}_{MP}) = \beta E_{\bar{y}}(\bar{x}_{MP}) + \alpha E_{\bar{x}}(\bar{x}_{MP})$, $H(= \beta A^{'}A + \alpha I)$ is the $N \times N$ Hessian matrix of the total error function. We employ the EM method to maximize $p(\bar{y};\Theta)$. This is equivalent to minimizing $-\log p(\bar{y};\Theta)$, yielding the effective cost function:

$$-\log p(\bar{y};\Theta) = L(\bar{x}_{MP}) + \frac{1}{2}\log\det(H) - \frac{N}{2}\log\alpha$$
$$-\frac{M}{2}\log\beta + \frac{N}{2}\log 2\pi. \tag{3.30}$$

Using differentiating, the α is given by,

$$\alpha^{\text{new}} = (\sum_{i=1}^{N}\frac{\lambda_i}{\lambda_i + \alpha})/2E_{\bar{x}}(\bar{x}_{MP}), \tag{3.31}$$

where $\lambda_i(i = 1, \ldots, N)$ are the eigenvalues of $\beta A^{'}A$. With the same procedure as for α, the log-evidence can be differentiated with respect to β

$$\beta^{\text{new}} = (M - \sum_{i=1}^{N}\frac{\lambda_i}{\lambda_i + \alpha})/2E_{\bar{y}}(\bar{x}_{MP}). \tag{3.32}$$

The iterative algorithm is given by

(1) Initialize α and β with positive random numbers between 0 and 1.

(2) Estimate x_{MP} using Eq. 3.28.

(3) Re-estimate diagonal elements of α and β using the criteria from Eqs. 3.31 and 3.32.

(4) If convergence criterion is fulfilled then stop; else go back to step 2.

To evaluate the convergence using the maximum change in α and β between iterations, the algorithm stops at iteration l when $W(l) < \varepsilon$ where

$$W(l) = \max |\alpha(l) - \alpha(l-1)|, |\beta(l) - \beta(l-1)|, \quad \varepsilon > 0. \tag{3.33}$$

Therefore, the l-th β is used in the Bayesian method.

3.3 Clinical and Simulation Protocols

3.3.1 Study population

Four patients who underwent epicardial mapping were enrolled. These patients had a history of ventricular tachycardia resistant to amiodarone or two other antiarrhythmic drugs, and patients with implantable defibrillators and recurrent appropriate device therapies. Detailed description of the four cases is included in Appendix C.1.2.

3.3.2 Patient-specific models

CT-imaging was acquired for each patient in the supine position. All patients underwent computed tomography (CT) scanning prior to the procedure for registration with electroanatomic mapping and generation of patient-specific geometry by a custom software, and surface electrodes were applied on the patient torso according to our Dalhousie Standard methodology [99, 100] (See Appendix A.1). The Dalhousie standard torso consists of 352 nodes in Fig. 3.2 (panel A, blue part), which was used to align with the patient-specific locations of the 120-lead electrodes in Fig. 3.2 (panel A, red part) for customizing the Dalhousie standard 352-node torso as shown in Fig. 3.2 (panels B, C, E and F).

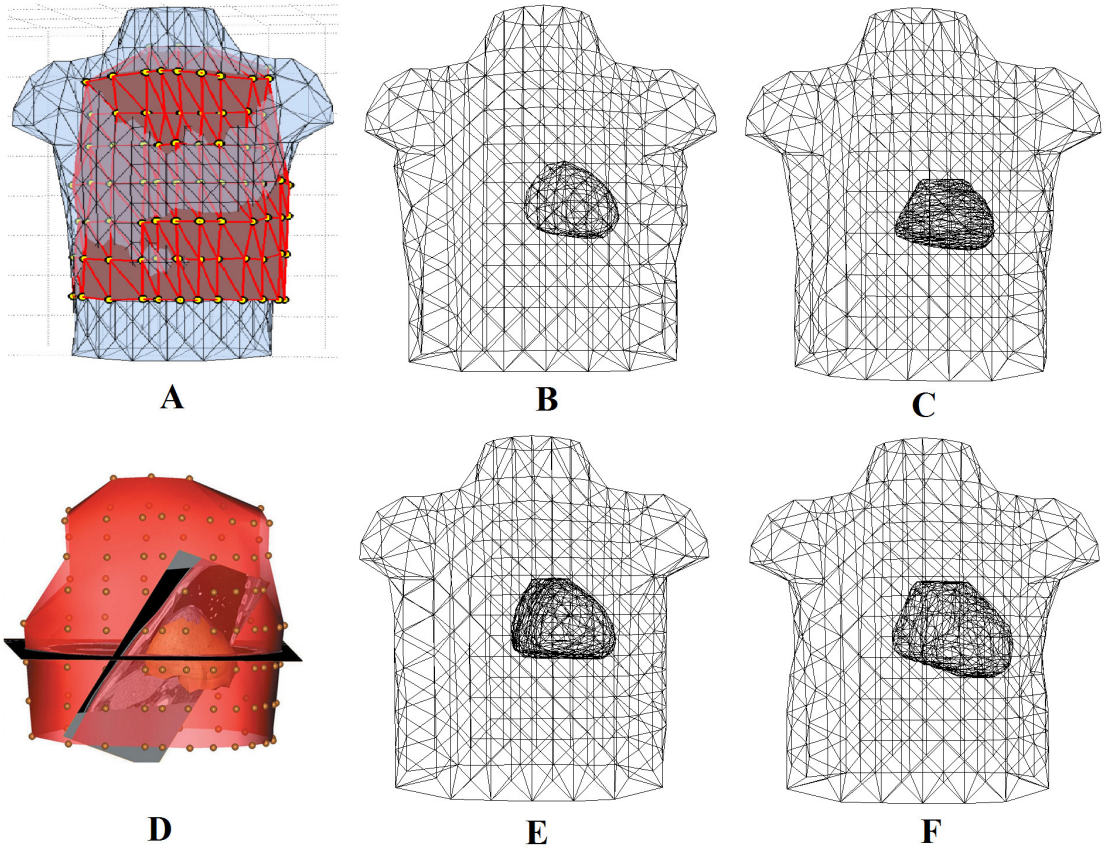

Figure 3.2: A: Anterior view of the standard Dalhousie torso (blue) aligned with the triangulated surface (red) of patient-specific locations of the 120 surface electrodes (yellow disks). B, C, E, F: Patient-specific geometry with epicardial surface for the subjects #1 to #4. D: Registration of electroanatomic map with CT.

3.3.3 Data acquisition and processing

The detailed data acquisition is described in the Appendix B.1. For the purposes of this study, we used the BSPM data corresponding to known pacing sites (with spatial coordinates provided by the electroanatomic system), and analyzed them off-line. Fig. 3.3 shows a butterfly plot of the BSPM data of a representative paced beat. The following features were extracted: (1) QRS integral ($\int$QRS), a time integral of the QRS complex in microvoltseconds (μVs); (2) trimmed QRS integral ($\int \mathrm{QRS}_{\mathrm{ms}}$) calculated over the initial 10, 20, 30, 40, 50, 60, 70, 80 ms of the QRS complex (denoted as $\int \mathrm{QRS}_{10}$, ... etc.) from the onset of QRS complex.

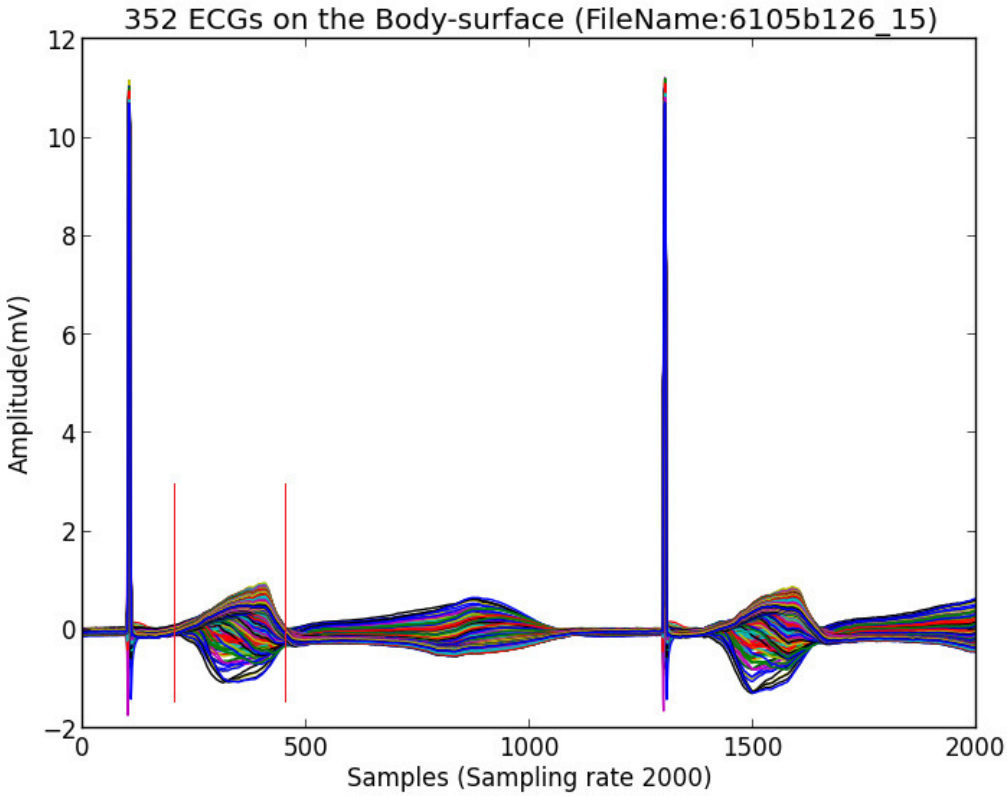

Figure 3.3: Butterfly plot of the body-surface potential mapping (BSPM) data with pacing spikes during epicardial pacing of Patient #2 who underwent epicardial catheter ablation. The red vertical lines indicate the onset and the offset of the QRS complex.

3.3.4 Analysis of experimental data

The gold standard for assessing accuracy of the inverse procedure was provided by the Carto© electroanatomic mapping system during the epicardial ablation procedure. The patient-specific Carto© geometry was registered manually (by J.L. Sapp) and fused with the patient's CT geometry by a custom software, to facilitate quantitative comparison. The locations of the Carto© sites where pacing was applied were projected onto the triangulated mesh of the CT epicardial surface (Fig. 3.4). As a measure of accuracy, the Euclidean distance was calculated for each recording between the inversely-calculated potential minimum and the actual pacing site exported from the Carto© electroanatomic system and projected on the discretized epicardial surface. The means and standard deviations of the localization error over all pacing sites were calculated (in millimeters).

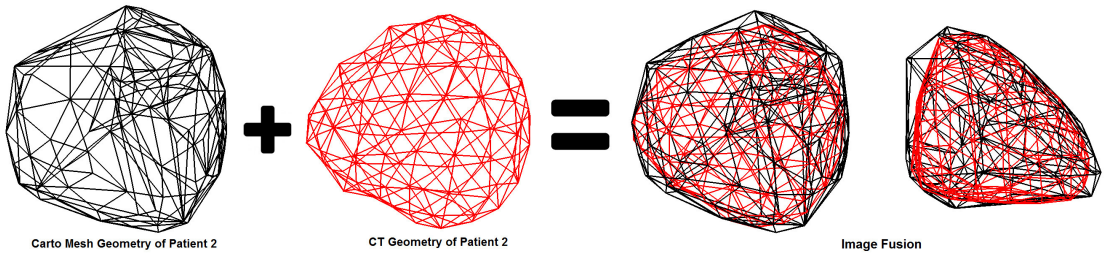

Figure 3.4: Patient-specific image fusion. The patient-specific Carto© electroanatomic geometry was incorporated into the coordinate system of the computed tomography (CT) geometry to register and fuse in the same coordinate system.

For analysis of pacing-site localization, we compared the Bayesian method with both Tikhonov methods in localizing 78 epicardial pacing sites pooled for all 4 patients. The ℓ_1-norm method is based on the normal derivative of the potential as a penalty function [55]; and the ℓ_2-norm regularization penalizes Laplacian function (a second-order Tikhonov [SOT] scheme); regularization parameters are chosen by the L-curve method [94]. For two of the four patients, epicardial potential distributions corresponding to VTs for which an exit site was identified by clinical mapping were also calculated by using both Bayesian and Tikhonov methods.

3.3.5 Simulation protocol

To further validate the Bayesian method and compare it with Tikhonov methods, model-based simulations were performed using patient-specific geometry. Sets of epicardial and body-surface potentials were calculated using a forward simulation using a single-dipole source [60] at anatomically significant locations.

For each patient's geometry separately, simulated epicardial (Φ_H^S) and body-surface (Φ_B^S) potentials with added Gaussian noise were calculated for 17 dipoles on the epicardium, one in each AHA segment [101]. The 17 locations were determined by picking a triangle in the appropriate area of the epicardial surface, moving the dipole source 5 mm along the inward normal, and making the dipole direction the same as the inward normal of the selected triangle. The relative error (RE) and correlation coefficient (CC) were calculated in each case, to compare forward-simulated and inversely-estimated potentials.

$$RE = \sqrt{\frac{\sum_{i=1}^{N}(\Phi_i^C - \Phi_i^S)^2}{\sum_{i=1}^{N}\Phi_i^S}}; \tag{3.34}$$

$$CC = \frac{\sum_{i=1}^{N}(\Phi_i^S - \Phi_{mean}^S)(\Phi_i^C - \Phi_{mean}^C)}{\sqrt{[\sum_{i=1}^{N}(\Phi_i^S - \Phi_{mean}^S)^2 \sum_{i=1}^{N}(\Phi_i^C - \Phi_{mean}^C)^2]}}, \tag{3.35}$$

where Φ_i^C is the inversely-estimated epicardial potential at the i-th node, Φ_i^S is the corresponding forward-simulated potential; Φ_{mean}^S and Φ_{mean}^C are their respective mean values. Fig. 3.5 shows patient-specific locations of 17 dipole sources with the direction of the inward normal, based on AHA bull's-eye display [101].

3.4 Results

3.4.1 Simulation study

We compared, in terms of RE and CC, the capabilities of the Bayesian method and Tikhonov methods to recover epicardial potentials previously generated by the forward calculation. Fig. 3.6 shows the corresponding CC and RE in boxplot format. It is evident that the Bayesian method can recover epicardial potentials with the highest CC_{mean} ($CC_{\text{mean}} = 0.87$ compared to 0.71 for ℓ_1-norm method and 0.69 for ℓ_2-norm [SOT] method); *i.e.*, it can recover the spatial pattern of epicardial potentials

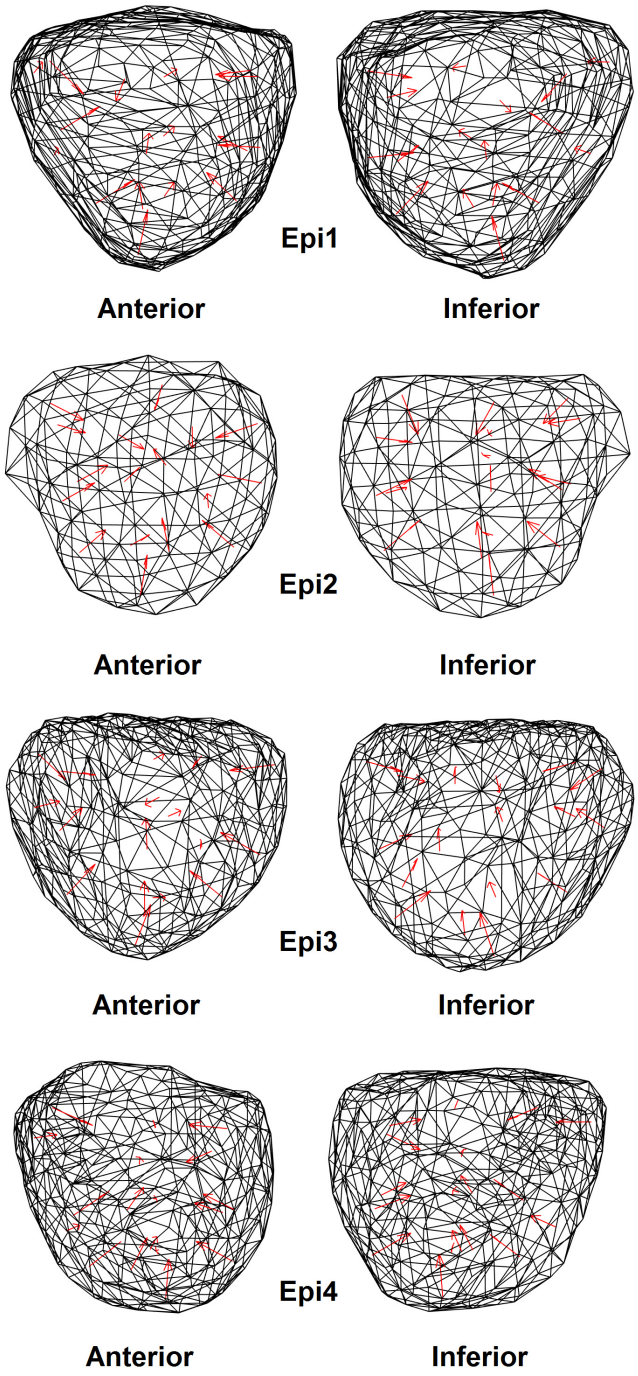

Figure 3.5: A single dipole with the direction of the outward normal at 17 locations on epicardial surface, for each patient separately.

more faithfully than the other methods. Also, the Bayesian method produces the smallest RE.

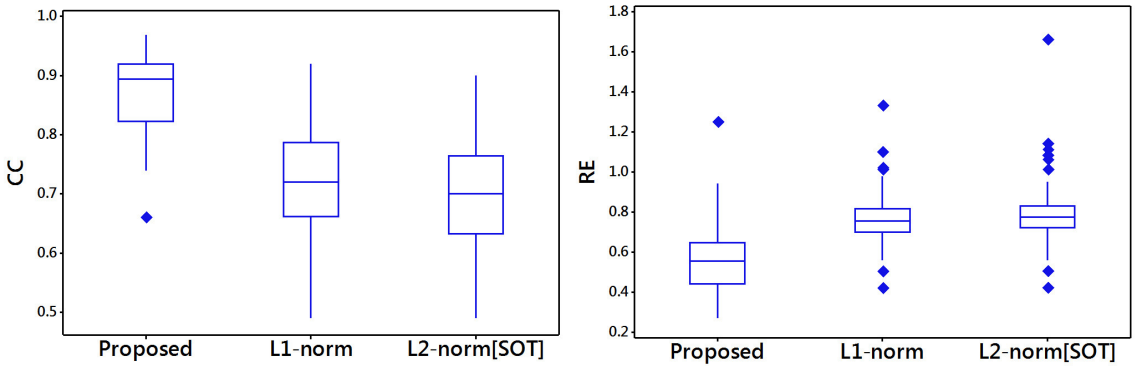

Figure 3.6: Results of simulation experiments. Boxplots illustrate the ability—in terms of correlation coefficient (CC) and relative error (RE)—to recover forward generated epicardial potentials by the proposed Bayesian method, and by the two Tikhonov methods. Boxes represent interquartile range, error-bars represent range, and line in the box indicates median.

3.4.2 Localization of epicardial pacing sites

The localization accuracy was tested for: pooled pacing sites ($n = 78$), pacing sites of each patient separately ($n = 23, 24, 21, 10$), and pooled pacing sites in the normal tissue ($n = 33$), scar tissue ($n = 31$), and scar-margin tissue ($n = 14$). The accuracy of pacing-site localization for varied intervals of $\int$QRS input variables is listed in Table 3.1, with localization errors of an optimal integration interval indicated for each patient. Fig. 3.7 compares localization performance of the Bayesian method with that of the Tikhonov methods across all integration windows of input variables. With increasing window size, the localization error does not change significantly for ℓ_1-norm and ℓ_2-norm methods; however, for the Bayesian method it tends to decrease, reaching the minimal value at 60-ms window. Thus we considered the "optimal" integration interval of trimmed $\int$QRS input variables to extend 60 ms from the QRS onset.

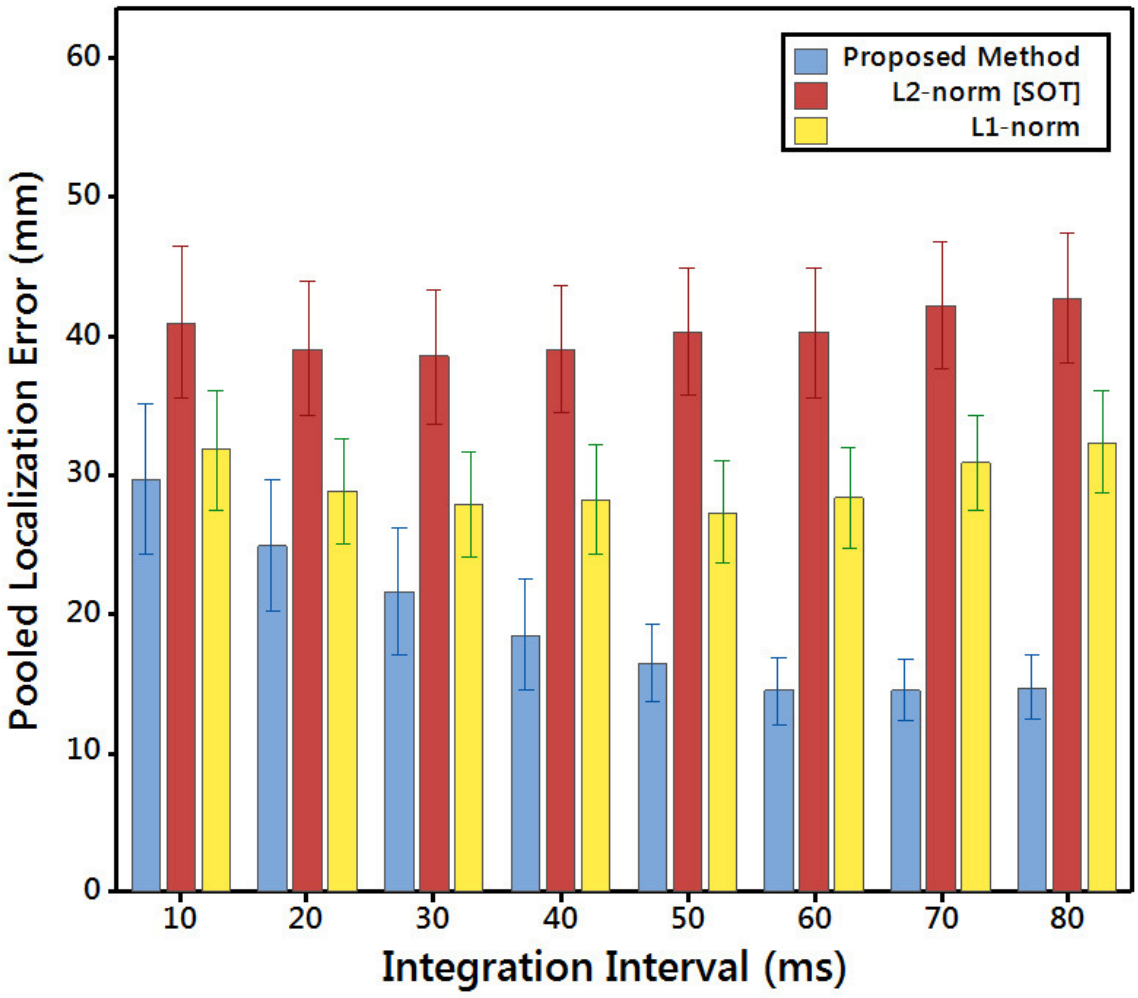

Figure 3.7: Results of clinical experiments. Mean localization errors with SD of the proposed Bayesian method and the two Tikhonov methods, across all integration-intervals of $\int QRS$ input variables, for all available pacing sites ($n = 78$).

Table 3.2 shows—for each patient separately—the accuracy of pacing-site localization for three methods, all using the $\int \mathrm{QRS}_{60}$ input variables. The pairwise t-test demonstrated statistically significant differences in the mean error for each pair of these three methods: Inverse solutions using the Bayesian method—for pooled ($n = 78$) epicardial pacing sites—were significantly more accurate than those estimated by the ℓ_2-norm method (P=0.0007), and the ℓ_1-norm method (P=0.0053). Also, the pooled localization accuracy of the ℓ_1-norm method was better than that achieved by the ℓ_2-norm method (P=0.022).

We found that for each subject, there were several outlier pacing sites that had a localization error larger than 20 mm. To investigate the source of these unacceptable errors, we sorted all pacing sites into three categories in terms of the electroanatomic substrate around them, as characterized by bipolar voltage measured by Carto© system. Fig. 3.8 shows the localization error of the Bayesian method for the pacing in no-scar areas ($n = 33$), scar-margin areas ($n = 14$), or scar areas ($n = 31$). The pacing sites within scar region show the largest median of localization error (16.8 mm), whereas the pacing within the area with no scar shows the lowest median of localization error (10.6 mm), with the mean and standard deviation (10.7 $\pm$ 7.4 mm). The Bayesian method's localization accuracy within no-scar region and for pacing sites with no-delay response ($n = 17$) was 7.6 $\pm$ 6.4 mm, which is significantly better than that (13 $\pm$ 9 mm, $P < 0.00001$) achieved previously by Sapp *et al.* [26] by means of the Tikhonov method and using the same clinical data.

3.4.3 Localization of VT-exit sites

Table C.2 contains clinical data of two patients suffering from scar-related VT (Patient #1 and Patient #2) for whom epicardial VT-exit sites were identified by epicardial contact mapping. Figure 3.9 illustrates how Bayesian and Tikhonov inverse solutions estimated these known exit sites in each patient. In patient #1, the site of successful ablation of VT1 was at the infero-basal LV as indicated on the electroanatomic map in Fig. 3.9 (panels a). This site was estimated by both Tikhonov methods with the localization error of 24.2 mm (panels f & j), whereas the epicardial potential distribution obtained by the Bayesian method featured a minimum at a distance of 13.3 mm from the ablation site (panel n). In patient #2, the VT-exit site for VT2 was also

Table 3.1: Accuracy of pacing-site localization achieved by the Bayesian method for varied integration intervals of $\int$QRS input variables in 4 patients

Subject #	No. of Pacing Sites	Localization Error of the Proposed Method Integration Intervals of $\int QRS$ (Mean ± SD)							
		10 ms	20 ms	30 ms	40 ms	50 ms	60 ms	70 ms	80 ms
1	23	19.6 ± 12.6	16.7 ± 10.4	13.2 ± 9.2	13.8 ± 9.1	13.0 ± 9.9	**12.9 ± 9.7**	14.5 ± 10.0	15.1 ± 11.2
2	24	35.2 ± 17.7	29.8 ± 16.9	27.9 ± 15.7	23.2± 12.5	21.3 ± 13.7	18.8 ±13.6	17.3 ± 10.8	**16.1 ± 10.9**
3	21	23.6 ± 18.5	18.4 ± 11.3	13.8 ± 7.9	12.5 ± 5.1	12.5 ± 5.1	**11.7 ± 5.7**	11.7 ± 5.7	11.8 ± 5.9
4	10	52.5 ± 44.3	45.5 ± 40.4	42.3 ± 41.2	31.1 ±39.8	21.6 ± 18.5	**14.1 ±13.2**	14.1 ± 13.2	17.2 ± 12.4

Accuracy of localization in terms of Euclidean distance (mm) from the predicted node to the known pacing-site node on the patient-specific epicardial surface as Mean ± standard deviation (SD). Smallest error for each patient is in **bold** face.

Table 3.2: Accuracy of pacing-site localization achieved by Bayesian and Tikhonov methods: patient-by-patient results

Subject	No. of Sites	ℓ_2-norm [SOT] Localization Error (mm)	ℓ_1-norm Localization Error (mm)	Proposed method Localization Error (mm)
1	23	33.8 ± 21.5	27.3 ± 17.6	12.9 ± 9.7
2	24	45.5 ± 18.5	33.0 ± 16.0	18.8 ± 13.6
3	21	40.4 ± 22.1	21.8 ± 14.0	11.7 ± 5.7
4	10	42.7 ± 18.1	34.0 ± 11.0	14.1 ± 13.2

All three methods used $\int \text{QRS}_{60}$ input variables. The localization error (in mm) was calculated for pacing sites of each patient as mean ± SD of estimated distance over the LV endocardial surface.

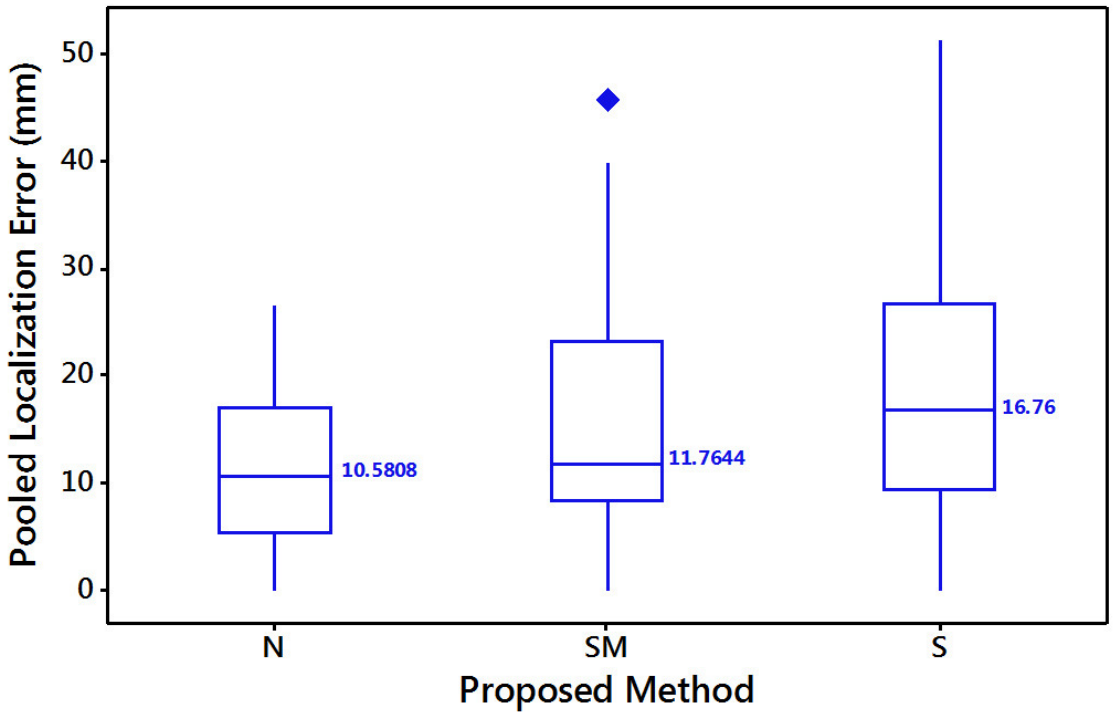

Figure 3.8: Errors of the Bayesian inverse solution in localizing epicardial pacing sites within no-scar areas (N), scar-margin areas (SM), and scar areas (S). Boxplots as in Fig. 3.6, with median values attached.

at the inferio-basal LV, at the scar margin, as indicated on the electroanatomic map in Fig. 3.9 (panels d). Fig. 3.9 (panels h) shows a corresponding epicardial potential distribution obtained by the ℓ_1-norm inverse solution, with the site of minimum potential at a distance of 28.4 mm from the successful ablation site of VT2, still at the infero-basal aspect of the LV (panel h). However, the minimum of potential distribution obtained by the ℓ_2-norm method for the VT2 predicts erroneously the VT-exit site at the basal-superior LV (panel m). Fig. 3.9 (panel p) shows the Bayesian inverse solution features the site of minimum potential in close proximity to the site of successful ablation of VT2, at a distance of 9.3 mm.

3.5 Discussion and Conclusions

The principal goal of this study was to improve localization of the earliest epicardial activation by reconstructing electrical potential distributions on the epicardial surface from the temporal-integral variables extracted from multiple body-surface ECGs. We achieved this goal by developing a data-driven method based on empirical Bayesian framework and the smoothing Automatic Relevance Determination (ARD) model for deriving dynamic spatio-temporal *a priori* constraints. To validate the proposed method, we used both *in silico* and *in vivo* experiments, using data acquired from four patients suffering from scar-related VT who underwent CT scan, EP study, and epicardial ablation procedure aided by the Carto© electroanatomic mapping system. Data exported from the latter system constitute the gold standard for the assessment of localization performance.

The proposed Bayesian method based on the ARD model provides—in comparison with the established methods using a Tikhonov-type regularization—an improved spatio-temporal estimation of the electrical potentials and their time-integrals across the epicardial surface of the heart. The innovative aspect of the proposed method is that the prior variance of each unknown parameter is estimated from the observed ECG data by introducing a hierarchical prior on the variance [91]. The smoothing ARD associates one group of hyperparameters to each source prior based on a weighting function using only a small group of relevant spatio-temporal features and automatically pruning the remaining features. The ARD model can force any unnecessary parameters to zero for irrelevant sources on the epicardial surface, which helps

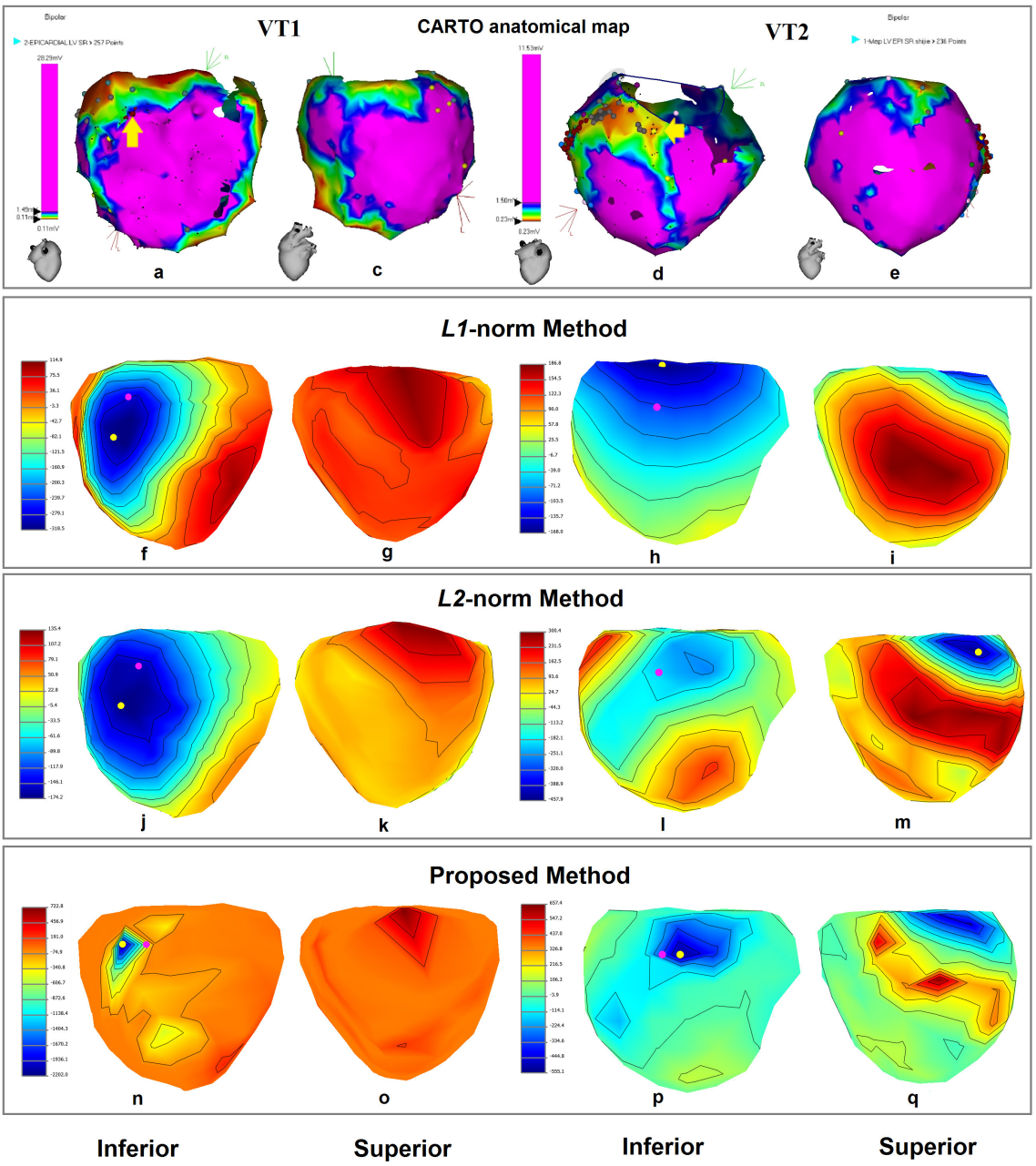

Figure 3.9: Localization of VT-exit sites by epicardial inverse-solution mapping. Top Row: Electroanatomic substrate as depicted by epicardial Carto© voltage maps for patients #1 (a & c) and #2 (d & e); Second Row: epicardial inverse-solution maps of the electrogram integrals during VT1 (f & g) and VT2 (h & i), obtained by the ℓ_1-norm method; Third Row: maps corresponding to those in the 2nd row, obtained by the ℓ_2-norm method; Bottom Row: maps corresponding to those in the 2nd row, obtained by the Bayesian method. The yellow arrows on the Carto© maps mark the clinically-identified VT exit; these exit sites were registered to the inverse-solution potential maps and marked by purple dot. The estimated sites of myocardial activation origin are marked as yellow dots in the corresponding inverse-solution maps.

to efficiently localize the origin of ventricular activation. This empirical Bayesian framework with a smoothing ARD model yields significantly higher performance of source localization than the widely-used Tikhonov-type regularization, demonstrating that the empirical priors are superior to conventional fixed priors. We found that the performance of the proposed method in localizing the origin of ventricular activation improves when the temporal-integration window for calculating input ECG variables encompasses a longer interval than just initial 30–40 ms from the onset of activation; the optimal temporal window appears to be 60–80 ms from the QRS onset, *i.e.*, it corresponds to the time required for the depolarization wave to spread near-completely throughout the ventricular mass.

The Bayesian method's ability to recover epicardial potential distributions (more accurately, time-integrals of epicardial electrograms) was compared with the corresponding ability of Tikhonov-type methods. We can confirm previous findings that the ℓ_1-norm method performs better than the ℓ_2-norm method in localizing focal sources [102, 103]. However, the ℓ_1-norm method [55] has a slow convergence and the solution becomes unstable when the constant parameter in the diagonal weight matrix is small. In addition, the accuracy of the constraint-based methods incorporating a fixed *a priori* information depends on determination of an optimal regularization parameter. Recently, various novel spatially-constrained regularization schemes were proposed. For instance, Potyagaylo *et al.* [104] used spatially-varying regularization parameters with different weightings for endocardial and epicardial components of the solution. Chamorro-Servent *et al.* [105] optimized the placement of the pseudo-boundaries (depending on the distance between the torso electrodes and the nearest heart locations) to achieve significant improvements in inverse solutions in patients with structural heart disease.

The limitations of the present study is that the proposed inverse solution recovers only epicardial (not endocardial) potentials. However, the unique aspect of this and the previous [26] study is that the reference data were obtained from electroanatomical maps created with a catheter in direct contact with the epicardial surface. We used the same clinical data as the previous study by Sapp *et al.* [26], which relied on an inverse solution regularized by the Tikhonov method. From the same pacing sites

as used previously we found a highly-significant improvement in the resulting localization accuracy. In conclusion, the results of both *in vivo* and *in silico* experiments yielded by the present study should provide a strong incentive for pursuing further investigation and clinical application of data-driven Bayesian methods in electrocardiographic imaging.

Chapter 4

Inverse Solution for Activation Times

4.1 Introduction

The clinical electrophysiological (EP) studies are now routinely used to investigate abnormal propagation pathways [106] by techniques of activation mapping [107]. Isochronal activation map visualizes propagation of the activation front wave in the myocardium and it provides a summary of an entire activation sequence. The passing activation wave front can be detected from a steep negative deflection of a local electrogram; this was first proposed by Sir Thomas Lewis in 1914 [108, 109]. Invasive experiments designed to map the local activation times (LAT) throughout the whole ventricle were later performed by Durrer and co-workers, who placed closely-spaced differential electrodes in the ventricular wall of perfused human hearts [14]; they showed that the passing activation wave front can be most conveniently detected as a spike-like deflection on bipolar electrograms.

The standard method by which activation times are calculated from inversely-calculated unipolar electrograms (EGMs) is to detect the steepest negative deflection; this approach has been widely used and it is well supported by experimental and theoretical evidence [110]. Producing the LAT as an isochronal map over the entire epicardial/endocardial surface by direct measurement requires maneuvering of the catheter tip to collect EGMs point by point and determining for each point a LAT. In the clinical EP studies, it is more common to detect passing activation wave front beneath the catheter tip as spikes on bipolar electrograms [110]. The bipolar-catheter technique was adopted in the present clinical study to define reference activation times based on Carto© measurements. This technique is sometimes used in clinical EP studies to map sustained arrhythmias; however, the approach cannot be used when the arrhythmia is not sustained or when it is not reproducibly inducible or hemodynamically tolerated.

Over the past decade, electrocardiographic imaging (ECGI) as a noninvasive

imaging modality has demonstrated its ability to reconstruct unipolar EGMs and isochronal maps on the epicardial surface from body-surface potentials [27]. The isochronal maps generated by the computed unipolar EGMs can serve as a summary of the entire sequence of ventricular activation. There are two most frequently used methods for calculating the activation times from the ECGI. In a standard computation, the LAT is defined as the time when the activation wave front passes beneath the electrode, which is usually set either at the maximum negative slope of the electrical deflection for computed unipolar EGM for that location, or at the maximum signal magnitude for bipolar recordings [111]. Alternatively, a nonlinear temporal model based on an *a priori* restriction of transmembrane potential waveforms can be adopted on the heart surface model [61, 74, 112, 113]; this latter technique is referred to as activation-time imaging. However, this approach with its *a priori* restrictions does not accurately describe the full temporal behavior of the heart-surface potentials, and it can be especially problematic in the cases of acute ischemia or prior myocardial infarction. Moreover, the activation-time imaging requires strict physiological constraints based on the assumption of uniform double layer (UDL) model [114].

This Chapter presents a new methodology for constructing isochronal activation maps, based on measurements of propagation delay between pairs of computed EGMs at neighboring locations. This new method of detecting activation times was assessed by correlation with known activation maps derived from *directly measured* epicardial EGMs collected invasively through Carto© electroanatomic system (Biosense Webster, Diamond Bar, CA, USA).

4.2 Methods

4.2.1 Study population

Validation of the proposed methodology of activation mapping was performed by using clinical data of Patient #4, who had an implantable cardioverter defibrillator (ICD) device (see Appendix C, Table C.2). During the epicardial catheter procedure, the reference LAT was measured at multiple sites when keeping the ICD device pacing.

4.2.2 Computed electrograms

The empirical Bayesian method proposed in Chapter 3 was used to reconstruct EGMs that represent the variation of voltage as a function of time at a given point on the epicardial surface. We extract the body-surface potential on the torso at each time instant and use it as input for the inverse solution to recover a time-sequence of potentials (EGMs) on the epicardial surface.

4.2.3 Global activation mapping

To assess the accuracy of the inverse procedure in preserving timing information, the activation time at multiple points on the epicardial surface was mapped, generating an activation map of the pathways followed by the electrical depolarization wave front during the activity of the heart.

Dubois *et al.* [115] presented a method that measures the delay in the activation of two neighboring locations during a single propagation of the depolarization wave front. Based on this method, we employed a cross-correlation method to determine the time delay in the activation of two neighboring locations. After calculating the cross-correlation for each pair of neighboring locations, the maximum (or minimum if the signals are negatively correlated) of the cross-correlation function indicates the instant of time at which the signals are best aligned, *i.e.*, the time delay between the two signals is determined by the argument of the maximum, as in $\tau_{\text{delay}} = \arg\max_t((f \star g)(t))$, where the $\star$ is the convolution operation for two continuous functions f and g based on time series, such as a couple of EGMs in our application.

Using the known activation relationships of two neighboring locations with these delays as the inputs, a linear system can be constructed. For a patient-specific geometry, let us assume N computed EGMs for which the activation map is known on the epicardial surface. The activation times of two EGMs (i and j) are such that the difference is equal to the time necessary for the wave front to travel from one to the other:

$$T_j - T_i = \tau_{ij} \quad i, j = 1, \ldots, N; j > i. \tag{4.1}$$

Therefore, the resulting system contains as many equations as there are pairs of neighboring EGMs on the epicardial surface. Eq. 4.1 is rewritten in a matrix form $DT = \tau$, where $T = [T_1, \ldots, T_N]'$ is the vector of activation times on the epicardial surface, each row of D corresponds to an equation for a given two neighboring locations, and the vector τ includes all neighboring pairs of EGMs'delays (τ_{ij}). For example, let's imagine 3 time-instants of activations: T_1, T_2, T_3, leading to 3 equations given by

$$\begin{bmatrix} -1 & 1 & 0 \\ 0 & -1 & 1 \\ -1 & 0 & 1 \end{bmatrix} \begin{bmatrix} T_1 \\ T_2 \\ T_3 \end{bmatrix} = \begin{bmatrix} \tau_{12} \\ \tau_{23} \\ \tau_{13} \end{bmatrix}. \tag{4.2}$$

Since the matrix D assumes a sparse dictionary, we used Sparse Bayesian Learning [116] to solve this linear system.

4.3 Results

4.3.1 Global activation time (GAT)

Fig. 4.1 (panels (e)-(h)) shows the measured local activation time (isochronal maps) obtained from Carto© electroanatomic mapping system by using contact mapping [117]. The inversely-calculated isochronal map (panel (f)) shows earliest activation on the right-ventricular apex (red) and the activation wave spreading over the right-ventricular anterior and free wall in approximately 120 ms. The latest area to activate was the basal region of the anterior left ventricle at around 220 ms as shown in panels (e) and (h). To demonstrate the inverse isochronal map, an epicardial pacing site located on the right-ventricular apex was selected and indicated by the blue dot and arrow, as shown in Fig. 4.1. The computed isochronal maps (in Fig. 4.1 panels (i)-(l)) obtained by the GAT mapping show a qualitatively similar spread of activation, and feature several characteristics: the early activation, which captures the right-ventricular (RV) apical region and then propagates from the right-ventricular anterior wall to the left-ventricular anterior wall, as well as the latest activation of the anterior-basal wall, are all correctly estimated by the proposed activation-map method. Moreover, a scar region with lowest bipolar potentials (panel (b)) located on the right-ventricular apex is near the ICD pacing site, causing delayed propagation (indicated by the green part) as shown in lateral RV view of panel (j). The inverse isochronal maps of panels (i) and

(j) illustrate the very slow propagation on the right-ventricular free wall and anterior basal areas that are indicated as having large scar margin and tissue with unknown status (panels (a) and (b)).

Fig. 4.1 (panels (m)-(p)) illustrates the activation maps constructed by a standard computation. Although the calculated activation isochrones were approximately able to capture early and late activation areas, the whole isochronal map features inaccurate propagation patterns. The standard method estimates the local activation time (LAT) at each location by using maximum negative slope method ($\min\frac{\partial V}{\partial t}$) during depolarization. In this case, the poor resolution of the estimated activation time by the classical method was caused by several factors: multiple negative deflections, fractionated electrograms or poor signal-to-noise ratio (SNR), particularly in unipolar recordings.

4.4 Discussion and Conclusions

This Chapter presents a novel method for assessing the local activation time at the sites of computed EGMs. Inverse-solution isochrones yielded by this algorithm correlated closely with known activation maps obtained by electroanatomic contact mapping during endocardial pacing at the right-ventricular apex, delivered by ICD.

The discrepancies in comparison of the proposed method and the reference LAT isochronal map occur in part due to limitations of the inverse-solution method used here, which can only produce *unipolar* EGMs, which inherently contain superposition of both near and distant field potentials; moveover, the reference activation times were obtained from directly measured *bipolar* EGMs, which reflect only intrinsic near-field activity [119]. Bipolar EGMs exhibit a sharp peak when the activation wave front passes by the catheter tip, whereas the fastest down-slope in inverse unipolar EGMs has reduced ability to resolve changes in activation times over neighboring epicardial regions.

In diseased hearts, there are many situations in which the peak negative derivative may not be a reliable predictor of activation time. Spach *et al* [120] have recorded multi-component unipolar EGMs from isolated atrial preparations for which the maximum negative derivative alone did not accurately predict activation of the myocardial

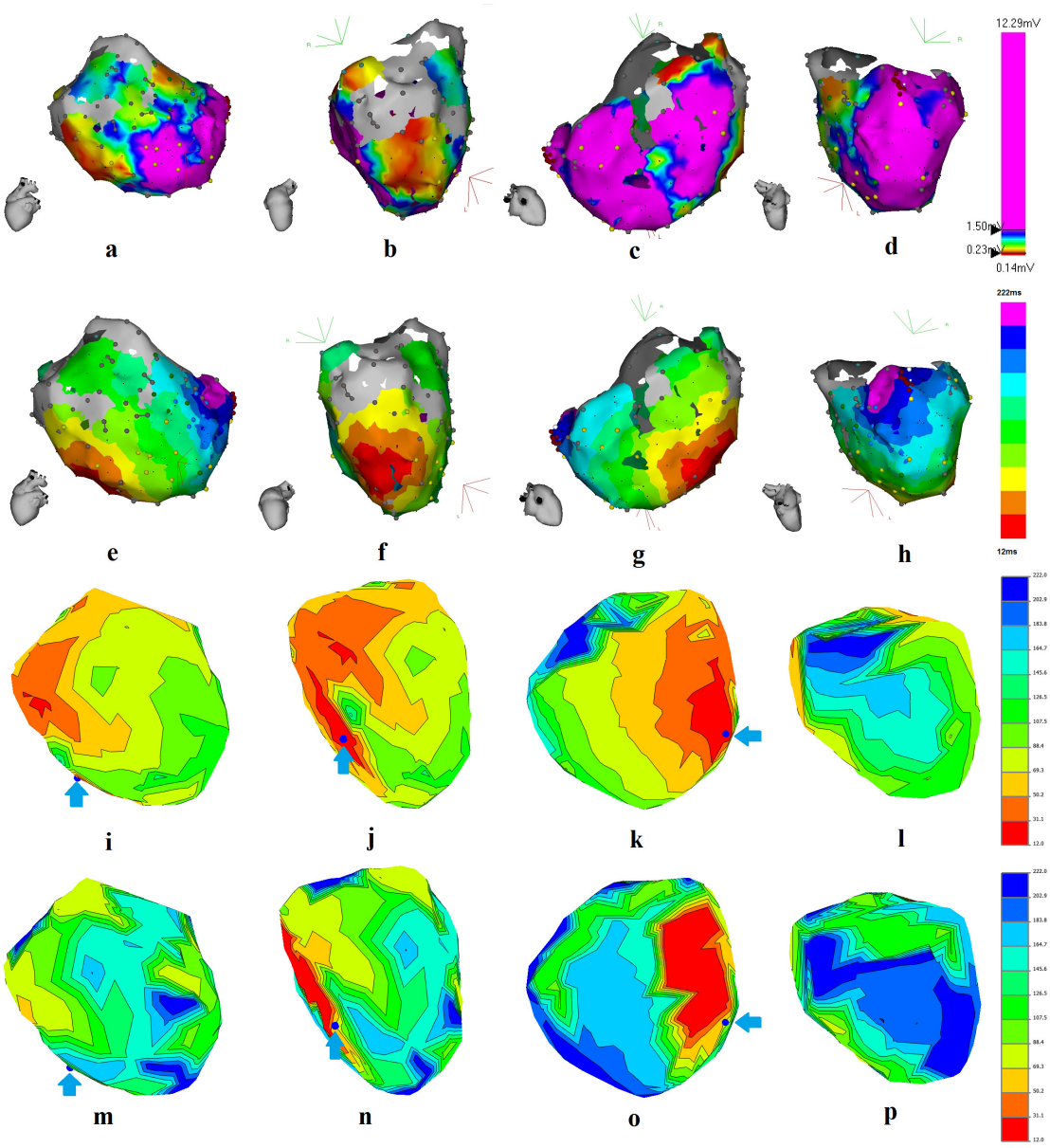

Figure 4.1: Maps for Patient #4. The first row (panels a-d) shows Carto© epicardial substrate maps based on bipolar potentials; the second row (panels e-h) depicts the activation times as determined by Carto© system; the third row (panels i-l) shows the activation times estimated by the proposed methodology of activation mapping; the last row (panels m-p) shows the activation times estimated by the classical method (maximum negative slope). The blue dot and arrow indicate where the ICD pacing site projects on the epicardial surface. These estimated maps were constructed using the Map3D [118] software.

cells immediately beneath the extracellular electrode. They found the maximum negative derivative sometimes reflected activation of larger bundles of fibers that were some distance from the recording site. Thus, the presence of diseased tissue further complicated interpretation of EGMs obtained by the inverse solution. The method of steepest down-slope applied to EGMs obtained by the inverse solution relies on derivatives calculated from a few successive samples, which makes it vulnerable to measurement noise in body-surface potentials or to slight changes in the regularization parameter that controls the amount of smoothing in the inverse calculation. In cases of EGMs with low peak amplitude, and thus low steepest-slope values, there were multiple points with very similar steepest slope values, which caused spurious assignment of activation times. This problem was partially mitigated by spatial smoothing of inverse EGMs using moving-average spline interpolation. Similar observation of quick activation over large regions and lines of abrupt jumps in the calculated activation-time maps were noticed in figures published by other investigators [27, 121, 122].

In calculating the activation maps, we have noticed that the inversely calculated isochrone maps did not reflect the presence of the scar, and thus they must be correlated with known myocardial scar for interpretation. This would be possible with advanced imaging software, such as MUSIC platform, which integrates dalayed-enhancement MRI and multidetector CT to derive a patient-specific 3D geometry to provide complementary information on VT substrate that facilitates VT ablation [123, 124].

Chapter 5

Localization of Endocardial Pacing Sites

5.1 Introduction

Electrocardiographic imaging (ECGI) is a non-invasive technology that can provide valuable information for pre-procedure planning of the catheter ablation interventions. The ECGI methodology involves solving the inverse problem, which is usually defined as computation of epicardial potentials from body-surface potential mapping (BSPM) data acquired from multiple thoracic sites [27]. However, to reconstruct the epicardial potential distributions is often *not* the clinical endpoint. Clinical electrophysiologists are in many cases more interested in electrical activity on the endocardial surface. Although endocardial potentials can be reconstructed by the commercial electroanatomic mapping systems, such as Carto© system (Biosense Webster, Diamond Bar, CA, USA) [125] or Ensite™ system (St Jude, St Paul, MN, USA) [126]), the procedure is invasive and time consuming. Therefore, one of the challenging tasks for ECGI to address is to develop a reconstruction of endocardial potentials from BSPM data; this would greatly facilitate ablation procedures for ventricular arrhythmias.

Several studies considered recently the reconstruction of distributed sources on the endocardial surface [32, 74, 85, 127, 128, 129, 130, 131, 132, 133]. The distributed-source models can be either the surface-potential model [59, 60] or the equivalent-double-layer (EDL) model [61, 62, 112], both introduced in Chapter 2. The surface-potential model was applied in Section 2.3.1 to computing linear transfer coefficients relating potentials on the epicardial surface and those on the body surface. The limitation of this approach is that endocardial sources must be estimated by projecting epicardial potential distributions on the endocardial surface. To overcome this limitation, attempts have been made to reconstruct simultaneously both epicardial and endocardial potentials [32, 85, 130, 132, 133]. In addition, the EDL model showed promise in activation-time imaging, which estimates the local strength of the double-layer source for each node of the heart surface. The EDL approach opens

the possibility of distinguishing between endocardial and epicardial activation [74]. However, all studies using the EDL model are based on simplifying (and possibly oversimplifying) assumptions with regard to cardiac electrophysiology, and these assumptions are often not valid under pathological conditions of ischemia or infarction. For example, van Dam [74] introduced a fastest-route algorithm (FRA) into the EDL model by assuming the heart to be a connected graph and assigning each edge in this graph a conduction velocity, which was set to be twice as high along the ventricular wall than in the transmural direction. Potyagaylo and co-workers [134] evaluated the FRA sensitivity with respect to the possible modeling errors under the assumption of structurally normal ventricular tissue, and they found that the performance of FRA is strongly dependent on assumed conduction velocities.

We turned our attention to the Bayesian learning algorithms [77] and we hypothesized that they can be advantageously applied to solving the inverse problem of cardiac electrophysiology. Chapter 3 reviewed historical context of Bayesian approaches applied to the reconstruction of epicardial-surface potentials from BSPM data, and introduced a data-driven Bayesian method that achieves significantly better inverse-solution performance than the Tikhonov-type regularization methods. To simplify computing tasks, one can take advantage of the sparse representation of cardiac sources by the EDL model—introduced by Salu [135]—using unit-strength double layer on depolarized sections of the ventricular surface and zero-strength on the remaining parts. With such sparse system, one can employ the sparse Bayesian learning (SBL) approach—first proposed by Tipping [98]—and use it for localizing the origin of ventricular activation. Since the depolarization sequence in real ventricles is continuous and it takes at least 30 ms for the activation wave front to propagate through the ventricular wall [14, 135], we use temporal integrals of the QRS complex as a robust variable to represent the initial phase of ventricular activation.

The aim of this Chapter is to validate a data-driven Bayesian approach to localizing the origin of ventricular activation by using clinical data recorded in patients with structurally normal ventricular myocardium who underwent LV endocardial pacing. The Chapter has three distinct parts: Firstly, the forward solution based on the EDL model (introduced in Chapter 2) is used to produce a well-conditioned transfer matrix (see Section 2.3.2). Secondly, the sparse Bayesian learning method is applied,

assuming that apart from the initial site of activation, the remaining regions of the ventricular myocardium are silent; relying on this sparseness constraint, the method searches for a solution that has as few nonzero entries as possible. Thirdly, to validate the proposed method, *in silico* experiments are performed to assess localization accuracy for dipole sources in patient-specific torso geometry. Finally, the performance of the proposed method is compared with a data-driven nonlinear dynamic parametrization method of Erem and co-workers [85].

5.2 Methods

5.2.1 Problem formulation

The EDL theory—introduced by Cuppen *et al.* [61, 62, 112]—is based on the assumption that the extracardiac potential generated by the volumetric electric source distribution within the ventricular myocardium is equal to the potential generated by a dipole layer on the ventricular surface. The strength of the layer is proportional to the transmembrane potential (TMP) on this surface. A Heaviside step function represents the transmembrane action potential, leading to a relationship between body-surface potentials and the isochrones of activation at the ventricular surface. The basic equation is given by

$$\phi(\boldsymbol{p}, t) = \int_S A(\boldsymbol{p}, \boldsymbol{q}) H(t - \tau(\boldsymbol{q})) ds_{\boldsymbol{q}}, \tag{5.1}$$

where $\phi(\boldsymbol{p}, t)$ is the body-surface potential generated at point $\boldsymbol{p}$ at time t, and $A(\boldsymbol{p}, \boldsymbol{q})$ (see Chapter 2) is the transfer matrix representing the potential at points $\boldsymbol{p}$ on the body surface generated by an elementary current double layer source around points $\boldsymbol{q}$ of the ventricular surface and pointing towards the ventricular mass. The function $\tau(\boldsymbol{q})$ is the activation time, when the wave front is passing by the ventricular-surface points $\boldsymbol{q}$. $H(t-\tau(\boldsymbol{q}))$ is the Heaviside step function approximating the actual ventricular action potential; so the elementary sources $\boldsymbol{q}$, once switched "on" at time $\tau(\boldsymbol{q})$ remain "on" until the total ventricular surface has been activated. In the discrete form Eq. 5.1 can be written as

$$\phi_{i,t} = \sum_{j=1}^{N} A_{i,j} S_{j,t}, \tag{5.2}$$

where the strength $S_{j,t}$ of dipole $j(1,\ldots,N)$ on the closed ventricular surface is either 1 or 0 depending on whether the point $\boldsymbol{q}_j$ is already activated or not yet activated; body-surface potential ϕ_i at any point $\boldsymbol{p}_i(i=1,\ldots,M)$ on a body surface is a linear combination of N dipoles as basis vectors $S_1,\ldots,S_N$ at time t.

5.2.2 Forward calculation

In the present study, the transfer matrix A was first calculated for the patient-specific ventricular surface S_H and patient-specific body surface S_B, using the EDL source model (see Section 2.3.2 of Chapter 2), and then a sub-matrix A_{LV} $(M \times N_1)$ was extracted that depends only on the geometry of body surface S_B with M nodes and LV endocardial surface S_{H_1} with N_1 nodes.

5.2.3 Inverse problem: Sparse Bayesian Learning (SBL)

The mathematical expression of the inverse problem to be solved by the sparse Bayesian learning (SBL) method is given by

$$\bar{\Phi} = A_{\mathrm{LV}}\bar{S}_{\mathrm{LV}} + v, \tag{5.3}$$

where $\bar{\Phi} \in \mathbb{R}^{M\times 1}$ is a known vector of body-surface-measurements (we use a time-integral of the time-varying ECG potential $\int QRS$), $A_{\mathrm{LV}} \in \mathbb{R}^{M\times N_1}$ is the previously computed transfer matrix, $\bar{S}_{\mathrm{LV}} \in \mathbb{R}^{N_1\times 1}$ is reconstructed with N_1-dimensional sparse vectors on the LV endocardial surface, and $v \in \mathbb{R}^{M\times 1}$ is a vector of measurement noise. The SBL, applied to solving the sparse inverse problem, is based on the Automatic Relevance Determination (ARD) model [136] that is weighing the local spatial interactions on the endocardial surface. A Bayesian *empirical prior* was used to describe an *a priori* distribution developed by learning from the properties of the cardiac action potential, in terms of a set of unknown hyperparameters that must be estimated from the data.

Firstly, the SBL applies the ARD involved to assign a N_1-dimensional Gaussian hierarchical prior

$$p(\bar{S}_{\mathrm{LV}};\gamma) = \prod_{i=1}^{N_1}(2\pi\gamma_i)^{-\frac{1}{2}}\exp(-\frac{\bar{S}^2_{\mathrm{LV}_i}}{2\gamma_i}), \tag{5.4}$$

where $\gamma = [\gamma_1, \ldots, \gamma_{N_1}]'$ is an unknown vector that consists of N_1 hyperparameters to control the prior variance of each weight. Therefore, the priors can be given by

$$p(\bar{S}_{\mathrm{LV}_i}; \gamma_i, \forall i) \sim \mathcal{N}_{\bar{S}_{\mathrm{LV}}}(0, \Gamma), \tag{5.5}$$

where Γ is

$$\Gamma = \begin{bmatrix} \gamma_1 & \cdots & 0 \\ \vdots & \ddots & \vdots \\ 0 & \cdots & \gamma_{N_1} \end{bmatrix}.$$

The likelihood model $p(\bar{\Phi} \mid \bar{S}_{\mathrm{LV}})$ is assumed to be Gaussian with a noise variance σ^2 written as

$$p(\bar{\Phi} \mid \bar{S}_{\mathrm{LV}}; \sigma^2) = (2\pi\sigma^2)^{-\frac{M}{2}} \exp(-\frac{1}{2\sigma^2}\|\bar{\Phi} - A_{\mathrm{LV}}\bar{S}_{LV}\|^2). \tag{5.6}$$

Combining likelihood with prior, the posterior probability distribution of the $\bar{S}_{\mathrm{LV}}$ is also Gaussian,

$$p(\bar{S}_{\mathrm{LV}} \mid \bar{\Phi}; \sigma^2, \Gamma) = \mathcal{N}(\mu, \Sigma_{\bar{S}_{\mathrm{LV}}}), \tag{5.7}$$

with the mean $\mu = \sigma^{-2}\Sigma_{\bar{S}_{\mathrm{LV}}} A'_{\mathrm{LV}}\bar{\Phi}$ and the covariance $\Sigma_{\bar{S}_{\mathrm{LV}}} = (\sigma^{-2}A'_{\mathrm{LV}}A_{\mathrm{LV}} + \Gamma^{-1})^{-1}$. Given these hyperparameters, the value of $\bar{S}_{\mathrm{LV}}$ can be estimated as the Maximum-A-Posteriori (MAP) probability

$$\bar{S}_{\mathrm{LV}_{MP}} = (A'_{\mathrm{LV}}A_{\mathrm{LV}} + \sigma^2\Gamma^{-1})^{-1}A'_{\mathrm{LV}}\bar{\Phi}. \tag{5.8}$$

To accommodate practical applications, where $M << N$, the $\bar{S}_{\mathrm{LV}_{MP}}$ can be written as

$$\bar{S}_{\mathrm{LV}_{MP}} = \Gamma A'_{\mathrm{LV}}(\sigma^2 I + A_{\mathrm{LV}}\Gamma A'_{\mathrm{LV}})^{-1}\bar{\Phi}, \tag{5.9}$$

by using the identity $(C + DD')^{-1}D' = C^{-1}D(I + D'C^{-1}D)^{-1}$ [137]. The marginal likelihood can be obtained by integrating the hyperparameters in Eqs. 5.4 and 5.6

$$\begin{aligned} p(\bar{\Phi}; \sigma^2, \Gamma) &\equiv \int p(\bar{\Phi} \mid \bar{S}_{\mathrm{LV}_{MP}}; \sigma^2) p(\bar{S}_{\mathrm{LV}_{MP}}; \Gamma) d\bar{S}_{\mathrm{LV}} \\ &= \log|\Sigma_{\bar{\Phi}}| + \bar{\Phi}'\Sigma_{\bar{\Phi}}^{-1}\bar{\Phi}, \end{aligned} \tag{5.10}$$

where $\Sigma_{\bar{\Phi}} \triangleq \sigma^2 I + A_{\mathrm{LV}} \Gamma A_{\mathrm{LV}}^{'}$. To estimate hyperparameters Γ and σ^2 by maximizing the marginal likelihood, we used expectation-maximization (EM) algorithm to iteratively update the Γ and σ^2 by taking the log of Eq. 5.10 and differentiating this expression with respect to $\gamma_i (i = 1, \ldots, N_1)$:

$$\frac{\partial}{\partial \gamma_i} \log p(\bar{\Phi}; \Gamma, \sigma^2) = \frac{\gamma_i}{2} - \frac{\bar{S}_{\mathrm{LV}_i}^2}{2} - \frac{1}{2} \mathrm{Tr}(\Sigma_{\bar{S}_{\mathrm{LV}}}). \tag{5.11}$$

Setting the derivative with respect to γ_i to zero gives the following identity for γ_i, which maximizes the evidence

$$\gamma_i^{\mathrm{new}} = \bar{S}_{\mathrm{LV}_i}^2 + \Sigma_{ii} \quad i = 1, \ldots, N_1, \tag{5.12}$$

where Σ_{ii} is the i-th diagonal element of the $\Sigma_{\bar{S}_{\mathrm{LV}}}$. Similarly, we derive the σ^2 given by

$$(\sigma^2)^{\mathrm{new}} \leftarrow \frac{\|\bar{\Phi} - A_{\mathrm{LV}} \bar{S}_{\mathrm{LV}}\|_{\mathcal{F}}^2}{M} + \frac{\sigma^2}{M} \mathrm{Tr}[A_{\mathrm{LV}} \Gamma A_{\mathrm{LV}}^{'} ((\sigma^2)^{\mathrm{old}} I + A_{\mathrm{LV}} \Gamma A_{\mathrm{LV}}^{'})^{-1}]. \tag{5.13}$$

This learning rule for σ^2 assures robustness in noisy environment by setting the off-diagonal elements of $A_{\mathrm{LV}} \Gamma A_{\mathrm{LV}}^{'}$ to zero [138]. Based on the properties of the EM algorithm, this method is convergent, because the cost function is reduced, reaching a fixed point by each iteration. During this EM progress, σ^2 is sensitive to its initial value. Therefore, the noise variance σ^2 was set to a tenth of the source variance $(\mathrm{SNR}\frac{M}{\mathrm{Tr}(C^{1/2} C^{-1/2})})$ to establish a initial value in scale with the SNR of data, where the measurement noise covariance C was approximately estimated from collected body-surface data by calculating the square of standard deviation for each node.

The inverse problem in terms of the EDL source model for the depolarization phase entails finding the values of the Heaviside step function at discretization nodes of the endocardial surface and normalizing the solution between 0 and 1, as given by the equation

$$\bar{S}_{\mathrm{LV}_{i,0/1}} = \frac{\bar{S}_{\mathrm{LV}_i} - \bar{S}_{\mathrm{LV}_{\mathrm{Min}}}}{\bar{S}_{\mathrm{LV}_{\mathrm{Max}}} - \bar{S}_{\mathrm{LV}_{\mathrm{Min}}}}, \tag{5.14}$$

where $\bar{S}_{\mathrm{LV}_i}, i = [1, \ldots, N_1]$ is the inverse solution at each point, $\bar{S}_{\mathrm{LV}_{\mathrm{Min}}}$ is for the minima among all the data points, $\bar{S}_{\mathrm{LV}_{\mathrm{Max}}}$ refers the maxima among all the data

points, and $\bar{S}_{\mathrm{LV}_{i,0/1}}$ denotes the solution value at point i, normalized between 0 and 1.

5.3 Clinical Protocols

5.3.1 Study population

Three subjects with normal ventricular myocardium underwent 120-lead BSPM during the endocardial catheter procedure (this dataset is at: http://edgar.sci.utah.edu/). The pacing sites were identified on 3D electroanatomic maps acquired by the Carto© XP system (Biosense Webster, Diamond Bar, CA, USA). The study protocol was approved by the Ethics Review Committee of the Charles University Hospital, Prague, Czech Republic.

5.3.2 Patient-specific models

CT-imaging restricted to a limited number of slices was performed for each patient in supine position. The Dalhousie standard torso (see in Appendix A.1) consisting of 352 nodes was aligned with each patient's electrode locations for customizing the torso surface [99, 100].

5.3.3 Data acquisition and processing

The Dalhousie standard BSPM protocol was used to acquire BSPM data (Appendix B.1). For the purposes of this study, we used the BSPM data corresponding to known pacing sites (with spatial coordinates provided by the electroanatomic system), and analyzed them off-line at Dalhousie University. Eq. 5.2 can be transferred into a time-integral linear system given by:

$$\bar{\Phi} = A\bar{S} \quad \text{with} \quad \bar{\Phi} = \sum_{t=1}^{T} \phi_{:t}, \tag{5.15}$$

where $\phi_{:t} \equiv [\phi_{1:t}, \phi_{2:t}, \ldots, \phi_{n:t}]'$ is the $M \times 1$ vector of potential measurements at nodes of body surface at time t; $\bar{\Phi}$ is a time integral of the QRS complex of duration T; A is a transfer matrix, and $\bar{S}$ denotes the $N \times 1$ vector of double-layer strength on depolarized sections of the ventricular surface. The following features were extracted from ECG data: (1) QRS integral ($\int$QRS), a time integral of the QRS complex in

microvoltseconds (μVs); (2) trimmed QRS integrals ($\int \mathrm{QRS}_{\mathrm{ms}}$) calculated over the initial 10, 20, and 30 ms of the QRS complex (denoted as $\int \mathrm{QRS}_{10}$, ... etc.).

5.3.4 Simulation protocol

A model-based simulation study was performed using patient-specific geometry for validating the proposed method. Sets of LV endocardial and body-surface potentials were calculated using a forward simulation based on a single-dipole source at anatomically significant locations. In particular, for each patient's geometry separately, simulated endocardial and body-surface potentials with 0 dB Gaussian white noise were calculated for 16 dipoles on the endocardium, one in each AHA segment [51, 101]. These 16 locations were determined by picking a triangle in the appropriate area of the endocardial surface, moving the dipole source 5 mm along the inward-oriented normal, and making the dipole direction the same as the inward normal of this triangle. The mean and standard deviation of the localization error over all single-dipole sites ($n = 48$) was given (in millimeters) by comparing the inversely-calculated location and the known source-dipole site. Fig. 5.1 shows, for each patient separately, locations of 16 dipole sources with the direction of the inward normal based on AHA bull's-eye display [101].

5.3.5 Data analysis of inverse-solution methods

The patient-specific Carto© geometry was registered manually and fused with the patient's CT geometry (by Dr. Petr Štovíček), to facilitate quantitative comparison. More details for patient-specific geometry were presented by Erem *et al.* [85]. The gold standard for assessing accuracy of the inverse procedure was the information provided by the Carto© electroanatomic mapping system during the EP procedure. The locations of the Carto© sites where pacing was delivered were projected onto the discretized CT endocardial surface. As a measure of accuracy, the Euclidean distance was calculated for each recording between the computed unit strength and the actual pacing site projected on the endocardial surface. The means and standard deviations of the localization errors over all pacing sites were given (in millimeters) by comparing the inversely-calculated location and the known reference location identified from the Carto© electroanatomic system. For analysis of pacing-site localization, we compared

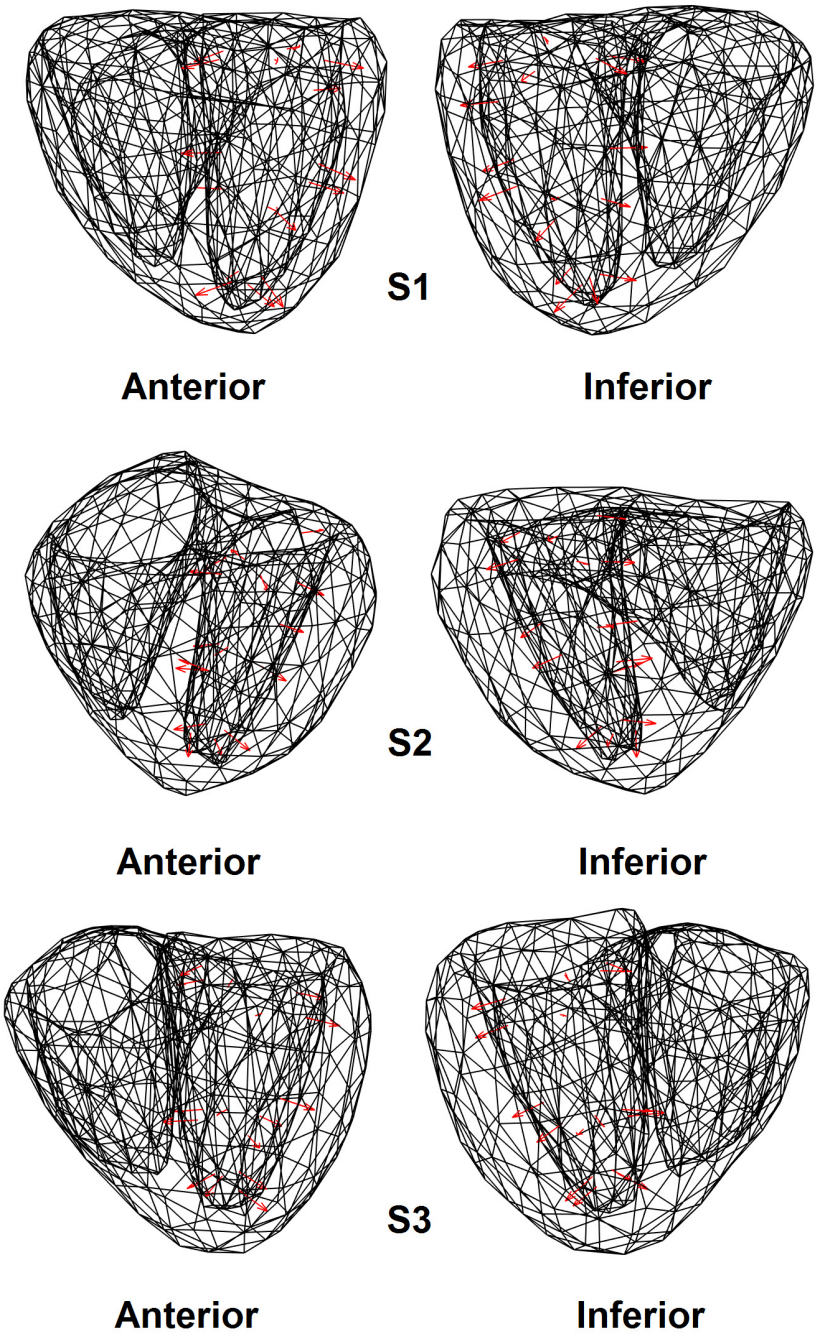

Figure 5.1: A single dipole with the direction of the inward normal at 16 locations on LV endocardial surface, for each subject (S #1, S #2, S #3) separately.

the performance of the proposed method with method of Erem and co-workers [85] in localizing the site of origin of ventricular activation based on 52 endocardial pacing sites pooled for all 3 subjects.

5.4 Results

5.4.1 Simulation study

We first estimated the accuracy of the proposed method in localizing endocardial dipoles from body-surface potentials generated by the forward calculation. Fig. 5.2 shows the frequency distribution of localization error for pooled single-dipole sites ($n = 48$) achieved by the proposed method. It is evident that the proposed method can accurately localize endocardial dipoles from simulated body-surface potentials with the mean and standard deviation of 9.4 ± 4.5 mm.

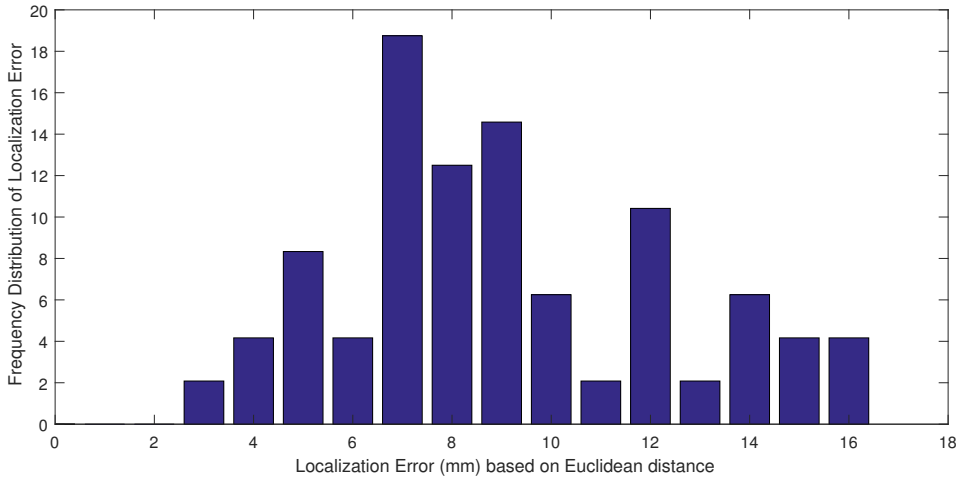

Figure 5.2: Frequency distribution of localization errors achieved by the proposed method in simulation experiment for pooled single-dipole sources ($n = 48$). Error is measured as Euclidean distance between the prediction node and the centroid of pacing-site triangle on the endocardial surface. Mean value $\pm$ standard deviation is 9.4 ± 4.5 mm.

Table 5.1: Accuracy of pacing-site localization achieved by the proposed method for varied intervals of integration $\int$ QRS

Patient #	No. of Pacing Sites	Localization Error based on the Proposed Method Intervals of Integration		
		10 ms	20 ms	30 ms
1	17	24.2 ± 14.0	20.5 ± 12.1	**19.7 ± 12.9**
2	21	20.2 ± 11.7	18.1 ± 9.1	**17.0 ± 9.1**
3	14	14.1 ± 7.6	14.1 ± 7.6	**12.6 ± 6.7**

Accuracy of localization in terms of Euclidean distance (mean ± SD) from the predicted node to the actual pacing-site node on the patient-specific endocardial surface. Optimal values are in **bold** face.

Table 5.2: Accuracy of pacing-site localization: Subject #1

Pacing Site (LV)	No. of Averaged Beats	Erem *et al.* Method Localization Error (mm)	Proposed Method Localization Error (mm)
1	28	29 ± 3	13.0
2	33	3 ± 5	13.8
3	29	39 ± 6	26.9
4	33	38 ± 8	29.0
5	34	54 ± 6	48.5
6	34	31 ± 9	15.3
7	34	29 ± 6	16.9
8	21	29 ± 6	16.9
9	20	19 ± 9	8.9
10	28	53 ± 6	14.2
11	33	46 ± 8	14.4
12	31	39 ± 6	4.6
13	24	24 ± 1	5.0
14	25	29 ± 10	11.8
15	21	26 ± 12	19.5
16	17	49 ± 4	27.4
17	22	44 ± 18	48.7

Erem *et al.* [85] averaged QRS complexes of a train of paced beats and, therefore, their localization error is given as mean ± SD; our proposed method is using $\int \mathrm{QRS}_{30}$ of a selected beat as an input variable. The underlined pacing sites were located in the septal region.

Table 5.3: Accuracy of pacing-site localization: Subject #2

Pacing Site (LV)	No. of Averaged Beats	Erem *et al.* Method Localization Error (mm)	Proposed Method Localization Error (mm)
1	43	40 ± 1	7.4
2	18	30 ± 2	21.1
3	38	41 ± 7	6.8
4	41	26 ± 1	2.5
5	35	34 ± 4	22.7
6	35	51 ± 20	16.2
7	27	22 ± 3	17.8
8	14	24 ± 0	27.1
9	29	38 ± 11	6.0
10	32	13 ± 14	21.9
11	33	17 ± 7	12.9
12	37	37 ± 10	27.8
13	30	30 ± 10	26.4
14	21	47 ± 11	19.4
15	28	42 ± 13	35.5
16	35	46 ± 7	25.3
17	33	23 ± 11	3.2
18	32	24 ± 10	6.2
19	35	49 ± 20	19.1
20	24	38 ± 15	14.3
21	34	21 ± 4	17.7

See legend of Table 5.2 for explanation.

Table 5.4: Accuracy of pacing-site localization: Subject #3

Pacing Site (LV)	No. of Averaged Beats	Erem *et al.* Method Localization Error (mm)	Proposed Method Localization Error (mm)
1	32	32 ± 4	12.3
2	34	35 ± 0	11.5
3	15	18 ± 10	7.4
4	31	32 ± 5	3.4
5	33	34 ± 5	10.0
6	34	54 ± 18	19.3
7	23	24 ± 9	9.9
8	34	32 ± 1	7.2
9	37	22 ± 4	31.0
10	37	39 ± 4	14.4
11	11	21 ± 24	8.0
12	34	33 ± 9	14.0
13	15	22 ± 12	16.6
14	22	30 ± 11	12.0

See legend of Table 5.2 for explanation.

Table 5.5: Accuracy of pacing-site localization achieved by two different methods

Subject No.	No. of Sites	Erem *et al.* Method Localization Error	Proposed Method Localization Error
1	17	34.2 ± 13.1	19.7 ± 12.9
2	21	33.0 ± 11.1	17.0 ± 9.1
3	14	30.6 ± 9.2	12.6 ± 6.7

The localization error (mm) for all pacing sites of each subject was calculated, as mean ± SD, by the proposed method and results were compared with those reported by Erem *et al.* [85]. The proposed method used the optimal 30-ms-integral ($\int \mathrm{QRS}_{30}$) input variables.

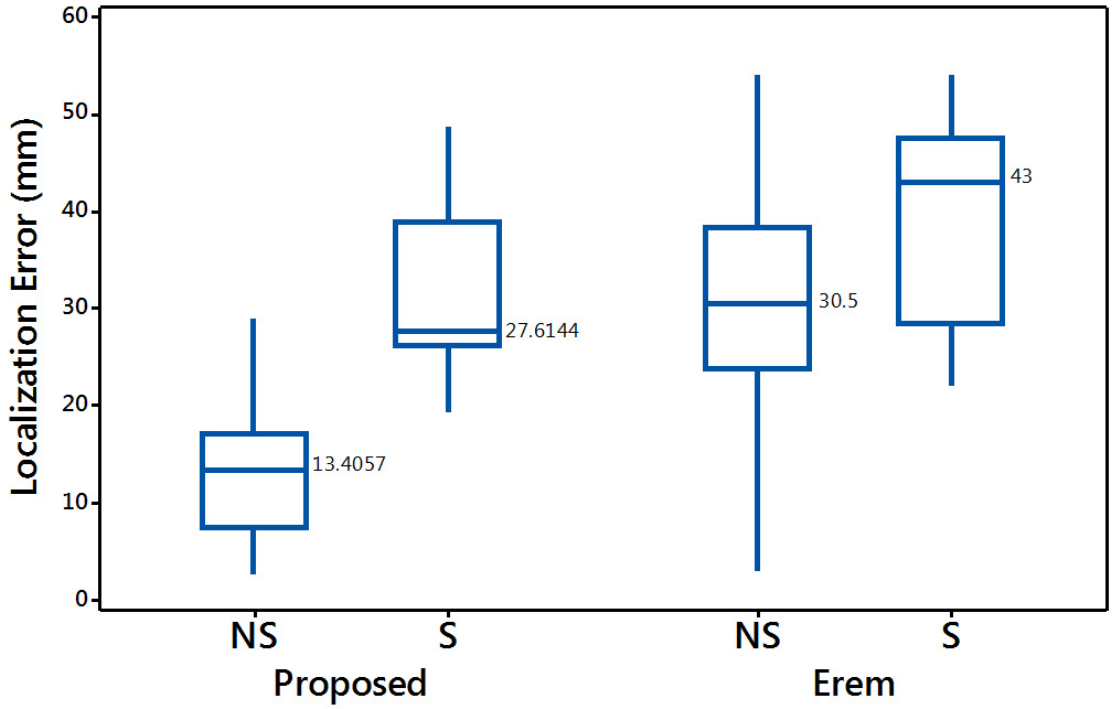

Figure 5.3: Box plot of Euclidean distances between sites of pacing as identified by Carto© electroanatomic maps and sites identified by the proposed method and the method previously introduced by Erem *et al.* [85]. Pacing sites are grouped into those that were within septal region (group S; $n = 10$), and those outside septal region (group NS; $n = 42$). Following the common convention, each box represents interquartile range and whiskers represent range; line with value represents median.

5.4.2 Localization of LV endocardial pacing sites

The localization accuracy was tested for: all available LV endocardial pacing sites ($n = 52$), and all pacing sites of each patient separately ($n = 17, 21, 14$). The inverse solutions presented in Table 5.1 were calculated by using time-integral variables with three different intervals of trimmed $\int$ QRS. The optimal interval of trimmed $\int$ QRS extends 30 ms from the QRS onset; the mean values and standard deviations of the localization error of the proposed solution for all pacing sites of subjects #1, #2, and #3 were 19.7 ± 12.9 mm, 17.0 ± 9.1 mm, and 12.6 ± 6.7 mm, respectively. Tables 5.2–5.4 summarize the localization accuracy for pacing sites of the three subjects

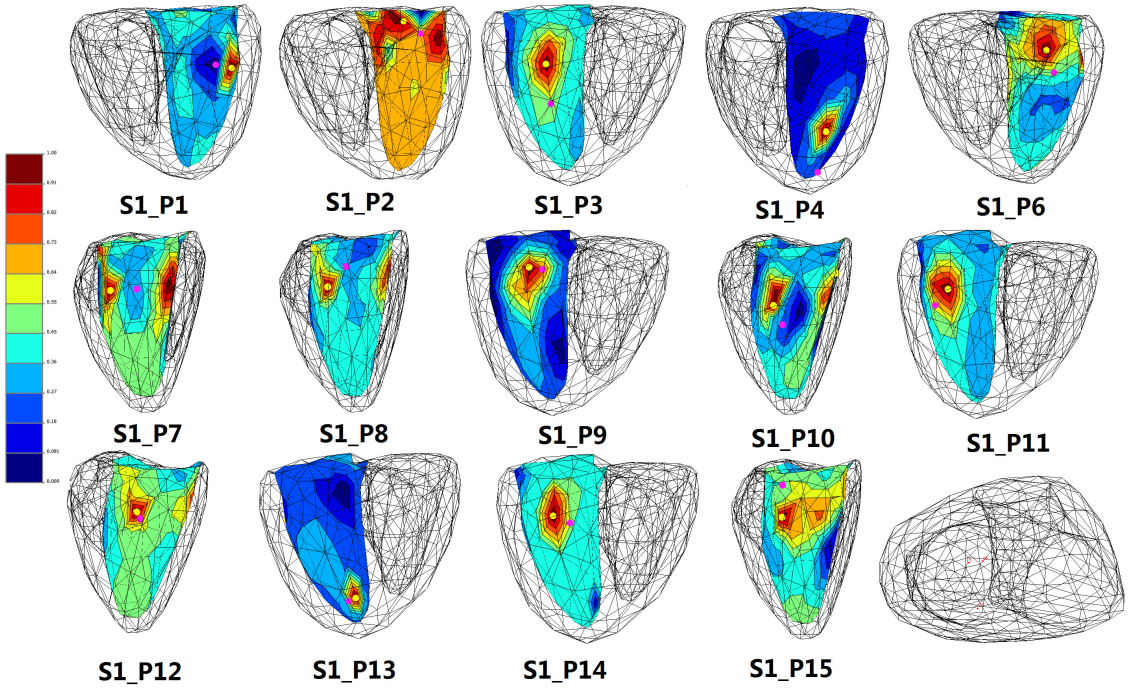

Figure 5.4: Subject #1: Normalized inverse-solution maps generated by the proposed method for estimating sites of LV endocardial pacing. There were 17 pacing sites (P1–P17) for this subject, 3 of them (P5, P16, P17) in the septal region; for each of the non-septal sites, there is a panel showing an inverse-solution map with the actual (purple dot) and the estimated (yellow dot) pacing site. The last panel shows 3 septal pacing sites (red dot and number) for which the localization error was large.

by a comparison of the proposed method based on the trimmed $\int QRS_{30}$ calculation with results of Erem and co-workers [85]. Table 5.5 shows—for each patient separately—the accuracy of pacing-site localization in comparison with results of Erem and co-workers [85], and the proposed method based on the trimmed $\int QRS_{30}$ calculation. It appears that the proposed method has a potential to improve the localization accuracy. To demonstrate that improvements in localization accuracy are statistically significant, we used the pairwise t-test to evaluate the mean error of the differentials between the proposed method based on the trimmed $\int QRS_{30}$ calculation with results of Erem *et al.* [85]. The proposed method for pooled pacing sites yielded more accurate results than the method of Erem and co-workers, with a statistically significant difference in accuracy ($P = 0.0039$).

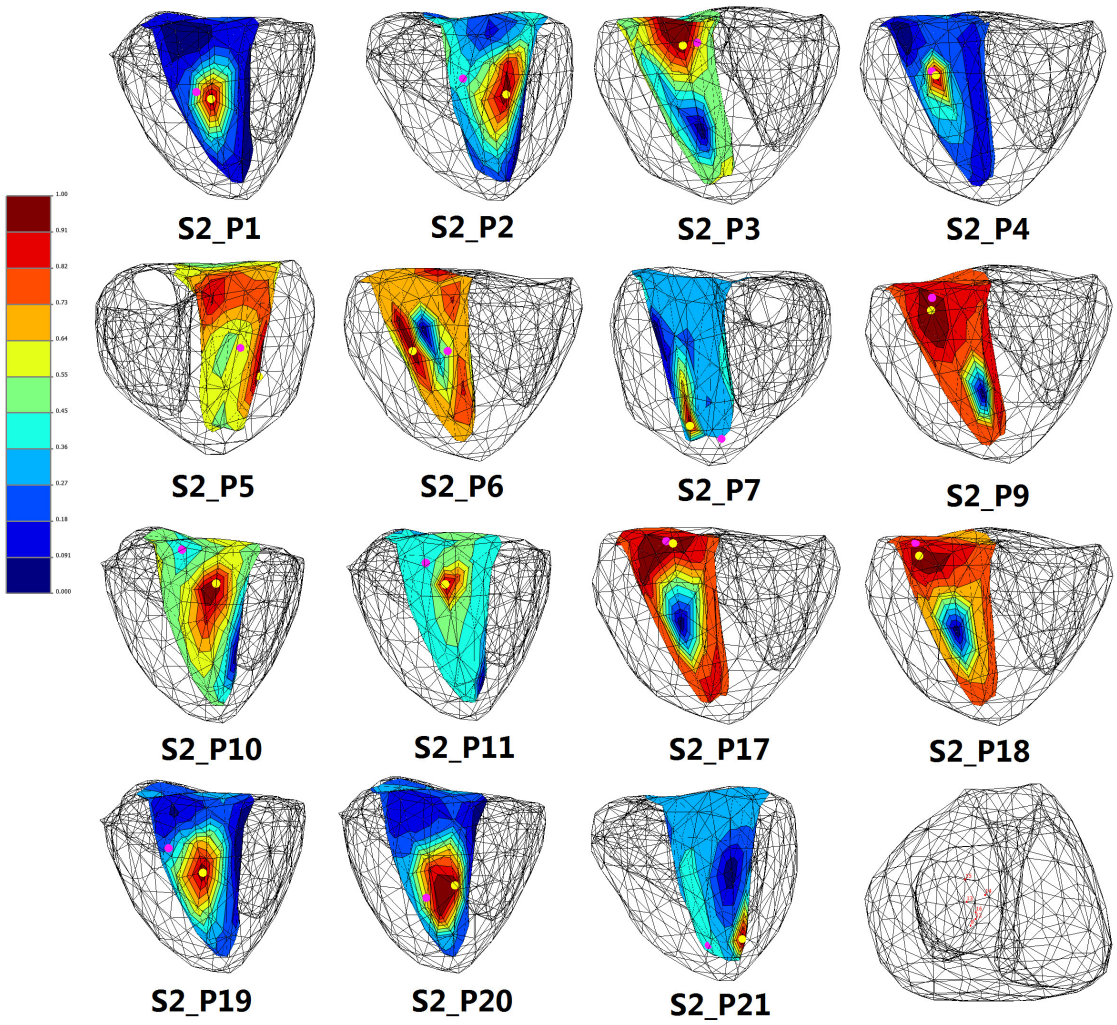

Figure 5.5: Subject #2: Normalized inverse-solution maps generated by the proposed method for LV endocardial pacing. The same format as in Fig. 5.4; there were 21 pacing sites for this subject, with 6 in the septal region; for each non-septal site, there is a panel showing an inverse-solution map and the last panel shows locations of septal sites.

For all three patients of this study, computed sites of early activation agreed well with sites registered from electroanatomic maps in all anatomical regions, except on the septum. The results of pacing-site localization accuracy in relation to the anatomical location of pacing are summarized in Figure 5.3, which graphically depicts localization accuracy of the two different inverse-solution methods in two different

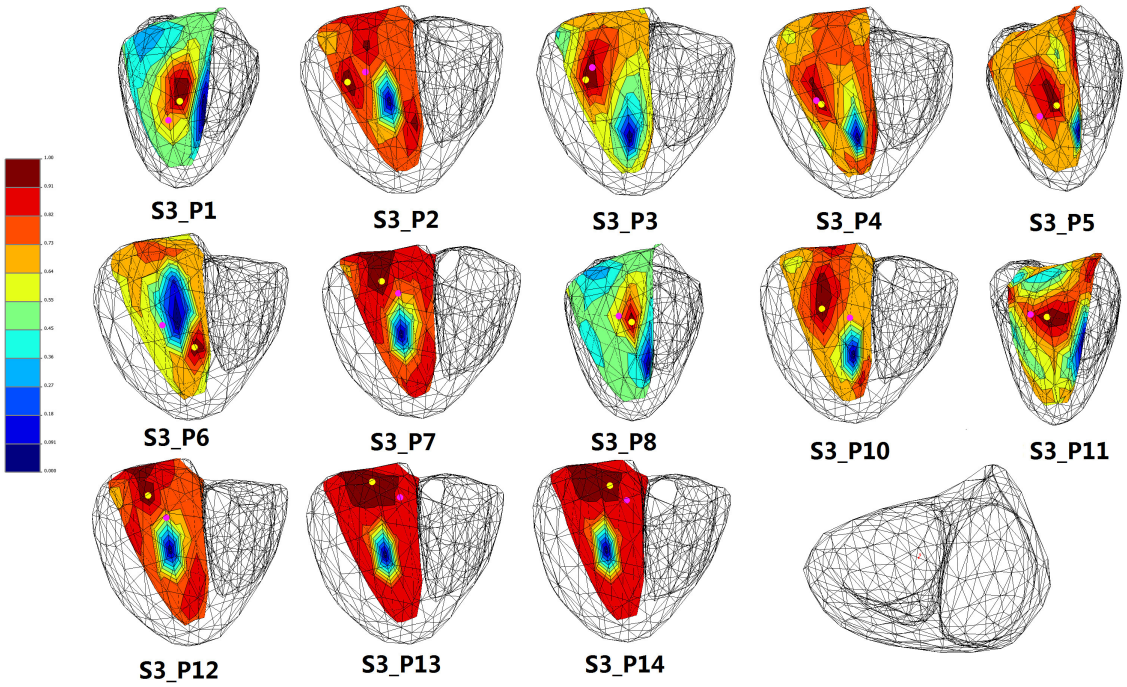

Figure 5.6: Subject #3: Normalized inverse-solution maps generated by the proposed method for LV endocardial pacing. The same format as in Fig. 5.4; there were 14 pacing sites for this subject, with one in the septal region; for each non-septal site, there is a panel showing an inverse-solution map and the last panel shows location of a single septal site.

anatomical regions: septal (S) and non-septal (NS). Apparently, for pacing in the septal region ($n = 10$), localization accuracy is much reduced in comparison with pacing in the rest of the LV ($n = 42$); this finding holds for both inverse-solution methods.

Figures 5.4–5.6 show normalized LV endocardial localization maps during initial 30 ms of the paced activation in three patients with structurally normal ventricular myocardium. The results are shown only for pacing sites outside septal region (NS). The actual pacing sites are indicated by the purple dot and the estimated sites by the yellow dot. The last panel of each figure shows the septal pacing sites with large localization error.

5.5 Discussion and Conclusions

The present study demonstrates that non-invasive localization of LV endocardial pacing sites using the sparse Bayesian learning (SBL) approach based on the EDL-source model is feasible and accurate. In this study, the forward sub-matrix A_{LV} relates the surface distribution of transmembrane potential on the LV endocardial surface to the body-surface potentials. This requires fewer operations to solve the inverse problem than the one using the potential formulation. The sparse Bayesian learning mechanism is able to make use of actually recorded data to guide the search for appropriate *a priori* constraints. Any unnecessary parameters are automatically forced to zero by the ARD model. The solutions obtained by the proposed method compared favorably with those obtained by Erem and co-workers [85], who used the same clinical data for LV endocardial pacing sites of three subjects ($n = 52$).

In summary, the results of both *in vivo* and *in silico* experiments presented in this Chapter provide a strong incentive for pursuing further investigations and clinical applications of data-driven Bayesian methods in the electrocardiographic imaging.

Chapter 6

Machine Learning *vs.* Multiple Linear Regression

6.1 Introduction

In the early 1980s, it was demonstrated that the 12-lead ECG produced by endocardial pacing can be helpful in identifying the pacing region in patients with and without organic heart disease [139, 140]; subsequently, various algorithms for localizing the origin of activation have been developed from extensive data accumulated in human studies [141, 142, 143, 144, 145, 146, 147]. With one notable exception [145], localization algorithms used discrete anatomical regions to subdivide LV endocardial surface and then to identify the region of most-likely origin of activation. All these previous studies suffered from unsatisfactory resolution; typically, there were 9–10 ventricular segments, each with an area of about 10 cm^2. In our laboratory, we use discrete localization into 16 LV segments, combined with much finer *continuous* localization using a multiple linear regression (MLR) and a generic LV geometry (Figs. 6.1 and 6.2). Our localization method can be used *during* the clinical procedure to find rapidly and accurately sites of activation origin from the 12-lead ECG [51].

The purpose of the study presented in this Chapter was to further explore the continuous-localization approach using the generic LV endocardium. In particular, we assessed two machine-learning techniques—Random-Forest Regression (RFR) [52, 53] and Support-Vector Regression (SVR) [54]—to further investigate intrinsic relationships in the clinical data used by the previous study [51] and to consider applicability of these techniques to the localization of focal ventricular activation.

6.2 Methods

6.2.1 Study population

The study population consisted of 38 patients who underwent the LV endocardial catheter ablation; detailed description of this population is in Appendix C.1.1. A

total of 1,012 LV pacing sites with known coordinates and their corresponding 12-lead ECG constituted a clinical dataset for the present study.

6.2.2 Data description

In the present study, coordinates of each pacing-site $X_j, Y_j, Z_j, j = 1, \ldots, n$ ($n = 1,012$), in the coordinate system of the generic LV endocardium, are considered dependent variables. Predictor variables were extracted from ECG data as follows: For all pacing sites ($n = 1,012$), one representative paced beat was selected in the corresponding 12-lead ECG, and a time integral of the QRS complex ($\int$QRS, in microvolt-seconds) was calculated over the initial 120 ms for the 8 leads (II, III, V1–V6) [51]; dimensionless predictor variables, $V_{j:i}, j = 1, \ldots, n$ ($n = 1,012$); $i = 1, \ldots, k$ ($k = 8$), were then derived by normalizing by the total signal energy of the constituent leads.

6.2.3 Electrophysiology study and ablation

The EP study was performed in the usual manner, as described in Appendix C.2.1.

6.2.4 ECG acquisition and processing

For 18 patients, the Dalhousie standard BSPM protocol was used to record simultaneously 120 ECGs (Appendix B.1). For 20 additional patients, only 8 leads of the 12-lead ECG were acquired via Cardiolab system (GE Healthcare, Piscataway, NJ), sampled at 1000 Hz with 16-bit resolution, and recorded for 15 seconds during VT, sinus rhythm or pacing. For each representative paced beat, a time integral of the QRS complex ($\int$QRS, in microvoltseconds), was calculated over the initial 120 ms of the QRS complex as an optimal interval of integration for the $\int$QRS, according to Sapp *et al.* [51].

6.2.5 Generic model of the left-ventricular endocardium

Anatomical sections of the normal human ventricular myocardium were used to construct a generic LV endocardial surface (Appendix A.2). The generic model consists of 238 triangular area elements; three Cartesian coordinates X, Y, and Z specify each triangle's vertices, in the coordinate system with the origin at the LV (epicardial)

apex and the Z axis oriented toward mid-point of aortic valve. Polar projection of this generic LV endocardium (bull's-eye display) is shown in Fig. 6.1; Fig. 6.2 shows a view of the LV endocardium stylized after Miller *et al.* [141].

6.2.6 Registration of pacing sites

Fig. 6.3 shows patient-specific 3D Carto© electroanatomic images of the LV endocardium with 16 ventricular segments demarcated on the image of patient's endocardial surface by means of Carto© software. For each patient, pacing sites were registered from the patient-specific 3D Carto© electroanatomic image onto the generic LV endocardium represented by the 3D model; each pacing site was associated with one of the generic model's 238 triangular area elements (Fig. 6.1). Two observers independently registered pacing sites from the 3D Carto© image (Fig. 6.3) by using anatomical landmarks or visual estimation based on anatomical features. They first demarcated 16 ventricular segments on the image by using Carto© software and then they selected the most appropriate triangle of the generic LV endocardium (Fig. 6.1) for each site.

6.2.7 Multiple Linear Regression (MLR) model

The regression model used in the previous study [51] used generic LV endocardium represented by the 3D surface and to this geometry were fitted three equations of the MLR model with dimensionless predictor variables $V_{:i}, i = 1, \ldots, k$, for $k = 8$. Thus a statistical estimate of pacing-site coordinates $\hat{X}, \hat{Y}, \hat{Z}$ was obtained by fitting three equations

$$\begin{aligned}
\hat{X} &= \hat{\alpha}_0 + \sum_{i=1}^{k} \hat{\alpha}_i V_{:i} + ex; \\
\hat{Y} &= \hat{\beta}_0 + \sum_{i=1}^{k} \hat{\beta}_i V_{:i} + ey; \\
\hat{Z} &= \hat{\gamma}_0 + \sum_{i=1}^{k} \hat{\gamma}_i V_{:i} + ez.
\end{aligned} \tag{6.1}$$

where $V_{:i}$ are the ECG predictor variables, k is the number of predictors, $\hat{\alpha}_i, \hat{\beta}_i, \hat{\gamma}_i, (i = 0, 1, \ldots, 8)$ are the regression coefficients with intercept calculated from the design set,

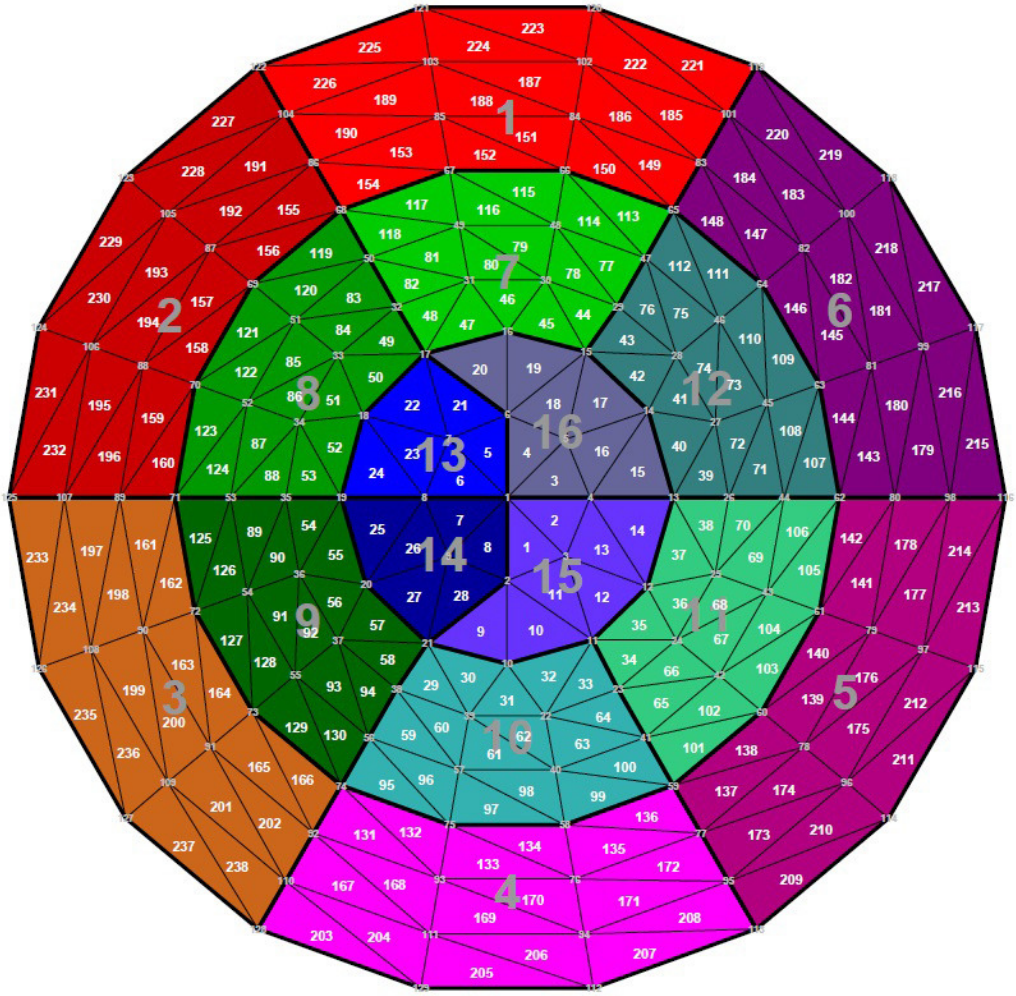

Figure 6.1: Bull's-eye display of the left-ventricular endocardium. Endocardial surface is represented by 238 planar triangles in 3D space and then projected into this polar display; there are 16 anatomical segments, resembling those recommended by the AHA [101], comprising 6 basal segments (1–6), 6 mid-segments (7–12), and 4 apical segments (13–16); basal and mid-segments are denoted, respectively, as anterior, anteroseptal, inferoseptal,inferior, inferolateral, and anterolateral; apical segments are, respectively, anteroseptal, inferoseptal, inferolateral, and anterolateral.

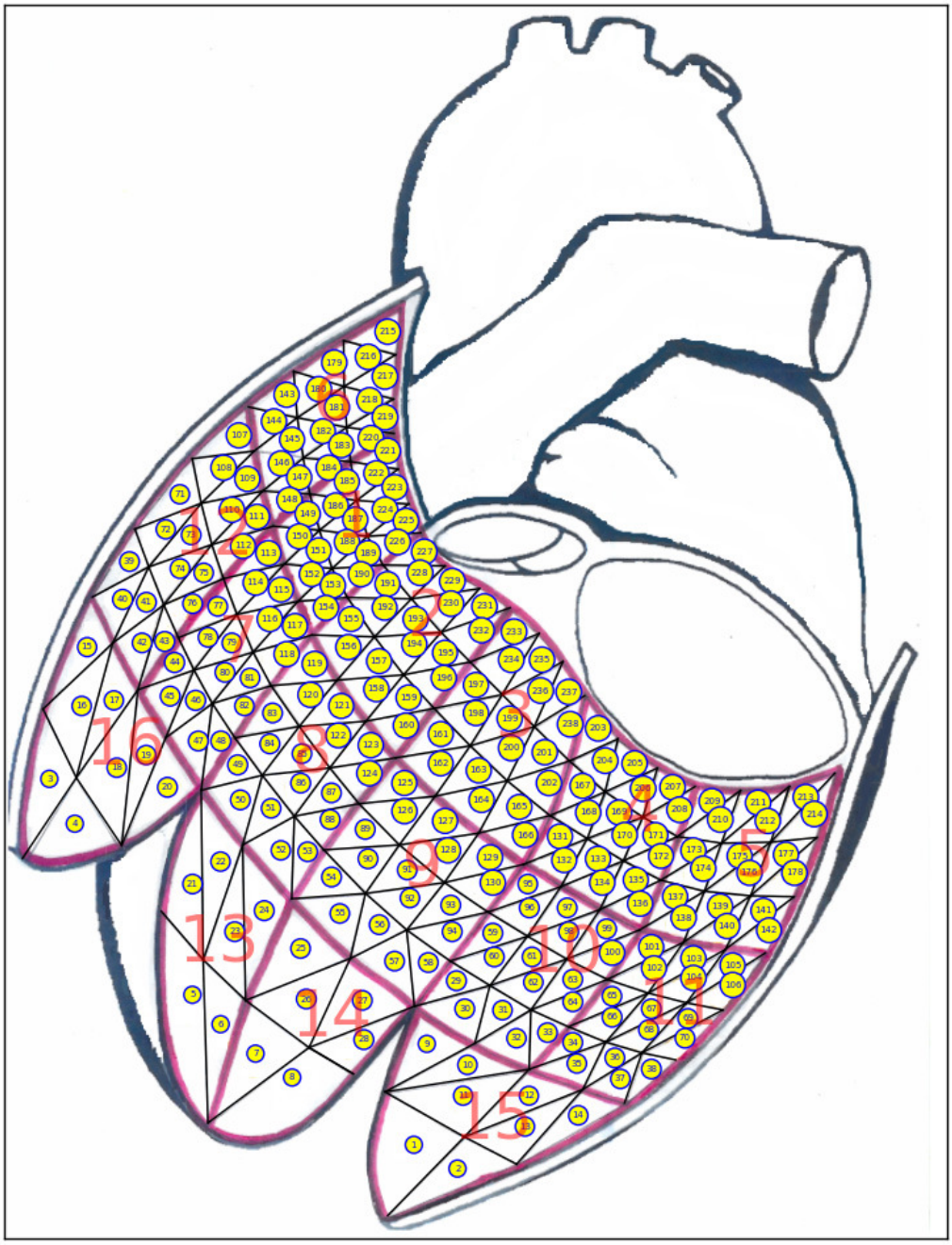

Figure 6.2: Stylized view of the left-ventricular endocardium with 238 triangles and 16 anatomical segments corresponding to Fig. 6.1

and ex, ey, and ez are the residuals. The three equations are used to estimate origin (in Cartesian coordinates) of an *unknown* activation of interest, based on the predictors derived from the known 12-lead ECG recorded on the body surface. The fitting of the MLR model to the generic LV geometry was performed by the R statistical software [148].

6.2.8 Random Forest Regression (RFR) model

The RFR model, first proposed by Breiman [52], is a machine-learning method predicting response variables (such as our pacing-site coordinates $\hat{X}, \hat{Y}, \hat{Z}$) from a set of predictors (such as our dimensionless ECG variables $V_{:i}, i = 1, \ldots, k$) by averaging over multiple decision trees (DTs) created by randomized feature selection and bootstrap aggregation. The RFR is an ensemble method that combines multiple DTs with weak learning output to predict a strong final decision using the mean of all observations.

The RFR is a tree-based algorithm, the crucial part of which is to understand a continuous variable DT [149]. In each DT, the goal is to determine the most predictive branches based on the splitting decision using minimizing residual sum of squares (RSS). However, a DT suffers from high variance and consequently high prediction error. To overcome the variance issue, resampling techniques are used to generate more data. To build many DTs for a forest, the bootstrap with replacement technique creates random samples; for the design set, each DT is trained by roughly 63.2% ((1-1/e)100%) of the design set drawn at random, leaving about 36.8% (100/e%) of the design set "out of bag" (OOB) for determining unbiased estimate of the error. The predictor variables are selected randomly for each node-splitting, which decreases the correlation between trees in the forest, and consequently improves accuracy. Unlike a classical regression tree, un-pruned regression tree is grown fully for each bootstrap sample in random forest. The final outcome is the average of the results of all the trees [52]. To estimate the accuracy of the RFR model, the mean square error (MSE) of the aggregated OOB predictions and the observed responses is calculated [53]

$$MSE_{\text{OOB}} = \frac{1}{m}\sum_{j=1}^{m}(w_j - \hat{w}_j^{\text{OOB}})^2, \tag{6.2}$$

where $w_j \in X_j, Y_j$ or Z_j is the observed response for jth observation from all trees

for which this observation has been OOB, $\hat{w}_j^{\text{OOB}}$ denotes the predicted outcome for the jth OOB case, m is the number of OOB cases. Also, R^2_{OOB} can be obtained as $1-MSE_{\text{OOB}}/(\sum_{i=1}^{n}(w_j-\bar{w})^2)$, where $\bar{w}$ is the mean of the observed outcome of OOB cases.

The "Random Forest" function implemented in the RF package [53] was used to run the RFR model. The required parameters for the RFR model fitting (the number of trees, the number of randomly selected predictor variables at each node) were set by using the 10-fold cross validation with five repetitions based on the grid-search method in the R "caret" package [150]. For each coordinate, the combination of the two parameters with the lowest error metric (root-mean-square (RMS) error) were used for the final optimal parameters.

6.2.9 Support Vector Regression (SVR) model

The SVR [54] model is another machine-learning method for estimating the localization performance. To train the SVR model, a nonlinear function $\varphi(V)$ was used to map the input ECG variables onto an 8-dimensional feature space, for each coordinate separately, as follows

$$g(V) = w \cdot \varphi(V) + b. \tag{6.3}$$

where w is the vector of coefficients, which controls flatness of the function; b is the "bias" term. The quality of estimation is measured by the loss function $L(u, g(V))$, where the u is the actual target. The SVR uses Vapnik's ε-insensitive loss function [151] defined as

$$L_\varepsilon(u, g(V)) = \begin{cases} 0 & \text{if} |u - g(V)| \leq \varepsilon \\ |u - g(V)| - \varepsilon & \text{otherwise} \end{cases}. \tag{6.4}$$

Using the ε-insensitive loss function, $g(V)$ is found that can best approximate the actual target u and has the error tolerance less than ε from the actual incurred targets u for all training data. The SVR tries to reduce model complexity by minimizing norm $\|w^2\|$ flatness. This can be described by introducing (non-negative) slack variables ξ_j, ξ_j^*, to measure the deviation of training samples outside ε-insensitive zone. Thus

the SVR is formulated as minimization of the following functional:

$$\min \frac{1}{2}\|w^2\| + C\sum_{j=1}^{n}(\xi_j + \xi_j^*),$$
$$s.t. \begin{cases} u_j - (w \cdot \varphi(V_{j:}) + b) \leq \varepsilon + \xi_j^* \\ (w \cdot \varphi(V_{j:}) + b) - u_j \leq \varepsilon + \xi_j \\ \xi_j, \xi_j^* \geq 0, j = 1, \ldots, n \end{cases} \tag{6.5}$$

where ξ_j and ξ_j^* are the distances of the training set points from the region where the errors smaller than ε are ignored, the index j labels the n training cases, b is a constant, and C is the cost constant. Based on the Eq. 6.5, Fig. 6.4 illustrates the concept of non-linear SVR.

Then, the optimization problem can be transformed into the dual problem [151, 152] that can be expressed as

$$\max_{\alpha_j^*, \alpha_j} \quad \frac{1}{2}\sum_{j,l=1}^{n}(\alpha_j - \alpha_j^*)(\alpha_l - \alpha_l^*)\langle\varphi(V_{j:}) \cdot \varphi(V_{l:})\rangle$$
$$- \varepsilon\sum_{j=1}^{n}(\alpha_j + \alpha_j^*) + \sum_{j=1}^{n} u_j(\alpha_j - \alpha_j^*)$$
$$s.t. \begin{cases} \sum_{j=1}^{n}(\alpha_j - \alpha_j^*) = 0 \\ 0 \leq \alpha_j^* \leq C, \quad j = 1, \ldots, n \\ 0 \leq \alpha_j \leq C, \quad j = 1, \ldots, n \end{cases} \tag{6.6}$$

where α_j^*, α_j are Lagrange multipliers. The "kernel function" $K(V_{j:}, V_{l:}) = \langle\varphi(V_{j:}), \varphi(V_{l:})\rangle$ is used for computations in input space for each estimated coordinate. Finally, the decision function of nonlinear SVR with the allowance of the kernel function is expressed as

$$g(v) = \sum_{j=1}^{n_{\mathrm{SV}}}(\alpha_j - \alpha_j^*)K(V_j, V) + b \tag{6.7}$$

where n_{SV} is the number of Support Vectors (SVs).

In this study, the Gaussian radial basis function (RBF) kernel was employed to separate the input ECG data into a hyperspace. The SVR model was tuned for each pacing site coordinate by optimizing three parameters (the cost constant C, the radius of the insensitive tube ε and the kernel parameter) by means of the grid search

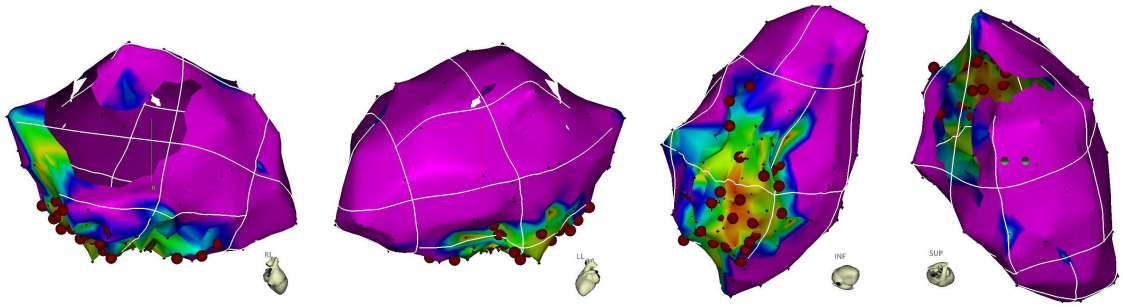

Figure 6.3: Three-dimensional Carto© image of the LV endocardium with manually added division into anatomical segments for a selected case. The LV endocardial surface is first divided into 16 segments (shown in polar projection in Fig 6.1) and then the location of pacing sites is estimated as triangle numbers of the generic LV-endocardial model. For views of the LV endocardial surface are (from left to right): right lateral, left lateral, inferior, and superior.

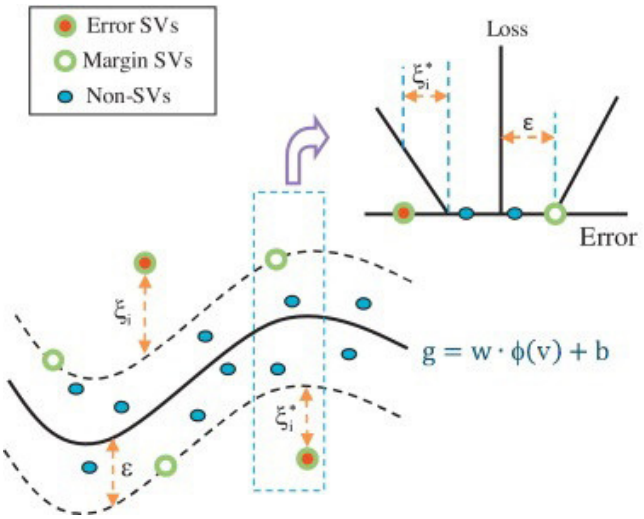

Figure 6.4: Nonlinear SVR with Vapnik's ε-insensitive loss function [54].

method in the R "caret"package [150]. To accomplish this optimization, ten random partitions of the training data with five repetitions were used for cross-validation of the model. Finally, the combination of three parameters resulting in the lowest root-mean-square (RMS) error was selected for the final model.

6.2.10 Modeling assessment for each coordinate

To compare MLR, RFR, and SVR models [148], R statistical software was used. To estimate the localization performance of each model, the entire dataset ($n = 1,012$) was partitioned at random into a design set with 80% of the entire set ($n = 810$) and a test set with the remaining 20% of the entire set ($n = 202$). For the cross validation, a 10-fold cross-validation scheme with 5 repetitions was applied to ensure model stability and reliability using the "caret" R Package [150]. Each model's ability to predict the Cartesian coordinates of pacing sites was assessed by three measures of predictive performance based on differences between predicted and observed values. 1) the coefficient of determination (R^2); 2) root mean squared error (RMSE); and 3) symmetric mean absolute percentage error (SMAPE). They were calculated as follows

$$R^2 = 1 - \frac{\sum_{i=1}^{n}(O_i - P_i)^2}{\sum_{i=1}^{n}(O_i - \bar{O})^2}, \tag{6.8}$$

$$RMSE = (\frac{1}{n}\sum_{i=1}^{n}(P_i - O_i)^2)^{1/2}, \tag{6.9}$$

$$SMAPE = \frac{1}{n}\sum_{i=1}^{n}\frac{|O_i - P_i|}{(|O_i| + |P_i|)/2}, \tag{6.10}$$

where n is the number of samples in the design set, O is the true/observed value, and P is the predicted value.

Bootstrap trials with replacement were used to get for each regression model distributions of predicted coordinates for the left-over sample ($n \simeq N/\mathrm{e}, N = 1,012$) to estimate errors to be expected for the future study population.

6.2.11 Prediction accuracy

Once the best-fitting coefficients were found for each regression model from the design set, they were applied as constants with the ECG predictor variables of an independent test set to get the estimated coordinates $\hat{X}_e, \hat{Y}_e, \hat{Z}_e$ of known pacing sites. The

triangle of the generic LV-endocardial surface with the smallest geodesic distance of its centroid from $(\hat{X}_e, \hat{Y}_e, \hat{Z}_e)$ was found and coordinates of its centroid $(\hat{X}_c, \hat{Y}_c, \hat{Z}_c)$ marked the estimated pacing/exit site on the generic LV-endocardial surface. The geodesic distance between $(\hat{X}_c, \hat{Y}_c, \hat{Z}_c)$ and the centroid of known pacing-site triangle (X_p, Y_p, Z_p), measured on the generic LV-endocardial surface, was approximated as an arc length on the sphere. The mean and standard deviation (SD) of this quantity provided a measure of localization accuracy in the test set.

6.2.12 Quantitative assessment

The statistical inference of each regression model was assessed by using the bootstrap method with replacement [153]. To estimate the optimistic bias of the regression model, the mean error with standard deviation was calculated and applied to the entire original sample ($n = 1,012$) and to the left-over sample ($n \simeq N/\mathrm{e}, N = 1,012$), which served as a test set. Localization error measured as geodesic distance in mm was calculated for each pacing site. The standard error was used to construct the 95%-confidence interval of the localization performance.

6.3 Results

6.3.1 Assessment based on the design set

This assessment was based on the comparison of three error measures of the models' ability to estimate spatial coordinates of the pacing sites using ECG variables as predictors (Table 6.1). As can be ascertained from this table, the SVR performed consistently better than the other two models, achieving lower RMSE and SMAPE values, higher R^2 values, and lower localization error measured as a geodesic distance between the estimated and actual pacing site. The pairwise t-test was used to assess significance of performance differences among three models for each of coordinates: SVR was significantly more accurate than the other two models in the design set, as shown in Fig. 6.5 (upper panel), both in comparison with the MLR ($P< 0.00001$), and with the RFR ($P< 0.00001$) for all three coordinates. In Fig. 6.5 (upper row), the RFR was significantly better than the MLR ($P< 0.00001$) for all three coordinates. Frequency distribution of pacing-site localization error in the generic LV-endocardial

model for the design set ($n = 810$) achieved by the SVR model is in Fig. 6.6 for the localization error measured as geodesic distance.

Table 6.1: Model validation based on the design set

Model	X axis			Y axis			Z axis			Localization Error
	RMSE	SMAPE	R^2	RMSE	SMAPE	R^2	RMSE	SMAPE	R^2	Mean ± SD (mm)
MLR	7.229	0.152	0.540	7.524	0.209	0.621	11.693	0.060	0.652	12.9 ± 8.7
RFR	6.625	0.148	0.614	6.647	0.191	0.704	10.323	0.050	0.729	12.2 ± 8.5
SVR	5.294	0.119	0.753	5.663	0.152	0.785	8.711	0.039	0.807	9.1 ± 8.0

Three measures of error were calculated: RMSE, root mean square error; SMAPE, symmetric mean absolute percentage error; and R^2, the coefficient of determination. Accuracy of localization in terms of Geodesic distance from the predicted node to the pacing-site node in the Prototype LV endocardial surface is given as Mean, standard deviation (SD).

6.3.2 Assessment based on the test set

Table 6.2 presents model performance statistics for the external validation using the test set ($n = 202$). The results resemble (with only one exception) those obtained for the design set. The SVR performed better than the other two models, achieving consistently lower RMSE and SMAPE values, higher R^2 values, and lower localization error measured as a geodesic distance. In Fig. 6.5 (lower panel), the SVR and RFR were significantly more accurate in the test set than the MLR for all three coordinates in terms of the mean error for each pair of three methods (SVR *vs.* MLR ($P< 0.00001$), RFR *vs.* MLR ($P< 0.00001$)). However, for the Y, and Z coordinates, the SVR is not significantly more accurate than the RFR model. Frequency distribution of pacing-site localization error in the generic LV-endocardial model for the test set ($n = 202$) achieved by the SVR model is shown in Fig. 6.7 for the error measured as geodesic distance.

6.3.3 Localization performance based on bootstrap assessment

To further assess the localization performance of regression models on the generic LV endocardial surface, the bootstrap method with replacement using 1,000 trials was used [153]. Table 6.3 shows—for each dependent variable X, Y, Z separately—the localization performance in the left-over sample ($n \simeq N/\mathrm{e}, N = 1,012$). The SVR

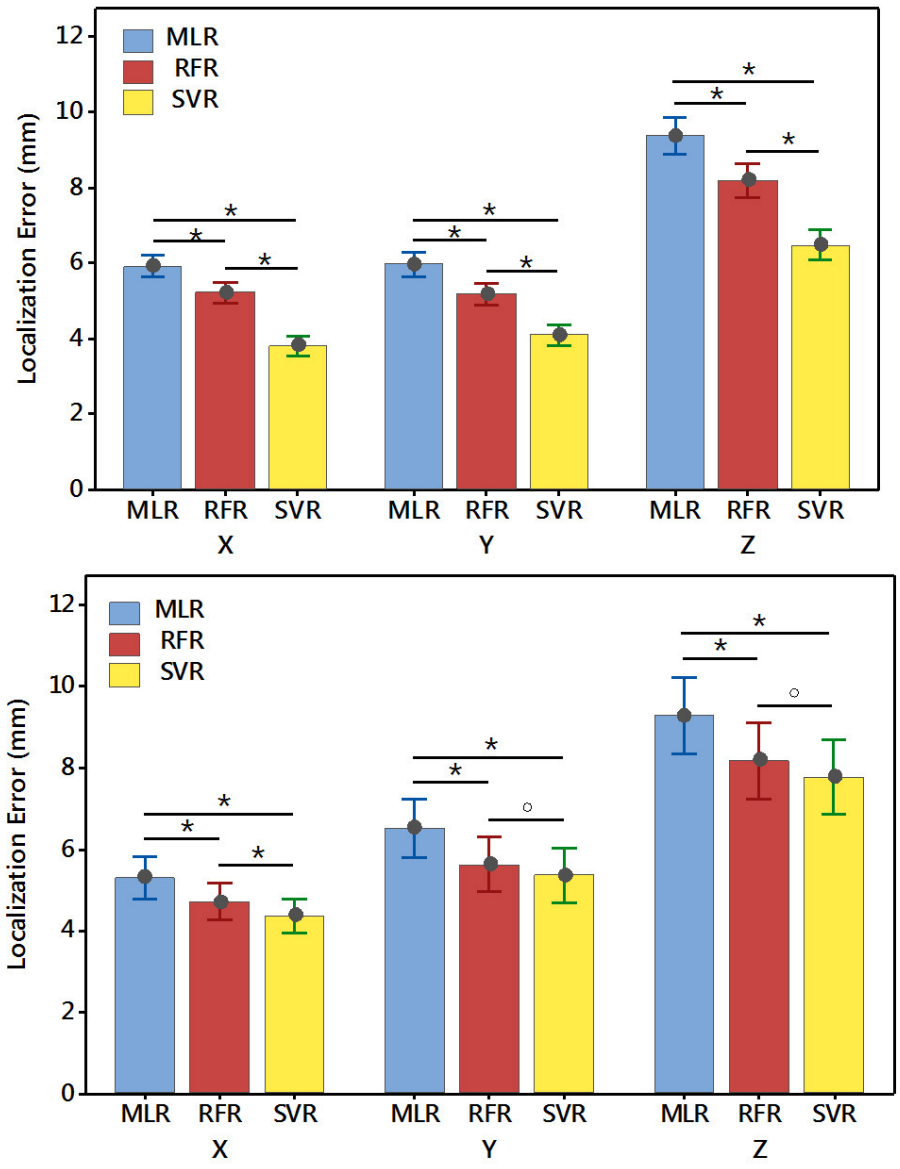

Figure 6.5: Upper panel: Comparison of three regression models applied to the design set ($n = 810$) for three dependent variables (coordinates X, Y, Z). Lower panel: Comparison applied to the test set ($n = 202$) for three dependent variables. Asterisk '$*$' denotes significant difference (P<0.05); '$\circ$' denotes non-significant (NS) difference.

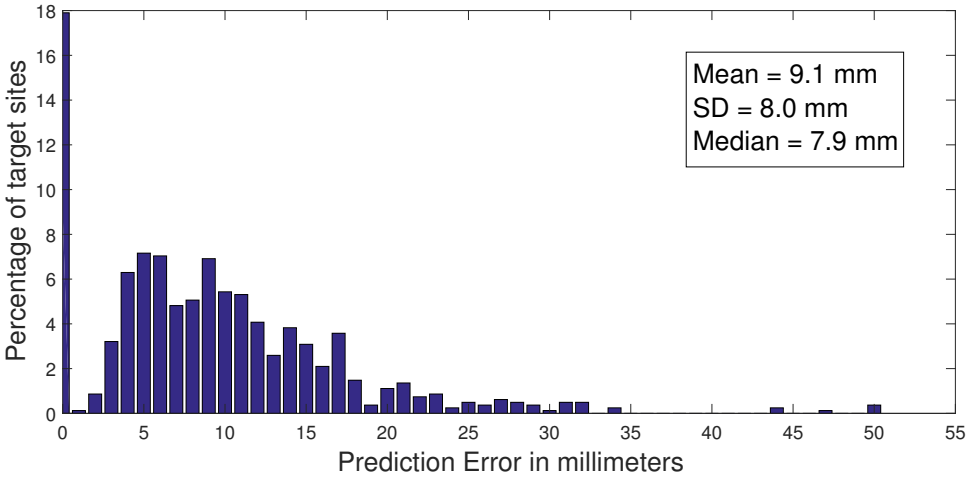

Figure 6.6: Frequency distribution of pacing-site errors on the generic LV-endocardial surface for the design set, achieved by SVR model with 8 ECG predictor variables. Error was measured as geodesic distance (approximated by the arc length) between the tip of prediction vector and the vertex of target triangle on the LV endocardial surface.

Table 6.2: Model validation based on the test set

Model	X axis			Y axis			Z axis			Localization Error
	RMSE	SMAPE	R^2	RMSE	SMAPE	R^2	RMSE	SMAPE	R^2	Mean ± SD (mm)
MLR	6.531	0.144	0.575	8.325	0.201	0.579	11.487	0.057	0.662	12.1 ± 8.1
RFR	5.735	0.138	0.672	7.440	0.181	0.664	10.247	0.048	0.709	12.1 ± 9.0
SVR	5.323	0.132	0.718	7.269	0.170	0.679	10.650	0.046	0.731	11.1 ± 8.1

Measures of error are the same as in Table 6.1.

model had the best performance. Table 6.4 shows that for each coordinate the mean localization error obtained by the SVR was in comparison with that obtained by the MLR significantly lower, both in the entire sample ($n = 1,012$) and in the left-over sample ($n \simeq N/\mathrm{e}, N = 1,012$). Table 6.5 shows the results of 1,000 bootstrap trials with replacement for the localization error in terms of geodesic distance between predicted and actual pacing site, measured on the generic LV endocardial surface. Bootstrap distributions of pacing-site localization error in terms of geodesic distance on the generic LV-endocardial surface for the entire sample ($n = 1,012$) and for the left-over sample ($n \simeq N/\mathrm{e}, N = 1,012$) achieved by the SVR model and by the MLR are in Figs. 6.8 and 6.9.

6.4 Discussion and Conclusions

The purpose of this study was to further investigate the regression approach introduced in [51], for predicting the site of origin of LV activation on a generic left ventricular endocardial surface, by comparing three statistical prediction models: multiple linear regression (MLR), random forest regression (RFR), and support vector regression (SVR). The localization performance of each model was assessed using a large set of ECGs corresponding to known pacing sites.

The performance comparison of regression models showed that consistent (albeit modest) improvement in localization accuracy can be achieved by non-parametric SVR and RFR models, in comparison with MLR model. This gain in accuracy is most likely due to the existence of a non-linear relationship between the pacing-site coordinates and the ECG predictors, which MLR could not adequately resolve.

The MLR is a frequently used statistical model, owing largely to its simplicity and the interpretability of the estimated parameters, which can be easily implemented for the real-time localization of ventricular activation on the generic LV. The RFR model showed a localization performance comparable to the MLR model. The principal result of the present study is that the SVR model shows a significantly higher predictive ability than the MLR model. We have shown that by using the SVR model, the origin of ventricular activation can be localized with mean accuracy of 10.2 mm from the endocardial site of activation origin. The "population" coefficients generated by the SVR model from our design set are superior to the previously-derived coefficients

Table 6.3: Accuracy of pacing-site localization on the generic LV endocardial surface achieved by MLR RFR, and SVR models using ECG predictors: Left-over sample

Model	Coordinates	Variable	Mean	SD	Median	5^{th} Pctl	95^{th} Pctl
MLR	X	gmean	5.86	0.17	5.85	5.52	6.20
		gsd	4.14	0.13	4.15	3.87	4.40
		gmedian	5.12	0.25	5.12	4.64	5.64
	Y	gmean	6.14	0.19	6.14	5.76	6.51
		gsd	4.79	0.20	4.79	4.40	5.21
		gmedian	5.08	0.25	5.08	4.59	5.60
	Z	gmean	9.42	0.29	9.41	8.86	10.00
		gsd	7.05	0.23	7.05	6.60	7.50
		gmedian	7.96	0.39	7.95	7.20	8.72
RFR	X	gmean	5.15	0.17	5.15	4.81	5.46
		gsd	3.97	0.16	3.96	3.66	4.25
		gmedian	4.24	0.21	4.24	3.83	4.66
	Y	gmean	5.37	0.18	5.37	5.04	5.74
		gsd	4.40	0.22	4.40	3.98	4.81
		gmedian	4.38	0.22	4.37	3.98	4.84
	Z	gmean	8.23	0.28	8.23	7.70	8.81
		gsd	6.48	0.28	6.48	5.90	7.04
		gmedian	6.71	0.35	6.71	6.06	7.40
SVR	X	gmean	4.92	0.17	4.92	4.60	5.26
		gsd	3.99	0.17	3.99	3.65	4.32
		gmedian	3.90	0.22	3.90	3.47	4.34
	Y	gmean	5.27	0.19	5.26	4.60	5.26
		gsd	4.44	0.22	4.44	4.01	4.86
		gmedian	4.19	0.22	4.18	3.75	4.66
	Z	gmean	8.03	0.28	8.03	7.49	8.59
		gsd	6.63	0.30	6.63	6.04	7.22
		gmedian	6.38	0.34	6.37	5.73	7.09

Bootstrap method with replacement [153], using 1,000 trials, was used; the entire sample consisted of $n = 1,012$ pacing sites (results not shown); the left-over sample had $n \simeq 1,012/\mathrm{e}$ pacing sites. Three g-variables quantify accuracy of localization by 8-predictor regressions for pacing-site coordinates (X, Y, Z); gmean, mean value; gsd, standard deviation; gmedian, median value; Pctl, percentile.

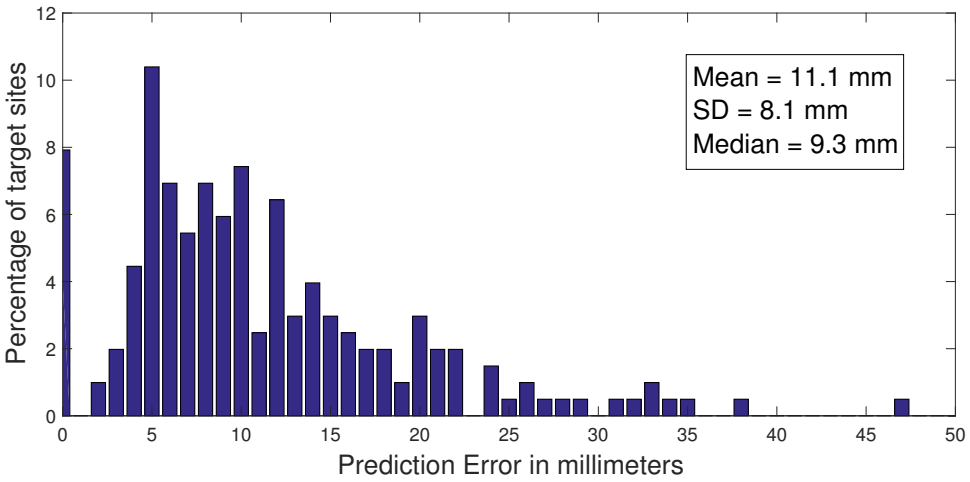

Figure 6.7: Frequency distribution of pacing-site errors on the generic LV-endocardial surface for the test set, achieved by SVR model with 8 ECG predictor variables. Error was measured as geodesic distance between the estimated and the actual pacing site.

Table 6.4: The pairwise t-test for pacing-site coordinates (X, Y, Z) based on the results of Bootstrap method with replacement using 1,000 trials in comparison of MLR and SVR methods

Sample	Coordinates	MLR Mean± SD	SVR Mean± SD	t	p
Entire	X	5.80 ± 0.02	4.22 ± 0.07	23.55	$<.00001^\star$
	Y	6.08 ± 0.02	4.51 ± 0.07	20.63	$<.00001^\star$
	Z	9.35 ± 0.02	6.91 ± 0.09	27.10	$<.00001^\star$
Left-over	X	5.86 ± 0.17	4.92 ± 0.17	3.93	$<.00010^\star$
	Y	6.14 ± 0.20	5.27 ± 0.19	3.22	$<.00138^\star$
	Z	9.42 ± 0.29	8.03 ± 0.28	3.46	$<.00061^\star$

Mean and standard deviation (SD) are in millimeters, Student's t-test results shown as t and p values; $\star$ denotes significant difference ($p \leq 0.05$) between methods; the entire sample consisted of $n = 1,012$ pacing sites, the left-over sample had $n \simeq 1012/\mathrm{e}$ pacing sites.

Table 6.5: Comparative accuracy of pacing-site localization in terms of geodesic distance on the generic LV endocardial surface achieved by SVR and MLR models using ECG predictors

Model	Sample	Variable	Mean (mm)	SD (mm)	Median (mm)	5^{th} Pctl (mm)	95^{th} Pctl (mm)
SVR	Entire (Geodesic)	gmean	10.15	0.15	10.15	9.85	10.43
		gsd	8.50	0.23	8.58	8.17	9.04
		gmedian	8.71	0.14	8.71	8.45	9.07
	Left-over (Geodesic)	gmean	12.00	0.39	12.00	11.27	12.81
		gsd	8.88	0.62	8.87	7.70	10.12
		gmedian	10.22	0.38	10.19	9.57	10.97
MLR	Entire (Geodesic)	gmean	12.72	0.12	12.72	12.49	12.96
		gsd	8.68	0.13	8.68	8.42	8.95
		gmedian	11.08	0.16	11.04	10.79	11.43
	Left-over (Geodesic)	gmean	12.85	0.39	12.85	12.09	13.61
		gsd	8.74	0.52	8.77	7.73	9.73
		gmedian	11.22	0.43	11.21	10.41	12.04

Bootstrap method with replacement [153], using 1,000 trials, was used; the entire sample consisted of $n = 1,012$ pacing sites; the left-over sample had $n \simeq 1012/\mathrm{e}$ pacing sites. Three g-variables quantify accuracy of localization by 8-predictor linear regression in terms of geodesic distance (in millimeters) from the centroid of the predicted triangle to the centroid of the pacing-site triangle in the 238-triangle generic LV endocardial surface; gmean, mean value; gsd, standard deviation; gmedian, median value; Pctl, percentile.

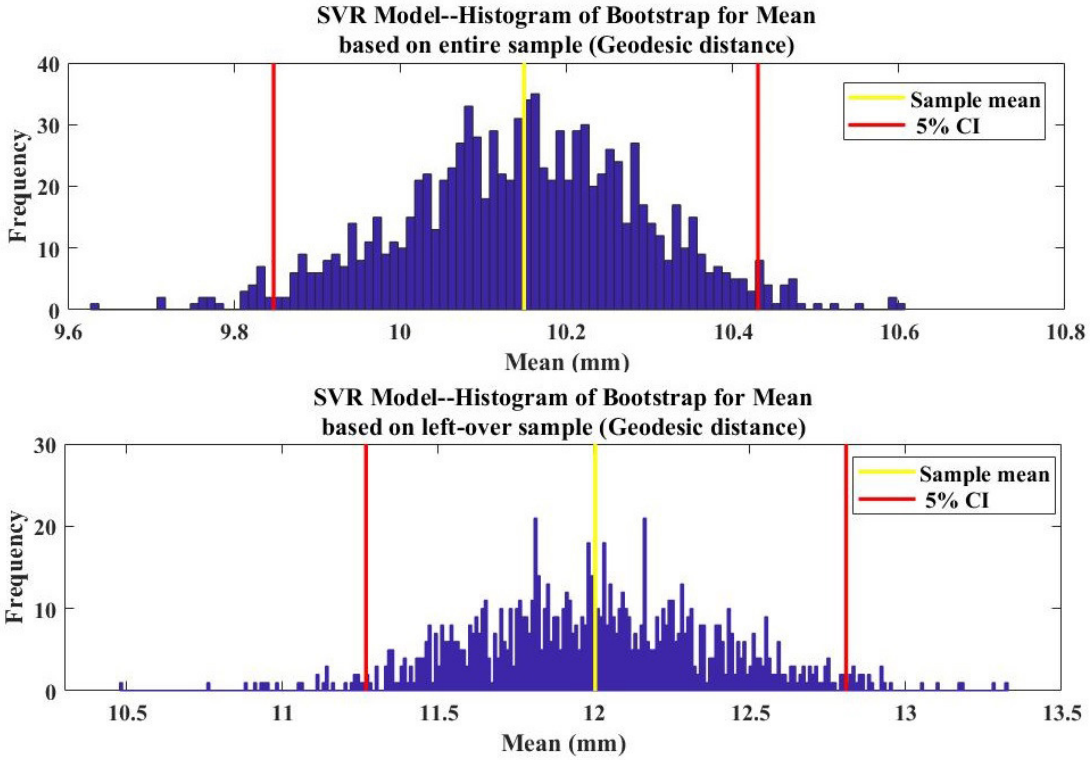

Figure 6.8: Support-vector-machine model: Bootstrap distribution of pacing-site localization error in terms of geodesic distance on the generic LV-endocardial surface for the entire sample ($n = 1,012$), and the left-over sample ($n \simeq N/\mathrm{e}, N = 1,012$). The red reference lines represent a 95% confidence interval; the yellow vertical line is the mean of the bootstrap distribution.

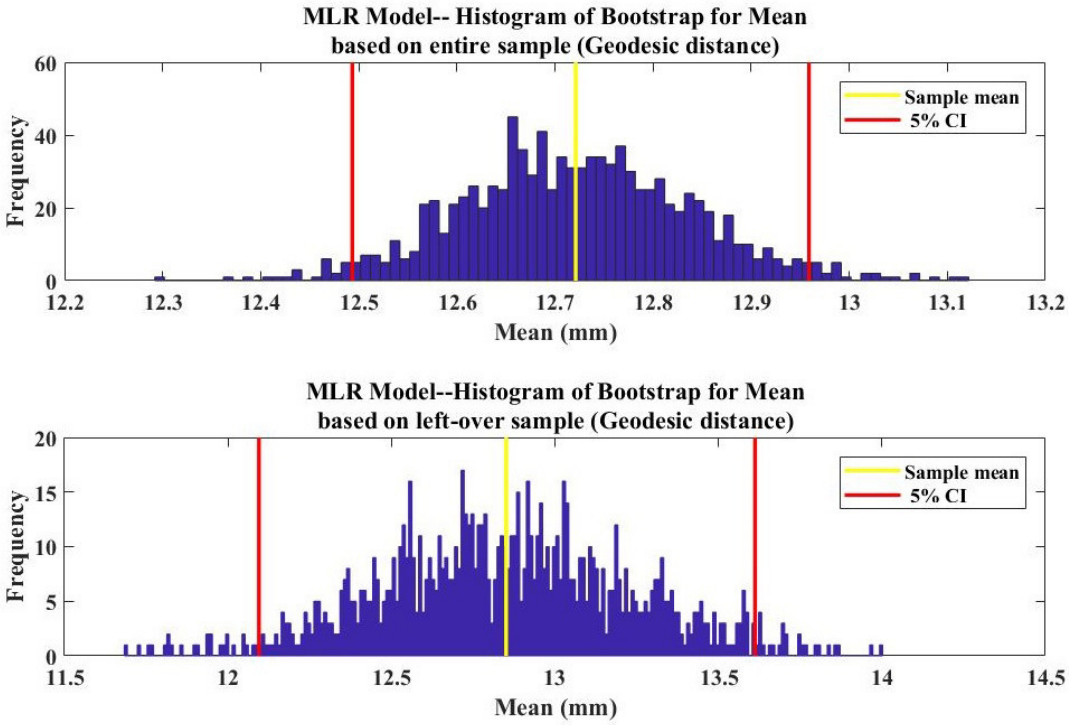

Figure 6.9: Multiple-linear-regression model: Bootstrap distribution of pacing-site localization error in terms of geodesic distance on the generic LV-endocardial surface. Analogous to Fig. 6.8.

generated by the MLR model [51] and can supersede them to improve the real-time localization of ventricular activation on the generic LV endocardial surface.

Chapter 7

Patient-Specific Inverse Solution *vs.* Pace-Mapping

7.1 Introduction

The pre-procedure ECGI methodology can identify sites of epicardial/endocardial pacing with very good accuracy—as shown in Chapters 3 and 5—although accuracy diminishes when pacing is performed over myocardial scar, or over a slowly conducting isthmus (Chapter 3). To achieve such accuracy, however, ECGI requires specialized electrodes for BSPM acquisition, patient-specific geometry acquisition by CT imaging, and time-consuming processing, which make it complex to use in real time to guide catheter-ablation procedure. In an attempt to develop a rapid localization of VT-exit sites for real-time applications, we have previously introduced a novel statistical pace-mapping methodology based on multiple linear regression (MLR) technique and using only the standard 12-lead ECG for pacing sites with known coordinates to localize the origin of ventricular activation [51].

The aim of studies presented in this Chapter is to compare the localization accuracy of the MLR technique with that of the validated inverse solution based on the ℓ_1-norm method [55] (Chapter 3). Although both methods require patient-specific geometry data, the MLR method is using only geometry of the heart surface obtained via catheter during *intra-procedure* electroanatomic mapping, whereas the inverse solution requires *pre-procedure* CT imaging to obtain geometry of both heart- and torso-surface, together with locations of body-surface electrodes.

7.2 Methods

7.2.1 Study population

We studied four patients with recurrent scar-related VT who underwent epicardial catheter mapping and stimulation (79 pacing sites) at the QEII Health Sciences Centre in Halifax, and three patients with structurally normal ventricular myocardium

who underwent endocardial stimulation (52 pacing sites) at the General University Hospital, Charles University, Prague, Czech Republic. (This dataset was contributed by Dr. Petr Šťovíček, and it is available at http://edgar.sci.utah.edu/.) All 7 patients had 120-lead BSPM done according to the Dalhousie protocol, as described in Appendix C.1.2.

7.2.2 Electrophysiology study and ablation

Body-surface electrodes were applied to the patient's torso prior to the ablation procedure, which was performed by using standard techniques [117]. For the epicardial patients, the pericardial space was entered percutaneously [154] and mapped using an electroanatomic non-fluoroscopic system (Carto XP, Biosense Webster, Diamond Bar, CA, USA) described in Appendix C.2.2. For the endocardial patients, the EP study was performed as described in Appendix C.2.1.

7.2.3 Data acquisition and processing

Dalhousie standard BSPM recordings were acquired during pacing at each site (Appendix B.1). Within each recording, a representative paced beat was selected, and the following features were extracted: (1) QRS integral ($\int$QRS), a time integral of the QRS complex in microvoltseconds (μVs); (2) trimmed QRS integral ($\int \mathrm{QRS}_{\mathrm{ms}}$) for inverse calculation, calculated over the initial 30, 40, ... , 80 ms of the QRS complex (denoted as $\int \mathrm{QRS}_{30}$ ... etc.); (3) trimmed QRS integral ($\int \mathrm{QRS}_{120}$) for the statistical method, calculated over the initial 120 ms of the QRS complex of the 12-lead ECG.

7.2.4 Statistical method by multiple linear regressions

The statistical method is based on a linear-regression model with MLR relating ECG predictors (QRS integrals from the independent leads II, III, and V1–V6 of the 12-lead ECG) to the coordinates of activation origin, using 8-variable regression equations with patient-specific coefficients derived from the design set of ECGs corresponding to the *known* pacing sites (with 3D coordinates defined by the electroanatomic system). Once the regression coefficients that best fit (in the least-square sense) the patient's design set are found, they can be linearly combined with the variables generated from the 12-lead ECG of any activation sequence of interest initiated at an *unknown*

site. Thus, the 3D coordinates of an unknown pacing and/or VT-exit site can be calculated from known patient-specific regression coefficients and the ECG variables for the unknown pacing site or activation site of interest [51].

7.2.5 Emulation of clinical protocols

The statistical approach can be implemented in real time using a sweep-operator algorithm [155] (Appendix D) that can then calculate patient-specific regression coefficients for a minimal design set and—as more pacing sites are added to the training set—recalculate them to improve localization accuracy with each added pacing site. With 8 predictor variables, at least $8 + 1$ pacing sites are necessary to render a non-singular system. Therefore, for more safety, patient-specific regression coefficients can be calculated with data acquired by pacing at least 10 known sites. This process was emulated off-line to assess its expected performance in real time.

7.2.6 Inverse-solution method

The forward problem was solved based on the epicardial potential source model as described in Section 2.3.1 of the Chapter 2. For each endocardial patient, we only considered a forward transfer sub-matrix exported from the forward transfer matrix, which directly relating LV endocardial surface to body surface (see details in Section 2.3.3). The ℓ_1-norm regularization method was used to solve the inverse problem (see details in Section 3.2.4 of the Chapter 3). The regularization parameter was determined using the L-curve method [156].

7.2.7 Data analysis of the inverse-solution method

The electroanatomic Carto© map was manually registered and fused with the patient's CT data and pacing sites were projected to the discretized CT heart surface (epicardial surface or endocardial surface) and utilized as the localization gold standard. As a measure of accuracy, the Euclidean distance was calculated for each recording between the earliest computed potential minimum and the actual pacing site projected on the heart surface. For analysis of pacing-site localization, the sites were grouped into 3 categories: sites were characterized as "endocardial", "epicardial", and "pooled". For 2 of 4 patients undergoing epicardial mapping, epicardial

potential distributions of VTs for which an exit site was identified were computed.

7.3 Results

7.3.1 Selection of optimal variables for the statistical localization method

The optimal variables for representing ECG data were derived from 8 independent leads (II, III, V1–V6) of the 12-lead ECG, since the remaining leads are redundant [157]. Following our prior methodology, we chose the first 120 ms of the QRS as an interval of integration for the $\int$QRS variables [51].

7.3.2 Accuracy of localization of pacing sites

Accuracy of pacing-site localization achieved—for each patient separately—by inverse solution for varied integration intervals of input variables (trimmed $\int$QRS) is presented in Table 7.1 The optimal integration intervals of trimmed $\int$QRS are not the same for all patients; they tend to be shorter (about 30–40 ms) for epicardial pacing and longer (70–80 ms) for endocardial pacing. Comparative localization accuracy of the statistical MLR and of the deterministic inverse solution is summarized in Table 7.2 and Fig. 7.1. Table 7.2 shows—for each patient separately—the accuracy of pacing-site localization using the MLR method using $\int \mathrm{QRS}_{120}$ input variables and the inverse-solution method using optimal integration interval input variables. Fig. 7.1 graphically compares the localization accuracy of statistical and deterministic methods for epicardial, endocardial, and pooled pacing sites. For epicardial pacing, the mean localization error of the MLR method was lower than that of the inverse solution (11.2 *vs.* 28.4 mm, P = 0.034). For endocardial pacing, localization by the MLR method also achieved better accuracy than the inverse solution (7.2 *vs.* 19.1 mm, P = 0.017). The pooled localization accuracy of the MLR method was also superior to that achieved by the inverse solution (P = 0.005).

7.3.3 Localization of VT exit sites by the inverse-solution method

For two patients who underwent epicardial mapping, an epicardial VT exit site was identified with contact mapping. The site of successful ablation of VT1 identified by

Table 7.1: Accuracy of pacing-site localization achieved by inverse solution for varied intervals of $\int$QRS derived from BSPM: Patient-by-patient results

Patient #	No. of Pacing Sites	Localization Error based on Inverse Solution Intervals of $\int$QRS					
		30 ms	40 ms	50 ms	60 ms	70 ms	80 ms
1 epi	23	**22.9 ± 13.3**	23.9 ±15.7	23.9 ± 17.4	27.3 ± 17.6	33.5 ± 15.9	38.2 ± 16.7
2 epi	24	35.7 ± 21.9	35.3 ± 21.9	33.2 ± 16.3	**33.0 ± 16.0**	34.9 ± 15.9	33.9 ± 17.9
3 epi	21	23.2 ± 15.2	21.7 ±16.8	**20.8 ± 14.5**	21.6 ± 14.2	21.3 ± 13.7	23.0 ± 14.5
4 epi	10	**31.7 ± 8.5**	36.0 ± 10.2	34.3 ±10.6	34.0 ± 11.0	33.9 ± 11.0	33.0 ± 9.0
5 endo	17	45.3 ± 25.4	31.0 ± 15.0	27.7 ± 8.9	27.4 ± 9.6	24.5 ± 8.8	**23.4 ± 10.5**
6 endo	21	37.2 ± 22.2	22.5 ± 13.9	**16.7 ± 8.3**	17.0 ± 9.6	17.0 ± 10.9	17.8 ± 9.4
7 endo	14	45.6 ± 14.8	34.7 ± 15.2	23.45 ± 12.7	20.0 ± 11.2	19.8 ± 11.4	**17.1 ± 11.7**

Accuracy of localization evaluated for each patient separately in terms of Euclidean distance (mm) from the predicted node to the pacing-site node on the patient-specific epicardial or endocardial surface is given as mean ± standard deviation. Optimal values are in **bold** face.

Table 7.2: Accuracy of pacing-site localization achieved by the MLR method and by the inverse solution: Patient-by-patient results

Patient #	No. of Pacing Sites	MLR Method Localization Error $\int$QRS$_{120}$	Inverse Solution Localization Error
1 epi	23	8.4 ± 9.8	22.9 ± 13.3
2 epi	24	12.7 ± 8.3	33.0 ± 16.0
3 epi	21	16.4 ± 14.2	20.8 ± 14.5
4 epi	10	7.4 ± 5.3	31.7 ± 8.5
5 endo	17	8.7 ± 8.1	23.4 ± 10.5
6 endo	21	5.1 ± 4.5	16.7 ± 8.3
7 endo	14	7.7 ± 13.0	17.1 ± 11.7

The accuracy of pacing-site localization was evaluated for each patient separately using the MLR method and the inverse-solution method using the optimal integration interval $\int$QRS$_{120}$ as input variables. The localization error was calculated for pacing sites of each patient as mean ± standard deviation of estimated distance over epicardial and/or endocardial surface (mm).

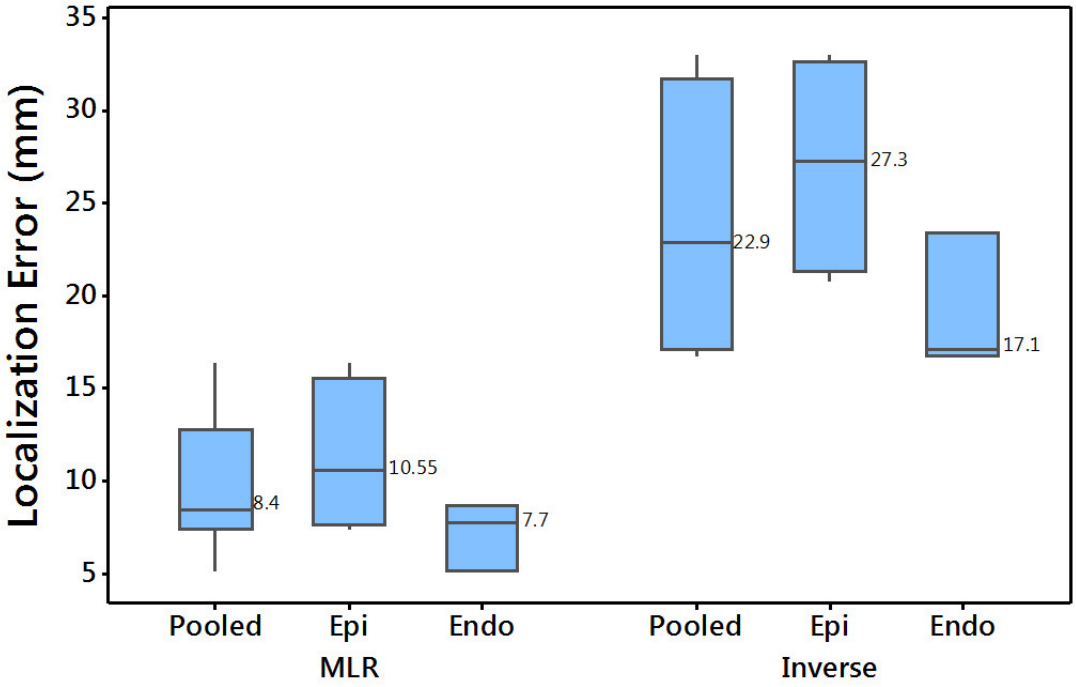

Figure 7.1: Box plots of localization error identified by the proposed MLR method and by the inverse solution. Three plots for each method represent data for pooled pacing sites ($n = 130$), epicaridal pacing sites ($n = 78$), and endocardial pacing sites ($n = 52$). Boxes represent interquartile range, a line inside the box marks the median, and "whiskers" above and below the box indicate the range.

activation- and entrainment-mapping in Patient#1 is shown in Fig. 7.2a; an early potential minimum estimated by the inverse solution from the optimal integration interval ($\int \mathrm{QRS}_{30}$) as input variables appears at the mid-inferolateral LV, which corresponds approximately with the site of successful ablation at a geodesic distance of 24.2 mm (Fig. 7.2b). In Patient#2, the VT exit site was at the basal inferior left ventricle at the scar margin (Fig. 7.2c). Fig. 7.2d shows that the site of early minimum potential on the inverse-solution map during VT2 (yellow dot) is in the same anatomical region as the site of successful ablation (purple dot) registered from the corresponding electroanatomic map, within a geodesic distance of 33.4 mm.

7.3.4 Emulation of real-time localization of the VT exit by the statistical method

To illustrate how the statistical method can be incorporated into actual clinical workflow, we studied two patients who underwent epicardial mapping for VT-exit localization (Fig. 7.3). In these two cases, the 3D coordinates of VT exit sites were identified during the mapping/ablation procedure, based upon activation and entrainment mapping; 8-variable regressions were performed.

Representative Patient#1: This patient's VT1 had cycle length 325 ms, with right-bundle-branch-block-type (RBBB) morphology in lead V1, and a leftward axis (Fig. 7.3A). The site of VT1 exit was identified by activation and entrainment mapping prior to termination by RF application. Using the statistical MLR method, the VT1 exit was localized to the basal inferior LV, achieving accuracy within 10.5 mm after including up to 20 pacing sites in the training set (Table 7.3). The electroanatomic map (Fig. 7.3B) shows the site of VT1 exit identified (yellow arrow); on the corresponding meshed epicardial surface this exit site is marked by a purple dot and estimated site of VT1 exit is marked by a yellow dot.

Representative Patient#2: The exit site of one of two inducible VTs was localized using substrate and pace-mapping techniques; it was ablated with RF delivery at the basal anterolateral presumed entrance site and it was rendered non-inducible. The VT2 had a cycle length of 240 ms, with a left axis, and left-bundle-branch-block morphology (LBBB) (Fig. 7.3C). By directing the catheter to the region of interest and pacing at $\geq$10 sites within the region, patient-specific regression coefficients were

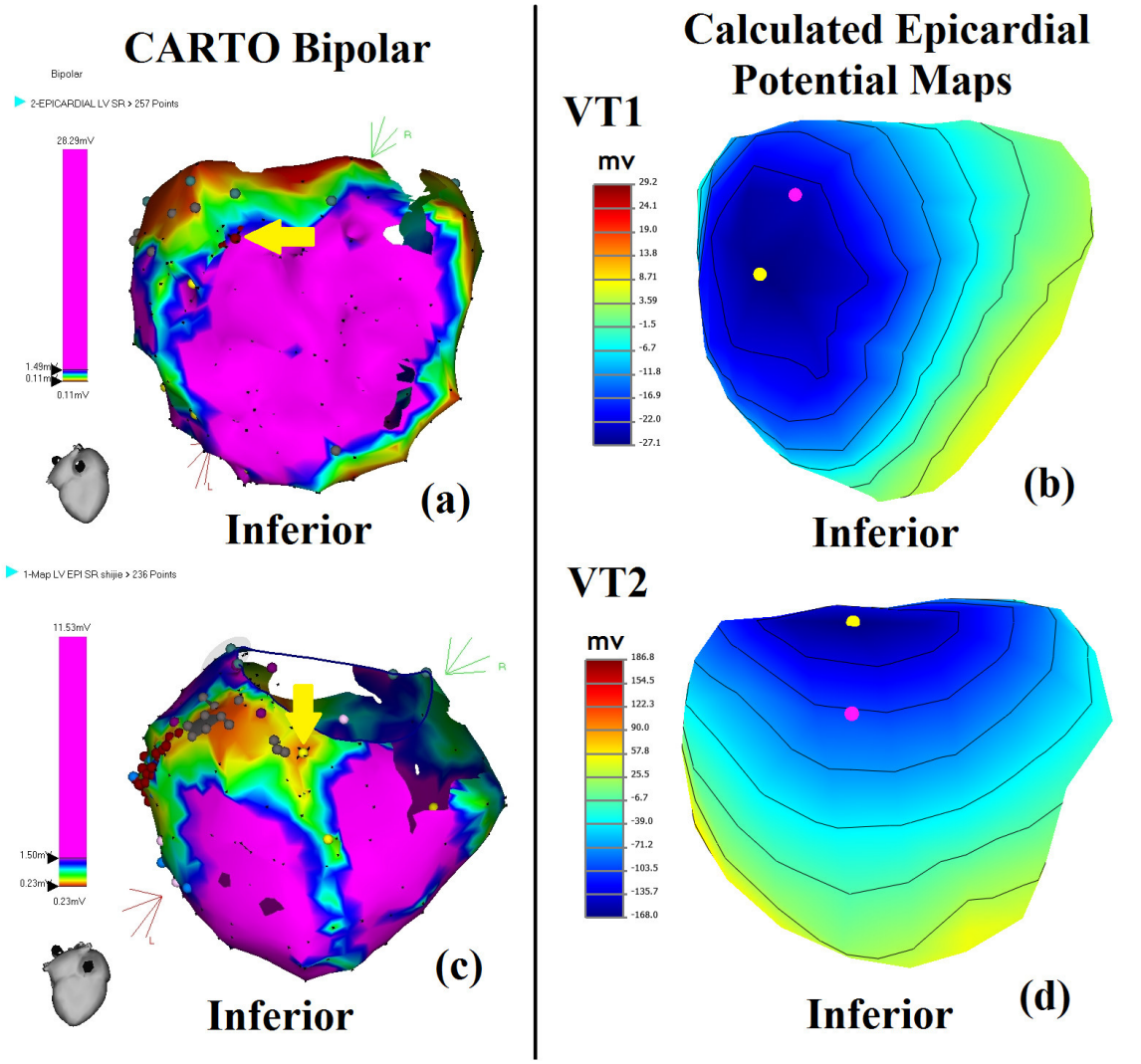

Figure 7.2: Localization of VT exit by inverse-solution mapping for patients #1 and #2. Carto© bipolar maps, inverse epicardial potential maps and isochrones of activation are shown for VT1 and VT2, respectively. The yellow arrow on the Carto© maps in panels (a) and (c) indicates the clinically identified VT exit site, which was registered to the corresponding heart surface geometry in panels (b) and (d) with purple dot; the site of origin of ventricular activation estimated by the inverse solution is shown as yellow dot. Localization error is 24.2 mm for VT1 exit and 33.4 mm for VT2 exit, measured as geodesic distance on epicardial surface.

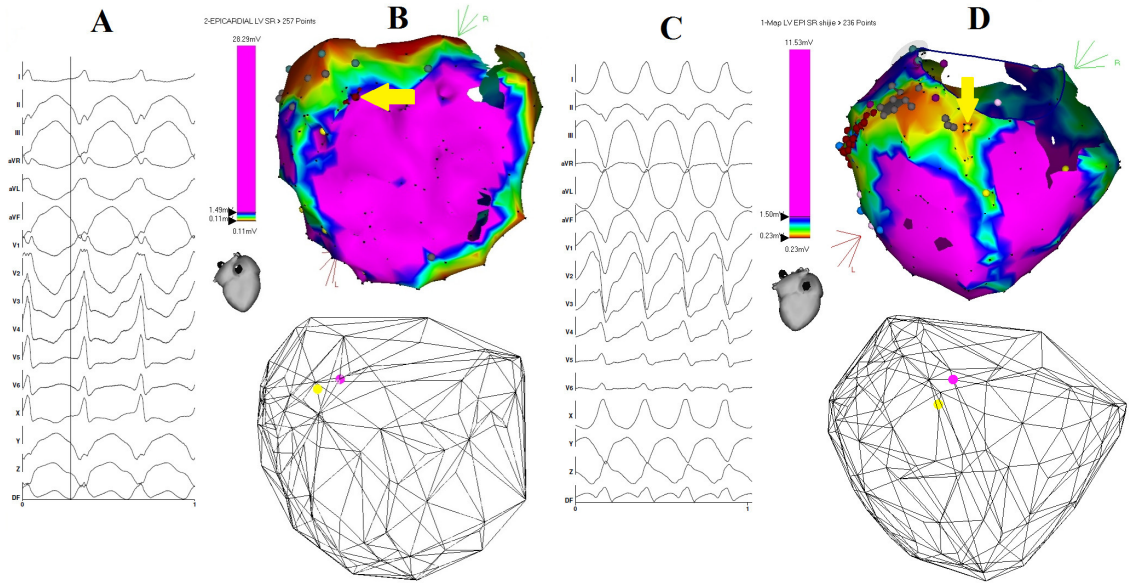

Figure 7.3: Localization of the activation origin by the statistical MLR method. (A) The 12-lead ECG of monomorphic VT1 for Patient#1. (B) Top Carto© map shows the epicardial electroanatomic substrate for this patient, with areas featuring bipolar signal amplitude $\geq$ 1.5 mV in purple, and the site of VT1 exit (identified by contact mapping) depicted by the yellow arrow. Bottom panel shows a corresponding mesh map with the actual site of VT1 exit marked by the purple dot and the site of VT1 exit estimated by the MLR method marked by the yellow dot; localization error of the VT1 exit is 10.5 mm. (C) The 12-lead ECG of monomorphic VT2 for Patient#2. (D) The actual site of VT2 exit (identified by activation and entrainment mapping) and estimated site of VT2 exit for this patient are marked analogously to sites in down panel (D); localization error of the VT2 exit is 11.6 mm.

Table 7.3: VT-exit localization by successive regressions for predictors from ECG leads (II, III, V1–V6) and meshed epicardial surface: Patient #1

Number of Neighboring Pacing Sites	Estimated X coordinate	Estimated Y coordinate	Estimated Z coordinate	Distance from VT exit
True VT1	-24.3	-9.0	-42.2	0.0
1 to 10	–	–	–	–
11	12.3	3.8	-49.9	39.5
12	13.0	3.6	-48.6	39.3
13	7.9	2.5	-51.6	35.5
14	1.4	0.9	-53.8	29.9
15	-3.1	-2.3	-49.0	23.2
16	-3.7	-2.7	-48.5	22.5
17	-8.8	-4.2	-48.1	17.2
18	-8.7	-4.2	-48.0	17.3
20	-15.9	-6.0	-47.7	**10.5**

Emulation of the clinical procedure as described in the text. The error of VT-exit localization was calculated as Euclidean distance from the true VT origin (at CARTO x, y, z coordinates -24.3; -9.0; -42.2 mm, measured from the center of epicardial cavity at 42.4; -125.7; 6.6 mm, derived from the patient's exported 257 Carto sinus-rhythm points). Only the first 20 pacing sites (out of available 23) are shown here; the error of VT localization is a measure of convergence of successive estimates.

generated, which were then used to estimate the 3D coordinates of the site of VT2 exit. This estimate became increasingly accurate with the addition of pacing sites within the *region* provisionally identified (by means of MLR using "population coefficients") as the origin of VT2, finally converging to accuracy within 11.6 mm when pacing at the 15^{th} site (Table 7.4). The site of VT2 exit identified by contact mapping and the estimated site are shown in Fig. 7.3D.

Table 7.4: VT-exit localization by successive regressions for predictors from ECG leads (II, III, V1–V6) and meshed epicardial surface: Patient #2

Number of Neighboring Pacing Sites	Estimated X coordinate	Estimated Y coordinate	Estimated Z coordinate	Distance from VT exit
True VT2	-24.1	-31.8	-24.0	0.0
1 to 10	–	–	–	–
11	-2.9	-32.8	-4.0	29.2
12	-5.9	-29.1	-19.8	18.9
13	-11.3	-30.6	-19.9	13.6
14	-12.9	-30.8	-20.7	**11.8**
15	-13.0	-30.8	-20.8	**11.6**

Emulation of the clinical procedure as described in the text. The error of VT-exit localization was calculated as Euclidean distance from the true VT origin (at CARTO x, y, z coordinates -24.1; -31.8; -24.0 mm, measured from the center of epicardial cavity at 42.9; -84.8; -22.8 mm, derived from the patient's exported 236 Carto points gathered during sinus rhythm). Only the first 15 pacing sites (out of available 24) are shown here; the error of VT localization is a measure of convergence of successive estimates; the errors $\leq$ 12.0 mm in **bold** face.

7.4 Discussion and Conclusions

The main purpose of this study was to compare the performance of the statistical MLR method for estimating the site of origin of ventricular activation with the corresponding performance of conventional electrocardiographic inverse solution. The inverse-solution approach requires in our setting 120 body-surface electrodes for ECG acquisition, patient-specific geometry acquisition by CT imaging, and time-consuming processing, which does not make it suitable for guiding in real time a catheter ablation procedure. On the other hand, the statistical MLR method is using just the standard 12-lead ECG and pacing-site coordinates exported from an electroanatomic system

to generate patient-specific regression coefficients; once these coefficients are known, the site of early ventricular activation can be estimated *during* the EP procedure with significantly higher accuracy than that achieved by the inverse solution.

The utility of the 12-lead ECG in localizing the origin of ventricular activation has been assessed previously by Miller *et al.* [141, 143] and by Kuchar *et al.* [142]; their algorithms were limited to patients with anterior and/or inferior infarction and the site of VT origin was determined with relatively coarse resolution. The statistical MLR method directly relates a patient-specific ventricular geometry to the ECG input variables (predictors). Regression equations use patient-specific coefficients calculated *during* the EP study. This method uses a pace-mapping approach to incrementally increase the accuracy of localization as the procedure continues, and in the present study it eventually localized the origin of epicardial activation with mean accuracy of 11 mm and the origin of endocardial activation with mean accuracy of 7.2 mm. Since the MLR approach uses a patient's own LV geometry gathered by the electroanatomic system, it does not require any pre-procedure imaging. The method can be incorporated into a VT ablation procedure, after creation of a 3D heart substrate map and VT induction, pacing at 10 to 20 sites near the presumed VT exit. Two emulations of the clinical procedure demonstrated in this study achieved a mean localization error of 11.1 mm for two tested VT-exit sites. Thus, the statistical patient-specific method of VT-exit localization can potentially simplify substrate ablation for VT and help to increase the efficiency of a catheter-ablation procedure.

Why would a simple pace-mapping method based on the conventional 12-lead ECG surpass the accuracy of sophisticated electrocardiographic imaging? This was a principal question in the editorial comment [158] to the paper by Sapp *et al.* [51]. To answer this question, one should consider that the deterministic inverse-solution approach has to rely on numerous assumptions regarding electrical characteristics of the patient's torso and requires complex imaging techniques to describe torso geometry, whereas the pace-mapping approach gathers all necessary patient-specific information about the patient's torso by experimental means, based on the assumption that the human torso is a linear physical system.

In summary, the results of this study demonstrate that the pace-mapping methodology using real-time MLR calculations based on the conventional 12-lead ECG can

reliably localize the origin of ventricular activation with high accuracy. This localization capability stands out in comparison with the classical electrocardiographic inverse solution, especially because the means of achieving it are much less cumbersome. The proposed rapid method of localizing the origin of ventricular activation may thus offer an attractive supplement and/or alternative to the electrocardiographic inverse solution, making it suitable for real-time applications during clinical catheter ablation.

Chapter 8

Conclusions

For many years, the problems of interest in the field of cardiac clinical electrophysiology have been solved by using deterministic models of the underlying biophysical phenomena, based on hard assumptions regarding model parameters. Driven by the dramatically improved performance of modern computers, more sophisticated statistical modeling techniques have emerged in the machine-learning field. The aim of this dissertation was to take advantage of these recent technological and computational advances and to apply them in development of novel methods for guided therapy of life-threatening cardiac arrhythmias. In particular, the proposed new computational approaches involve improved statistical methods for non-invasive *pre-procedure* planning by electrocardiographic imaging (ECGI) and methods for real-time *intra-procedure* localization of the origin of cardiac electrical activation.

We have shown that the ECGI methodology can provide detailed spatio-temporal information to identify the origin of epicardial/endocardial ventricular activation with very good accuracy when enhanced by the data-driven Bayesian approach. We used the sparse property of the equivalent-double-layer (EDL) model to simplify localization of the origin of activation on left-ventricular endocardium from body-surface potential maps (BSPMs) using the spatio-temporal features of the cardiac action potentials. We also presented an improved method for evaluating the global activation time (GAT). Inverse-solution isochrones yielded by this method correlated closely with known activation maps obtained by contact mapping performed with an electroanatomic mapping system. Finally, we further investigated the regression approach—introduced previously in this laboratory—for predicting the origin of left-ventricular activation by comparing three statistical prediction models: multiple linear regression, random forest regression, support vector regression. The performance comparison of these regression models showed that consistent (albeit modest) improvement in localization accuracy can be achieved by machine-learning models, in

comparison with widely-used linear regression model.

Although we have thoroughly validated the accuracy of proposed methods within the available cohort of patients, future work should involve confirmation of our findings in a separate cohort, to demonstrate whether the accuracy of novel methods is indeed preserved across a broader range of structural heart-disease substrates. The origin of malignant ventricular tachycardia can usually be determined quickly from the conventional ECG and from catheter-acquired maps of low bipolar voltage when infarct scars are small. However, the difficulties arise when scars are large or intramural. To shed more light on these specific clinical problems, further validation of our proposed methods will be necessary in another prospective validation cohort.

Bibliography

[1] A. D. Waller. A Demonstration on Man of Electromotive Changes accompanying the Heart's Beat. *J Physiol.*, 8(5):229–234, Oct. 1887.

[2] W. Einthoven. Ueber die form des menschlichen electrocardiogramms. *Archiv für die gesamte Physiologie des Menschen und der Tiere*, 60(3):101–123, 1895.

[3] W. Einthoven. *Herinneringsbudendedl*, chapter Galvanometrische registratie van het menschelijk electrocardiogram, pages 101–107. Eduard Ijdo, 1902.

[4] W. Einthoven, G. Fahr, and A. De Waart. Uber die Richtung und die manifeste Grosse der Potentialschwankungen im menschlichen Herzen und uber den Einfluss der Herzlage auf die Form des Elektrokardiogramms. *Pflugers Arch. ges. Physiol.*, 150:275–315, 1913.

[5] H. C. Burger and J. B. van Milaan. Heart-vector and leads. *Br Heart J.*, 8(3):157–161, Jul 1946.

[6] H. C. Burger and J. B. van Milaan. Heart-vector and leads. part ii. *Br Heart J.*, 9(3):154–160, Jul 1947.

[7] H. C. Burger and J. B. van Milaan. Heart-vector and leads; geometrical representation. *Br Heart J.*, 10(4):229–233, Oct 1948.

[8] F. N. Wilson, A. G. Macleod, and P. S. Barker. Potential variations produced by the heart beat at the apices of Einthoven's triangle. *Am Heart J.*, 7:207–211, 1931.

[9] F. N. Wilson, F. D. Johnston, A. G. Macleod, and P. S. Barker. Electrocardiograms that represent the potential variations of a single electrode. *Am Heart J.*, 9(4):447–458, 1934.

[10] F. N. Wilson, F. D. Johnston, F. F. Rosenbaum, H. Erlanger, C. E. Kossmann, H. Hecht, H. Cotrim, R. M. de Oliveira, R. Scarsi, and P. S. Barker. The precordial electrocardiogram. *Am Heart J.*, 27(1):19–85, 1944.

[11] C. R. Johnson, R. S. MacLeod, and P. R. Ershler. A computer model for the study of electrical current flow in the human thorax. *Comput. Biol. Med.*, 22(5):305–323, Sep 1992.

[12] J. Malmivuo and R. Plonsey. *Bioelectromagnetism - Principles and Applications of Bioelectric and Biomagnetic Fields*. 1 1995.

[13] D. Durrer and L. H. van Der Tweel. Excitation of the left ventricular wall of the dog and goat. *Ann. N. Y. Acad. Sci.*, 65(6):779–803, Aug 1957.

[14] D. Durrer, R. T. van Dam, G. E. Freud, M. J. Janse, F. L. Meijler, and R. C. Arzbaecher. Total excitation of the isolated human heart. *Circulation*, 41(6):899–912, Jun 1970.

[15] W. T. Miller and D. B. Geselowitz. Simulation studies of the electrocardiogram. I. The normal heart. *Circ. Res.*, 43(2):301–315, Aug 1978.

[16] W. T. Miller and D. B. Geselowitz. Simulation studies of the electrocardiogram. II. Ischemia and infarction. *Circ. Res.*, 43(2):315–323, Aug 1978.

[17] L. J. Leon and B. M. Horáček. Computer model of excitation and recovery in the anisotropic myocardium. I. Rectangular and cubic arrays of excitable elements. *J Electrocardiol*, 24(1):1–15, Jan 1991.

[18] L. J. Leon and B. M. Horáček. Computer model of excitation and recovery in the anisotropic myocardium. II. Excitation in the simplified left ventricle. *J Electrocardiol*, 24(1):17–31, Jan 1991.

[19] L. J. Leon and B. M. Horáček. Computer model of excitation and recovery in the anisotropic myocardium. III. Arrhythmogenic conditions in the simplified left ventricle. *J Electrocardiol*, 24(1):33–41, Jan 1991.

[20] R. Hren, J. Nenonen, and B. M. Horáček. Simulated epicardial potential maps during paced activation reflect myocardial fibrous structure. *Ann Biomed Eng*, 26(6):1022–1035, 1998.

[21] K. Simelius, J. Nenonen, and B. M. Horáček. Modeling Cardiac Ventricular Activation. *International Journal of Bioelectromagnetism*, 3(2):51–58, 2001.

[22] R. L. Lux, C. R. Smith, R. F. Wyatt, and J. A. Abildskov. Limited lead selection for estimation of body surface potential maps in electrocardiography. *IEEE Trans Biomed Eng*, 25(3):270–276, 1978.

[23] R. E. Mason and I. Likar. A new system of multiple-lead exercise electrocardiography. *Am. Heart J.*, 71(2):196–205, Feb 1966.

[24] B. M. Horáček, K. Simelius, R. Hren, and J. Nenonen. *Challenges in Modelling Human Heart's Total Excitation*, pages 39–46. Springer Berlin Heidelberg, Berlin, Heidelberg, 2001.

[25] H.S. Oster and Y. Rudy. Regional regularization of the electrocardiographic inverse problem: a model study using spherical geometry. *IEEE Trans Biomed Eng*, 44(2):188–199, Feb. 1997.

[26] J. L. Sapp, F. Dawoud, J. C. Clements, and B. M. Horáček. Inverse solution mapping of epicardial potentials: quantitative comparison with epicardial contact mapping. *Circ Arrhythm Electrophysiol*, 5(5):1001–1009, Oct 2012.

[27] C. Ramanathan, R. N. Ghanem, P. Jia, K. Ryu, and Y. Rudy. Noninvasive electrocardiographic imaging for cardiac electrophysiology and arrhythmia. *Nat Med*, 10(4):422–428, Apr 2004.

[28] T. Berger, G. Fischer, B. Pfeifer, R. Modre, F. Hanser, T. Trieb, F. X. Roithinger, M. Stuehlinger, O. Pachinger, B. Tilg, and F. Hintringer. Single-beat noninvasive imaging of cardiac electrophysiology of ventricular pre-excitation. *J Am Coll Cardiol*, 48(10):2045–2052, Nov 2006.

[29] Y. Wang, P. S. Cuculich, J. Zhang, K. A. Desouza, R. Vijayakumar, J. Chen, M. N. Faddis, B. D. Lindsay, T. W. Smith, and Y. Rudy. Noninvasive electroanatomic mapping of human ventricular arrhythmias with electrocardiographic imaging. *Sci Transl Med*, 3(98):98ra84, Aug 2011.

[30] J. Zhang, D. H. Cooper, K. A. Desouza, P. S. Cuculich, P. K. Woodard, T. W. Smith, and Y. Rudy. Electrophysiologic scar substrate in relation to VT: Noninvasive high-resolution mapping and risk assessment with ECGI. *Pacing Clin Electrophysiol*, 39(8):781–791, Aug 2016.

[31] M. Rodrigo, A. Climent, A. Liberos, I. Hernandez-Romero, A. Arenal, J. Bermejo, F. Fernandez-Aviles, F. Atienza, and M. Guillem. Solving inaccuracies in anatomical models for electrocardiographic inverse problem resolution by maximizing reconstruction quality. *IEEE Trans Med Imaging*, May 2017.

[32] A. S. Revishvili, E. Wissner, D. S. Lebedev, C. Lemes, S. Deiss, A. Metzner, V. V. Kalinin, O. V. Sopov, E. Z. Labartkava, A. V. Kalinin, M. Chmelevsky, S. V. Zubarev, M. K. Chaykovskaya, M. G. Tsiklauri, and K. H. Kuck. Validation of the mapping accuracy of a novel non-invasive epicardial and endocardial electrophysiology system. *Europace*, 17(8):1282–1288, Aug 2015.

[33] M. Hocini, A. J. Shah, T. Neumann, M. Kuniss, D. Erkapic, A. Chaumeil, S. J. Copley, P. B. Lim, P. Kanagaratnam, A. Denis, N. Derval, R. Dubois, H. Cochet, P. Jaïs, and M. Haïssaguerre. Focal arrhythmia ablation determined by high-resolution noninvasive maps: Multicenter feasibility study. *J Cardiovasc Electrophysiol*, 26(7):754–760, Jul 2015.

[34] R. Dubois, A. J. Shah, M. Hocini, A. Denis, N. Derval, H. Cochet, F. Sacher, L. Bear, J. Duchateau, P. Jaïs, and M. Haïssaguerre. Non-invasive cardiac mapping in clinical practice: Application to the ablation of cardiac arrhythmias. *J Electrocardiol*, 48(6):966–974, 2015.

[35] V. Y. Reddy, M. R. Reynolds, P. Neuzil, A. W. Richardson, M. Taborsky, K. Jongnarangsin, S. Kralovec, L. Sediva, J. N. Ruskin, and M. E. Josephson. Prophylactic catheter ablation for the prevention of defibrillator therapy. *N. Engl. J. Med.*, 357(26):2657–2665, Dec 2007.

[36] C. T. Pedersen, G. N. Kay, J. Kalman, M. Borggrefe, P. Della-Bella, T. Dickfeld, P. Dorian, H. Huikuri, Y. H. Kim, B. Knight, F. Marchlinski, D. Ross, F. Sacher, J. Sapp, K. Shivkumar, K. Soejima, H. Tada, M. E. Alexander, J. K. Triedman, T. Yamada, P. Kirchhof, G. Y. Lip, K. H. Kuck, L. Mont, D. Haines, J. Indik, J. Dimarco, D. Exner, Y. Iesaka, and I. Savelieva. EHRA/HRS/APHRS expert consensus on ventricular arrhythmias. *Heart Rhythm*, 11(10):e166–196, Oct 2014.

[37] K. H. Kuck, A. Schaumann, L. Eckardt, S. Willems, R. Ventura, E. Delacretaz, H. F. Pitschner, J. Kautzner, B. Schumacher, P. S. Hansen, H. K. Jensen, F. Ouyang, P. Milberg, H. Klemm, M. Kuniss, S. H. Hohnloser, C. Israel, M. Horlitz, P. Schley, A. Bauer, K. H. Seidl, M. Strauss, J. Schwab, L. Lickfett, C. Wolpert, S. Spehl, S. Reek, C. Reithmann, and H. Tanner. Catheter ablation of stable ventricular tachycardia before defibrillator implantation in patients with coronary heart disease (VTACH): a multicentre randomised controlled trial. *Lancet*, 375(9708):31–40, Jan 2010.

[38] R. Tung, M. Vaseghi, D. S. Frankel, P. Vergara, L. Di Biase, K. Nagashima, R. Yu, S. Vangala, C. H. Tseng, E. K. Choi, S. Khurshid, M. Patel, N. Mathuria, S. Nakahara, W. S. Tzou, W. H. Sauer, K. Vakil, U. Tedrow, J. D. Burkhardt, V. N. Tholakanahalli, A. Saliaris, T. Dickfeld, J. P. Weiss, T. J. Bunch, M. Reddy, A. Kanmanthareddy, D. J. Callans, D. Lakkireddy, A. Natale, F. Marchlinski, W. G. Stevenson, P. Della Bella, and K. Shivkumar. Freedom from recurrent ventricular tachycardia after catheter ablation is associated with improved survival in patients with structural heart disease: An International VT Ablation Center Collaborative Group study. *Heart Rhythm*, 12(9):1997–2007, Sep 2015.

[39] J. L. Sapp, G. A. Wells, R. Parkash, W. G. Stevenson, L. Blier, J. F. Sarrazin, B. Thibault, L. Rivard, L. Gula, P. Leong-Sit, V. Essebag, P. B. Nery, S. K. Tung, J. M. Raymond, L. D. Sterns, G. D. Veenhuyzen, J. S. Healey, D. Redfearn, J. F. Roux, and A. S. Tang. Ventricular Tachycardia Ablation versus Escalation of Antiarrhythmic Drugs. *N. Engl. J. Med.*, 375(2):111–121, Jul 2016.

[40] K. Soejima, M. Suzuki, W. H. Maisel, C. B. Brunckhorst, E. Delacretaz, L. Blier, S. Tung, H. Khan, and W. G. Stevenson. Catheter ablation in patients with multiple and unstable ventricular tachycardias after myocardial infarction: short ablation lines guided by reentry circuit isthmuses and sinus rhythm mapping. *Circulation*, 104(6):664–669, Aug 2001.

[41] K. Soejima, W. G. Stevenson, W. H. Maisel, J. L. Sapp, and L. M. Epstein. Electrically unexcitable scar mapping based on pacing threshold for identification of the reentry circuit isthmus: feasibility for guiding ventricular tachycardia ablation. *Circulation*, 106(13):1678–1683, Sep 2002.

[42] W. G. Stevenson. Current treatment of ventricular arrhythmias: state of the art. *Heart Rhythm*, 10(12):1919–1926, Dec 2013.

[43] A. Arenal, S. del Castillo, E. Gonzalez-Torrecilla, F. Atienza, M. Ortiz, J. Jimenez, A. Puchol, J. Garcia, and J. Almendral. Tachycardia-related channel in the scar tissue in patients with sustained monomorphic ventricular tachycardias: influence of the voltage scar definition. *Circulation*, 110(17):2568–2574, Oct 2004.

[44] T. Harada, W. G. Stevenson, D. Z. Kocovic, and P. L. Friedman. Catheter ablation of ventricular tachycardia after myocardial infarction: relation of endocardial sinus rhythm late potentials to the reentry circuit. *J. Am. Coll. Cardiol.*, 30(4):1015–1023, Oct 1997.

[45] F. Bogun, E. Good, S. Reich, D. Elmouchi, P. Igic, K. Lemola, D. Tschopp, K. Jongnarangsin, H. Oral, A. Chugh, F. Pelosi, and F. Morady. Isolated potentials during sinus rhythm and pace-mapping within scars as guides for ablation of post-infarction ventricular tachycardia. *J. Am. Coll. Cardiol.*, 47(10):2013–2019, May 2006.

[46] P. Jaïs, P. Maury, P. Khairy, F. Sacher, I. Nault, Y. Komatsu, M. Hocini, A. Forclaz, A. S. Jadidi, R. Weerasooryia, A. Shah, N. Derval, H. Cochet, S. Knecht, S. Miyazaki, N. Linton, L. Rivard, M. Wright, S. B. Wilton, D. Scherr, P. Pascale, L. Roten, M. Pederson, P. Bordachar, F. Laurent, S. J. Kim, P. Ritter, J. Clementy, and M. Haissaguerre. Elimination of local abnormal ventricular activities: a new end point for substrate modification in patients with scar-related ventricular tachycardia. *Circulation*, 125(18):2184–2196, May 2012.

[47] R. Tung, N. Mathuria, Y. Michowitz, R. Yu, E. Buch, J. Bradfield, R. Mandapati, I. Wiener, N. Boyle, and K. Shivkumar. Functional pace-mapping responses for identification of targets for catheter ablation of scar-mediated ventricular tachycardia. *Circ Arrhythm Electrophysiol*, 5(2):264–272, Apr 2012.

[48] P. Santangeli and F. E. Marchlinski. Substrate mapping for unstable ventricular tachycardia. *Heart Rhythm*, 13(2):569–583, Feb 2016.

[49] L. Di Biase, P. Santangeli, D. J. Burkhardt, R. Bai, P. Mohanty, C. Carbucicchio, A. Dello Russo, M. Casella, S. Mohanty, A. Pump, R. Hongo, S. Beheiry, G. Pelargonio, P. Santarelli, M. Zucchetti, R. Horton, J. E. Sanchez, C. S. Elayi, D. Lakkireddy, C. Tondo, and A. Natale. Endo-epicardial homogenization of the scar versus limited substrate ablation for the treatment of electrical storms in patients with ischemic cardiomyopathy. *J. Am. Coll. Cardiol.*, 60(2):132–141, Jul 2012.

[50] L. Di Biase, J. D. Burkhardt, D. Lakkireddy, C. Carbucicchio, S. Mohanty, P. Mohanty, C. Trivedi, P. Santangeli, R. Bai, G. Forleo, R. Horton, S. Bailey, J. Sanchez, A. Al-Ahmad, P. Hranitzky, G. J. Gallinghouse, G. Pelargonio,

R. H. Hongo, S. Beheiry, S. C. Hao, M. Reddy, A. Rossillo, S. Themistoclakis, A. Dello Russo, M. Casella, C. Tondo, and A. Natale. Ablation of Stable VTs Versus Substrate Ablation in Ischemic Cardiomyopathy: The VISTA Randomized Multicenter Trial. *J. Am. Coll. Cardiol.*, 66(25):2872–2882, Dec 2015.

[51] J. L. Sapp, M. Bar-Tal, A. J. Howes, J. E. Toma, A. El-Damaty, J. W. Warren, P. J. MacInnis, S. Zhou, and B. M. Horáček. Real-time localization of ventricular tachycardia origin from the 12-lead electrocardiogram. *J Am Coll Cardiol EP*, 3(7):687–699, 2017.

[52] L. Breiman. Random forests. *Machine learning*, 45(1):5–32, 2001.

[53] A. Liaw and M. Wiener. Classification and regression by Random Forest. *R News*, 2(3):18–22, 2002.

[54] A. J. Smola and B. Scholkopf. A tutorial on support vector regression. *Journal Statistics and Computing*, 14(3):199–222, 2004.

[55] S. Ghosh and Y. Rudy. Application of L1-norm regularization to epicardial potential solution of the inverse electrocardiography problem. *Ann Biomed Eng*, 37(5):902–912, May 2009.

[56] A. C. L. Barnard, I. M. Duck, M. S. Lynn, and W. P. Timlake. The application of electromagnetic theory in electrocardiology. II. Numerical solution of the integral equations. *Biophys J*, 7:463–490, 1967.

[57] R. C. Barr, T. C. Pilkington, J. P. Boineau, and M. S. Spach. Determining surface potentials from current dipoles, with application to electrocardiography. *IEEE Trans Biomed Eng*, 13(2):88–92, Apr 1966.

[58] H. L. Gelernter and J. C. Swihart. A mathematical-physical model of the genesis of the electrocardiogram. *Biophys J*, 4:285–301, 1964.

[59] R. C. Barr, M. Ramsey, and M. S. Spach. Relating epicardial to body surface potential distributions by means of transfer coefficients based on geometry measurements. *IEEE Trans Biomed Eng*, 24(1):1–11, Jan 1977.

[60] B. M. Horáček and J. C. Clements. The inverse problem of electrocardiography: a solution in terms of single- and double-layer sources of the epicardial surface. *Math Biosci*, 144(2):119–154, Sep 1997.

[61] J. J. Cuppen and A. van Oosterom. Model studies with the inversely calculated isochrones of ventricular depolarization. *IEEE Trans Biomed Eng*, 31(10):652–659, Oct 1984.

[62] D. B. Geselowitz. Use of time integrals of the ECG to solve the inverse problem. *IEEE Trans Biomed Eng*, 32(1):73–75, Jan 1985.

[63] G. J. Huiskamp and A. van Oosterom. Tailored versus realistic geometry in the inverse problem of electrocardiography. *IEEE Trans Biomed Eng*, 36:827–835, 1989.

[64] A. van Oosterom and G. J. Huiskamp. The effect of torso inhomogeneities on body surface potentials quantified using "tailored" geometry. *J Electrocardiol.*, 22:53–72, 1989.

[65] J. D. Jackson. *Classical Electrodynamics*. John Wiley & Sons, New York, 1962.

[66] R. Plonsey. *Bioelectric Phenomena*. McGraw-Hill, New York, 1969.

[67] M. S. Lynn and W. P. Timlake. The use of multiple deflations in the numerical solution of singular systems of equations, with applications to potential theory. *SIAM J Numer Anal*, 5(2):303–322, 1968.

[68] A. J. Shah, M. Hocini, P. Pascale, L. Roten, Y. Komatsu, M. Daly, K. Ramoul, A. Denis, N. Derval, F. Sacher, R. Dubois, R. Bokan, S. Eliatou, M. Strom, C. Ramanathan, P. Jaïs, P. Ritter, and M. Haïssaguerre. Body surface electrocardiographic mapping for non-invasive identification of arrhythmic sources. *Arrhythm Electrophysiol Rev*, 2(1):16–22, Apr 2013.

[69] Y. Yamashita and D. B. Geselowitz. Source-field relationships for cardiac generators on the heart surface based on their transfer coefficients. *IEEE Trans Biomed Eng*, 32(11):964–970, Nov 1985.

[70] H. S. Oster, B. Taccardi, R. L. Lux, P. R. Ershler, and Y. Rudy. Electrocardiographic imaging: Noninvasive characterization of intramural myocardial activation from inverse-reconstructed epicardial potentials and electrograms. *Circulation*, 97(15):1496–1507, Apr 1998.

[71] G. F. Ahmad, D. H. Brooks, and R. S. MacLeod. An admissible solution approach to inverse electrocardiography. *Ann Biomed Eng*, 26(2):278–292, 1998.

[72] D. H. Brooks, G. F. Ahmad, R. S. MacLeod, and G. M. Maratos. Inverse electrocardiography by simultaneous imposition of multiple constraints. *IEEE Trans Biomed Eng*, 46(1):3–18, Jan 1999.

[73] B. Messnarz, B. Tilg, R. Modre, G. Fischer, and F. Hanser. A new spatiotemporal regularization approach for reconstruction of cardiac transmembrane potential patterns. *IEEE Trans Biomed Eng*, 51(2):273–281, Feb 2004.

[74] P. M. van Dam, T. F. Oostendorp, A. C. Linnenbank, and A. van Oosterom. Non-invasive imaging of cardiac activation and recovery. *Ann Biomed Eng*, 37(9):1739–1756, Sep 2009.

[75] C. Jamison, C. Navarro, C. Turner, J. Shannon, J. Anderson, and J. Adgey. The inverse problem utilizing the boundary element method for a nonstandard female torso. *IEEE Trans Biomed Eng*, 58(4):876–883, Apr 2011.

[76] J. Xu, A. R. Dehaghani, F. Gao, and L. Wang. Noninvasive transmural electrophysiological imaging based on minimization of total-variation functional. *IEEE Trans Med Imaging*, 33(9):1860–1874, Sep 2014.

[77] R. C. Barr, L. W. Nolte, and A. E. Pollard. Bayesian quantitative electrophysiology and its multiple applications in bioengineering. *IEEE Rev Biomed Eng*, 3:155–168, 2010.

[78] R. O. Martin, T. C. Pilkington, and M. N. Morrow. Statistically constrained inverse electrocardiography. *IEEE Trans Biomed Eng*, 22(6):487–492, Nov 1975.

[79] R. C. Barr and M. S. Spach. Inverse calculation of QRS-T epicardial potentials from body surface potential distributions for normal and ectopic beats in the intact dog. *Circ. Res.*, 42(5):661–675, May 1978.

[80] D. S. Khoury, B. Taccardi, R. L. Lux, P. R. Ershler, and Y. Rudy. Reconstruction of endocardial potentials and activation sequences from intracavitary probe measurements. Localization of pacing sites and effects of myocardial structure. *Circulation*, 91(3):845–863, Feb 1995.

[81] B. He. Non-invasive imaging of cardiac electric activity. In *Engineering in Medicine and Biology Society, 1998. Proceedings of the 20th Annual International Conference of the IEEE*, pages 10–12 vol.1, Oct 1998.

[82] A. van Oosterom. The use of the spatial covariance in computing pericardial potentials. *IEEE Trans Biomed Eng*, 46(7):778–787, Jul 1999.

[83] A. van Oosterom. *The spatial covariance used in computing the pericardial potential distribution*, pages 1–50. WIT, U.K., 2001.

[84] F. Greensite. A new treatment of the inverse problem of multivariate analysis. *Inverse Problems*, 18(2):363–379, 2002.

[85] B. Erem, J. Coll-Font, R. M. Orellana, P. Štovíček, and D. H. Brooks. Using transmural regularization and dynamic modeling for noninvasive cardiac potential imaging of endocardial pacing with imprecise thoracic geometry. *IEEE Trans Med Imaging*, 33(3):726–738, Mar 2014.

[86] Y. Serinagaoglu, D. H. Brooks, and R. S. MacLeod. Bayesian solutions and performance analysis in bioelectric inverse problems. *IEEE Trans Biomed Eng*, 52(6):1009–1020, Jun 2005.

[87] Y. Serinagaoglu, D. H. Brooks, and R. S. MacLeod. Improved performance of Bayesian solutions for inverse electrocardiography using multiple information sources. *IEEE Trans Biomed Eng*, 53(10):2024–2034, Oct 2006.

[88] Y. Zhang, A. Ghodrati, and D. H. Brooks. Analysis of spatial-temporal regularization methods for linear inverse problems from a common statistical framework. In *Biomedical Imaging: Nano to Macro, 2004. IEEE International Symposium on*, pages 772–775 Vol. 1, April 2004.

[89] O. Dössel, Y. Jiang, and H. W. Schulze. Localization of the origin of premature beats using an integral method. *Int J Bioelectromagn*, 13(4):178–183, 2011.

[90] A. Rahimi, J. Sapp, J. Xu, P. Bajorski, M. Horáček, and L. Wang. Examining the impact of prior models in transmural electrophysiological imaging: A hierarchical multiple-model Bayesian approach. *IEEE Trans Med Imaging*, 35(1):229–243, Jan 2016.

[91] D. J. C. MacKay. Bayesian interpolation. *Neural Computation*, 4(3):415–447, 1992.

[92] C. A. Brebbia, J. C. F. Telles, and L. C. Wrobel. *Boundary Element Techniques: Theory and Applications in Engineering*, pages 64–70. Berlin: Springer-Verlag, 1984.

[93] A. N. Tikhonov. *Numerical methods for the solution of ill-posed problems*. Mathematics and its applications. Kluwer Academic Publishers, Dordrecht, Boston, 1995.

[94] P. C. Hansen and D. P. O'Leary. The use of the *L*-curve in the regularization of discrete ill-posed problems. *SIAM J Sci Comp*, 14(6):1487–1503, 1993.

[95] P. C. Franzone, L. Guerri, B. Taccardi, and C. Viganotti. Finite element approximation of regularized solutions of the inverse potential problem of electrocardiography and applications to experimental data. *CALCOLO*, 22(1):91–186, 1985.

[96] P. R. Johnston and R. M. Gulrajani. A new method for regularization parameter determination in the inverse problem of electrocardiography. *IEEE Transactions on Biomedical Engineering*, 44(1):19–39, 1997.

[97] M. E. Tipping. The relevance vector machine. *Advances in Neural Information Processing System*, 12:652–658, 2000.

[98] M. E. Tipping. Sparse Bayesian learning and the relevance vector machine. *J Mach Learn Res*, 1:211–244, September 2001.

[99] B. M. Horáček, J. W. Warren, C. J. Penney, R. S. MacLeod, L. M. Title, M. J. Gardner, and C. L. Feldman. Optimal electrocardiographic leads for detecting acute myocardial ischemia. *J Electrocardiol*, 34 Suppl:97–111, 2001.

[100] F. Dawoud, G. S. Wagner, G. Moody, and B. M. Horáček. Using inverse electrocardiography to image myocardial infarction–reflecting on the 2007 PhysioNet/Computers in Cardiology Challenge. *J Electrocardiol*, 41(6):630–635, 2008.

[101] M. D. Cerqueira, N. J. Weissman, V. Dilsizian, A. K. Jacobs, S. Kaul, W. K. Laskey, D. J. Pennell, J. A. Rumberger, T. Ryan, and M. S. Verani. Standardized myocardial segmentation and nomenclature for tomographic imaging of the heart. A statement for healthcare professionals from the Cardiac Imaging Committee of the Council on Clinical Cardiology of the American Heart Association. *Circulation*, 105(4):539–542, Jan 2002.

[102] G. Shou, L. Xia, F. Liu, M. Jiang, and S. Crozier. On epicardial potential reconstruction using regularization schemes with the L1-norm data term. *Phys Med Biol*, 56(1):57–72, Jan 2011.

[103] L. Wang, J. Qin, T. T. Wong, and P. A. Heng. Application of L1-norm regularization to epicardial potential reconstruction based on gradient projection. *Phys Med Biol*, 56(19):6291–6310, Oct 2011.

[104] D. Potyagaylo, W. H. Schulze, and O. Dössel. Local regularization of endocardial and epicardial surfaces for better localization of ectopic beats in the inverse problem of ECG. In *Computing in Cardiology 2014*, volume 41, pages 837–840, Sept 2014.

[105] J. Chamorro-Servent, L. Bear, J. Duchateau, C. Dallet, Y. Coudire, and R. Dubois. Adaptive placement of the pseudo-boundaries improves the conditioning of the inverse problem. In *Computing in Cardiology 2016*, volume 43, pages 705–708, Sept 2016.

[106] Z. F. Issa, J. M. Miiler, and D. P. Zipes. *Clinical Arrhythmology and Electrophysiology*. Saunders, Philadelphia, PA, 2009.

[107] K. C. Man, B. Knight, H. F. Tse, F. Pelosi, G. F. Michaud, M. Flemming, S. A. Strickberger, and F. Morady. Radiofrequency catheter ablation of inappropriate sinus tachycardia guided by activation mapping. *J. Am. Coll. Cardiol.*, 35(2):451–457, Feb 2000.

[108] T. Lewis, J. Meakins, and P. D. White. The excitatory process in the dog's heart. Part I. The auricles. *Phil. Trans. Roy. Soc. Lond. B.*, 205:375–426, 1914.

[109] T. Lewis and M. A. Rothschild. The excitatory process in the dog's heart. Part II. The ventricles. *Phil. Trans. Roy. Soc. Lond. B.*, 206:325–334, January 1915.

[110] G. Ndrepepa, E. B. Caref, H. Yin, N. el Sherif, and M. Restivo. Activation time determination by high-resolution unipolar and bipolar extracellular electrograms in the canine heart. *J. Cardiovasc. Electrophysiol.*, 6(3):174–188, Mar 1995.

[111] M. S. Spach, W. T. Miller, E. Miller-Jones, R. B. Warren, and R. C. Barr. Extracellular potentials related to intracellular action potentials during impulse conduction in anisotropic canine cardiac muscle. *Circ. Res.*, 45(2):188–204, Aug 1979.

[112] G. Huiskamp and F. Greensite. A new method for myocardial activation imaging. *IEEE Trans Biomed Eng*, 44(6):433–446, Jun 1997.

[113] B. Tilg, G. Fischer, R. Modre, F. Hanser, B. Messnarz, M. Schocke, C. Kremser, T. Berger, F. Hintringer, and F. X. Roithinger. Model-based imaging of cardiac electrical excitation in humans. *IEEE Trans Med Imaging*, 21(9):1031–1039, Sep 2002.

[114] B. Taccardi, B. B. Punske, R. L. Lux, R. S. MacLeod, P. R. Ershler, T. J. Dustman, and Y. Vyhmeister. Useful lessons from body surface mapping. *J. Cardiovasc. Electrophysiol.*, 9(7):773–786, Jul 1998.

[115] R. Dubois, S. Labarthe, Y. Coudière, M. Hocini, and M. Haïssaguerre. Global and directional activation maps for cardiac mapping in electrophysiology. In *2012 Computing in Cardiology*, pages 349–352, Sept 2012.

[116] D. P. Wipf and B. D. Rao. Sparse Bayesian learning for basis selection. *IEEE Transactions on Signal Processing*, 52(8):2153–2164, Aug 2004.

[117] E. M. Aliot, W. G. Stevenson, J. M. Almendral-Garrote, F. Bogun, C. H. Calkins, E. Delacretaz, P. Della Bella, G. Hindricks, P. Jais, M. E. Josephson, J. Kautzner, G. N. Kay, K. H. Kuck, B. B. Lerman, F. Marchlinski, V. Reddy, M. J. Schalij, R. Schilling, K. Soejima, and D. Wilber. EHRA/HRS Expert Consensus on Catheter Ablation of Ventricular Arrhythmias: developed in a partnership with the European Heart Rhythm Association (EHRA), a Registered Branch of the European Society of Cardiology (ESC), and the Heart Rhythm Society (HRS); in collaboration with the American College of Cardiology (ACC) and the American Heart Association (AHA). *Heart Rhythm*, 6(6):886–933, Jun 2009.

[118] CIBC. map3d: Interactive scientific visualization tool for bioengineering data. Scientific Computing and Imaging Institute (SCI), Download from: http://www.sci.utah.edu/cibc/software.html, 2016.

[119] S. M. Blanchard, R. J. Damiano, T. Asano, W. M. Smith, R. E. Ideker, and J. E. Lowe. The effects of distant cardiac electrical events on local activation in unipolar epicardial electrograms. *IEEE Trans Biomed Eng*, 34(7):539–546, Jul 1987.

[120] M. S. Spach and P. C. Dolber. Relating extracellular potentials and their derivatives to anisotropic propagation at a microscopic level in human cardiac muscle. Evidence for electrical uncoupling of side-to-side fiber connections with increasing age. *Proc. Natl. Acad. Sci. U.S.A.*, 58(3):356–371, Mar. 1986.

[121] R. N. Ghanem, P. Jia, C. Ramanathan, K. Ryu, A. Markowitz, and Y. Rudy. Noninvasive electrocardiographic imaging (ECGI): comparison to intraoperative mapping in patients. *Heart Rhythm*, 2(4):339–354, Apr 2005.

[122] C. Ramanathan, P. Jia, R. Ghanem, K. Ryu, and Y. Rudy. Activation and repolarization of the normal human heart under complete physiological conditions. *Proc. Natl. Acad. Sci. U.S.A.*, 103(16):6309–6314, Apr 2006.

[123] H. Cochet, Y. Komatsu, F. Sacher, A. S. Jadidi, D. Scherr, M. Riffaud, N. Derval, A. Shah, L. Roten, P. Pascale, J. Relan, M. Sermesant, N. Ayache, M. Montaudon, F. Laurent, M. Hocini, M. Haïssaguerre, and P. Jaïs. Integration of merged delayed-enhanced magnetic resonance imaging and multidetector computed tomography for the guidance of ventricular tachycardia ablation: a pilot study. *J. Cardiovasc. Electrophysiol.*, 24(4):419–426, Apr 2013.

[124] MUSIC software (multimodality software for specific imaging in cardiology, L'Institut de Rythmologie et de Modélisation Cardiaque, University of Bordeaux, Institut National de Recherche en Informatique et Automatique Sophia Antipolis, Sophia Antipolis, France) is a multi-modal platform using multidetector CT-MR imaging fusion to derive a patient-specific 3D geometry, which provides complementary information on VT substrate. Download from: http://www.u-bordeaux.com/News/MUSIC-A-multimodal-platform-for-comprehensive-cardiac-imaging, 2013.

[125] S. A. Ben-Haim, D. Osadchy, I. Schuster, L. Gepstein, G. Hayam, and M. E. Josephson. Nonfluoroscopic, in vivo navigation and mapping technology. *Nat. Med.*, 2(12):1393–1395, Dec 1996.

[126] C. C. Gornick, S. W. Adler, B. Pederson, J. Hauck, J. Budd, and J. Schweitzer. Validation of a new noncontact catheter system for electroanatomic mapping of left ventricular endocardium. *Circulation*, 99(6):829–835, Feb 1999.

[127] B. Pfeifer, F. Hanser, M. Seger, G. Fischer, R. Modre-Osprian, and B. Tilg. Patient-specific volume conductor modeling for non-invasive imaging of cardiac electrophysiology. *Open Med Inform J*, 2:32–41, 2008.

[128] P. Štóvíček, Š. Havránek, J. Šimek, M. Zborník, M. Mlček, and O. Kittnar. *Isopotential ECG Imaging Correctly Identified Endocardial Ectopic Activation Site in the Case of Arrhythmia from Right Ventricular Outflow Tract*, pages 1965–1968. Springer Berlin Heidelberg, Berlin, Heidelberg, 2010.

[129] T. Berger, B. Pfeifer, F. F. Hanser, F. Hintringer, G. Fischer, M. Netzer, T. Trieb, M. Stuehlinger, W. Dichtl, C. Baumgartner, O. Pachinger, and M. Seger. Single-beat noninvasive imaging of ventricular endocardial and epicardial activation in patients undergoing CRT. *PLoS ONE*, 6(1):e16255, Jan 2011.

[130] E. Wissner, A. M. Saguner, A. Metzner, M. Chmelesky, A. Tsyganov, S. Deiss, T. Maurer, and K. H. Kuck. Radiofrequency ablation of premature ventricular contractions originating from the aortomitral continuity localized by use of a novel noninvasive epicardial and endocardial electrophysiology system. *HeartRhythm Case Rep*, 2(3):255–257, May 2016.

[131] L. Wang, O. A. Gharbia, B. M. Horáček, and J. L. Sapp. Noninvasive epicardial and endocardial electrocardiographic imaging of scar-related ventricular tachycardia. *Journal of Electrocardiology*, pages –, 2016.

[132] B. Rudic, M. Chaykovskaya, A. Tsyganov, V. Kalinin, E. Tulumen, T. Papavassiliu, C. Dosch, V. Liebe, J. Kuschyk, S. Roger, I. El-Battrawy, I. Akin, M. Yakovleva, E. Zaklyazminskaya, A. Shestak, S. Kim, M. Chmelevsky, and M. Borggrefe. Simultaneous Non-Invasive Epicardial and Endocardial Mapping in Patients With Brugada Syndrome: New Insights Into Arrhythmia Mechanisms. *J Am Heart Assoc*, 5(11), Nov 2016.

[133] E. Wissner, A. Revishvili, A. Metzner, A. Tsyganov, V. Kalinin, C. Lemes, A. M. Saguner, T. Maurer, S. Deiss, O. Sopov, E. Labarkava, M. Chmelevsky, and K. H. Kuck. Noninvasive epicardial and endocardial mapping of premature ventricular contractions. *Europace*, 19(5):843–849, May 2017.

[134] D. Potyagaylo, O. Dossel, and P. van Dam. Influence of Modeling Errors on the Initial Estimate for Nonlinear Myocardial Activation Times Imaging Calculated With Fastest Route Algorithm. *IEEE Trans Biomed Eng*, 63(12):2576–2584, Dec 2016.

[135] Y. Salu. Relating the multipole moments of the heart to activated parts of the epicardium and endocardium. *Ann Biomed Eng*, 6(4):492–505, Dec 1978.

[136] D. J. C. MacKay. Bayesian non-linear modelling for the energy prediction competition. *ASHRAE Trans.*, 100(2):1053–1062, 1994.

[137] K. B. Petersen and M. S. Pedersen. *The Matrix Cookbook*. Technical University of Denmark, nov 2012.

[138] Z. Zhang and B. D. Rao. Sparse signal recovery with temporally correlated source vectors using sparse bayesian learning. *IEEE Journal of Selected Topics in Signal Processing*, 5(5):912–926, Sept 2011.

[139] H. L. Waxman and M. E. Josephson. Ventricular activation during ventricular endocardial pacing: I. Electrocardiographic patterns related to the site of pacing. *Am. J. Cardiol.*, 50(1):1–10, Jul 1982.

[140] M. E. Josephson, H. L. Waxman, M. E. Cain, M. J. Gardner, and A. E. Buxton. Ventricular activation during ventricular endocardial pacing. II. Role of pace-mapping to localize origin of ventricular tachycardia. *Am. J. Cardiol.*, 50(1):11–22, Jul 1982.

[141] J. M. Miller, F. E. Marchlinski, A. E. Buxton, and M. E. Josephson. Relationship between the 12-lead electrocardiogram during ventricular tachycardia and endocardial site of origin in patients with coronary artery disease. *Circulation*, 77(4):759–766, Apr 1988.

[142] D. L. Kuchar, J. N. Ruskin, and H. Garan. Electrocardiographic localization of the site of origin of ventricular tachycardia in patients with prior myocardial infarction. *J. Am. Coll. Cardiol.*, 13(4):893–903, Mar 1989.

[143] M. E. Josephson and J. M. Miller. Endocardial and epicardial recordings. Correlation of twelve-lead electrocardiograms at the site of origin of ventricular tachycardia. *Ann. N. Y. Acad. Sci.*, 601:128–147, 1990.

[144] A. Sippensgroenewegen, H. Spekhorst, N. M. van Hemel, J. H. Kingma, R. N. Hauer, J. M. de Bakker, C. A. Grimbergen, M. J. Janse, and A. J. Dunning. Value of body surface mapping in localizing the site of origin of ventricular tachycardia in patients with previous myocardial infarction. *J. Am. Coll. Cardiol.*, 24(7):1708–1724, Dec 1994.

[145] M. Potse, A. C. Linnenbank, H. A. Peeters, A. SippensGroenewegen, and C. A. Grimbergen. Continuous localization of cardiac activation sites using a database of multichannel ECG recordings. *IEEE Trans Biomed Eng*, 47(5):682–689, May 2000.

[146] O. R. Segal, A. W. Chow, T. Wong, N. Trevisi, M. D. Lowe, D. W. Davies, P. Della Bella, D. L. Packer, and N. S. Peters. A novel algorithm for determining endocardial VT exit site from 12-lead surface ECG characteristics in human, infarct-related ventricular tachycardia. *J. Cardiovasc. Electrophysiol.*, 18(2):161–168, Feb 2007.

[147] M. Yokokawa, T. Y. Liu, K. Yoshida, C. Scott, A. Hero, E. Good, F. Morady, and F. Bogun. Automated analysis of the 12-lead electrocardiogram to identify the exit site of postinfarction ventricular tachycardia. *Heart Rhythm*, 9(3):330–334, Mar 2012.

[148] R Development Core Team. R: a language and environment for statistical computing. R Foundation for Statistical Computing, Vienna, Austria, ISBN 3- 900051-07-0. Available from: http://www.R-project.org/. (Accessed in Sept. 2017), 2010.

[149] C. Kingsford and S. L. Salzberg. What are decision trees? *Nature biotechnology*, 26(9):1011–1013, Dec. 2008.

[150] M. Kuhn. Caret package. *Journal of Statistical Software*, 28(5):1–26, 2008.

[151] V. Vapnik. *Statistical Learning Theory*. Wiley, New York, NY, 1998.

[152] V. Vapnik. *The Nature of Statistical Learning Theory (2nd ed.)*. Springer, New York, NY, 1999.

[153] B. Efron and R.J. Tibshirani. *An introduction to the bootstrap*. Chapman and Hall, New York, 1993.

[154] E. Sosa, M. Scanavacca, and A. d'Avila. Gaining access to the pericardial space. *Am. J. Cardiol.*, 90(2):203–204, Jul 2002.

[155] A. P. Dempster. *Elements of Continuous Multivariate Analysis*. Addison-Wesley Publ. Co., Reading, Mass., 1969.

[156] P. Hansen. Analysis of discrete ill-posed problems by means of the L-curve. *SIAM Rev*, 34:561–580, 1992.

[157] B.M. Horáček. *"Lead Theory". Comprehensive Electrocardiology*. Springer Verlag London, London, England, 2010.

[158] F. Bogun and M. Saeed. Computer-assisted mapping in electrophysiology: are the machines taking over. *JACC: Clinical Electrophysiology*, 3(7):700–702, July 2017.

[159] E. Sosa, M. Scanavacca, A. d'Avila, and F. Pilleggi. A new technique to perform epicardial mapping in the electrophysiology laboratory. *J. Cardiovasc. Electrophysiol.*, 7(6):531–536, Jun 1996.

[160] R. I. Jennrich. *"Stepwise regression", Statistical Methods for Digital Computers*. Wiley-Interscience, New York, NY, 1977.

Appendix A

Dalhousie Standard Models

A.1 Dalhousie Torso Model

A realistic human torso was determined in our laboratory from tomographic measurement of a single subject. The original version was developed by Dr. Horacek. The Dalhousie standard torso consists of 352 nodes, which are vertices of 700 triangular elements of body surface [99, 100]. Fig. A.1 shows a view of our Dalhousie torso model with this coordinate system.

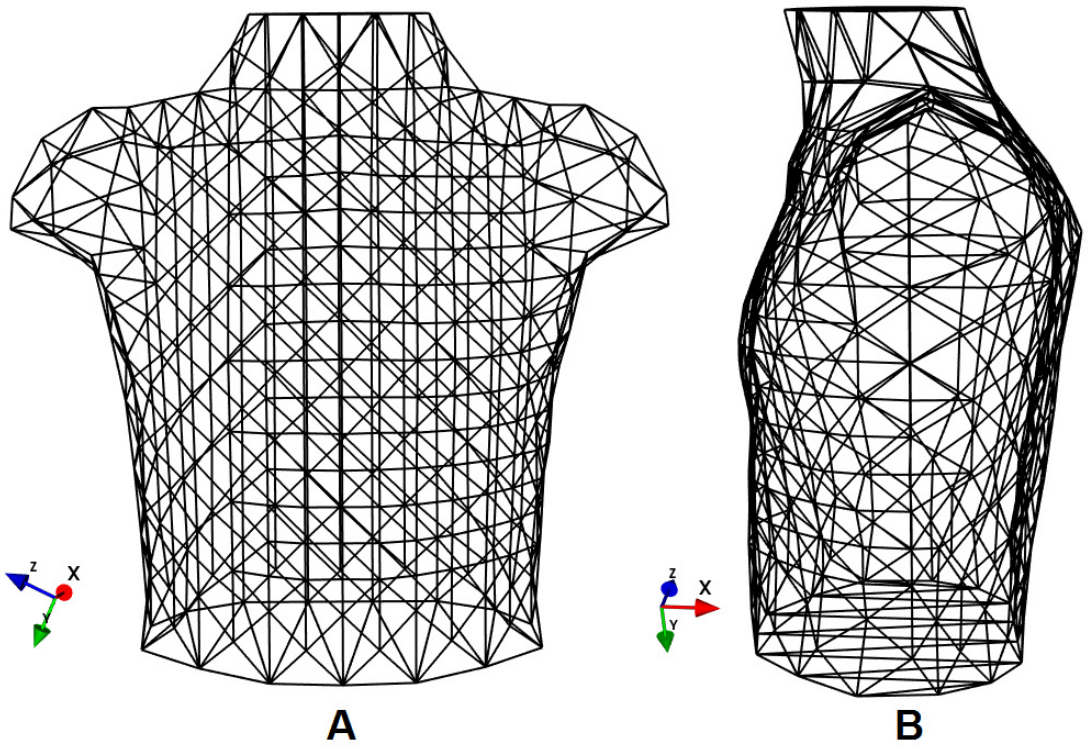

Figure A.1: The 3D Dalhousie standard torso. A: front view of the body surface; B: left-side view of the body surface.

A.2 Heart–A generic left-ventricular model

Detailed 3D geometry of the left-ventricular (LV) endocardial surface was obtained from the necropsy specimen of the normal human heart. A heart specimen was embedded in gelatine, frozen, and sliced whole with a microtome into 1-mm sections, which were photographed and the myocardium boundaries were digitized. The triangulated closed LV endocardial surface–including the aorto-ventricular membrane, mitral valve, and aortic valve–was then constructed. It consists of 305 triangular area elements, 238 of which correspond to the LV endocardium (with trabeculation and papillary muscles ignored) and the remaining triangles close the surface. Fig. A.2 shows a view of open and closed LV endocardial surfaces with coordinate system.

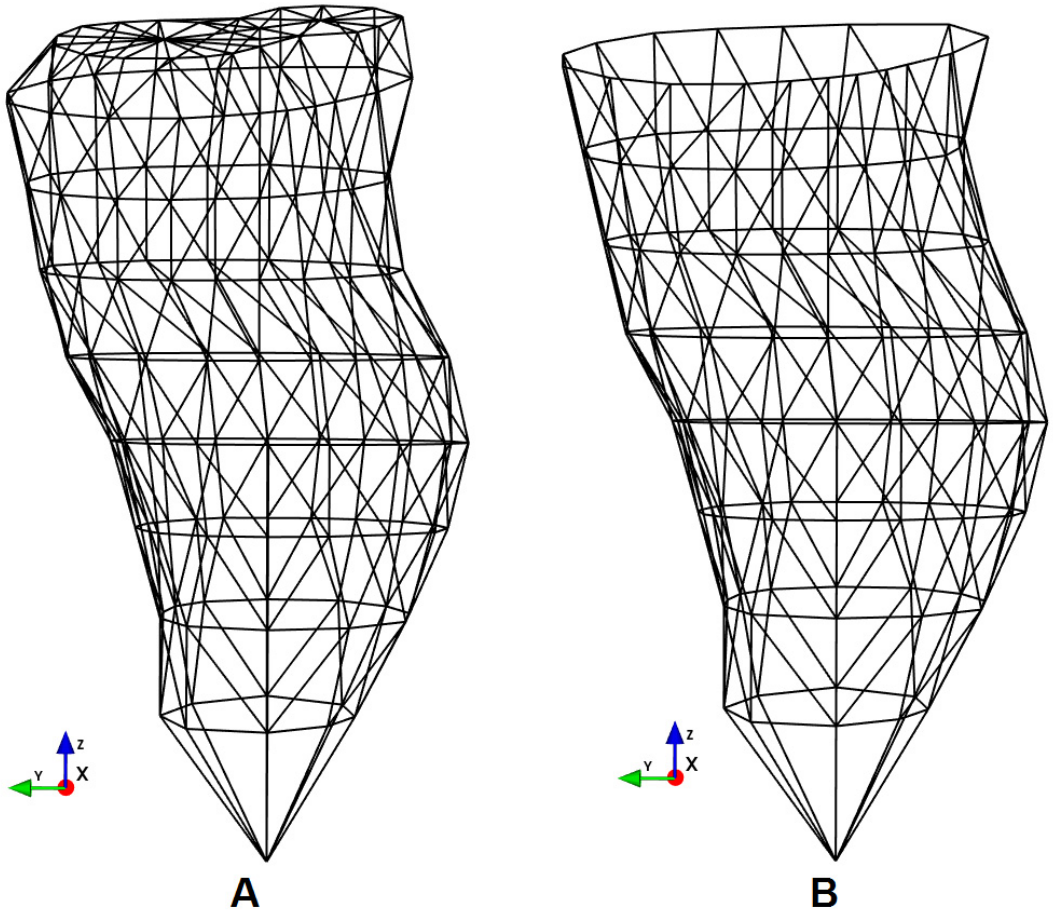

Figure A.2: The 3D generic LV endocardial surface. A: closed generic LV endocardial surface; B: open generic LV endocardial surface.

Appendix B

Dalhousie Standard BSPM

B.1 Data acquisition and processing

To perform electrocardiographic body-surface mapping [99], 18 disposable strips with 120 Ag-AgCl electrodes (FoxMed, Idstein, Germany) were placed on patient's torso and a 128-channel acquisition system (Mark 6, BioSemi, Amsterdam, the Netherlands) with a laptop computer running in-house-developed MAPPER software was used to display and record ECGs. The analog signals were amplified, filtered (0.025 to 300 Hz), sampled at 2000 Hz with 16-bit resolution, recorded for 15 seconds or a sequence of 11-43 consecutive beats during sinus rhythm (SR), ICD pacing, moving catheter pacing, and ventricular tachycardia (VT) for 4 epicardial patients In the 120-lead set, missing leads (due to defibrillation pads) and noisy leads were interpolated into 352 nodes by a three-dimensional interpolation [99], based on the patient-specific torso model. All ECGs were plotted and a representative paced beat for each pacing site was selected for analysis; great care was taken to select a *capture* beat of the best quality from the recording, avoiding motion artifacts, ectopic beats and non-capture beats. The location of each pacing site provided by the electroanatomic mapping system was noted for later off-line analysis and comparison.

Appendix C

Dalhousie Clinical Procedures

C.1 EP Studies Patient Population

C.1.1 Endocardial ablation patients

Study population consisted of patients who suffered from recurrent scar-related VT and underwent catheter-ablation procedure at the electrophysiology (EP) Lab of the Queen Elizabeth II Health Sciences Centre in Halifax, N.S., Canada. The total of 38 patients participated in the study (Table C.1); the first 18 patients underwent 120-lead body-surface potential mapping (BSPM) during catheter ablation procedure and for the next 20 patients only the standard 12-lead ECG was recorded. Before the procedure, standard diagnostic imaging modalities (including echocardiography, angiography, and multigated acquisition scan) were used to locate the site of myocardial scar. All participating patients were informed of the study's procedure, and each gave written informed consent in accordance with the ethical guidelines approved by the institutional Research Ethics Board.

For the purposes of this study, the 3D electroanatomic maps acquired by the Carto© electroanatomic system (Biosense Webster, Diamond Bar, CA, USA) during the ablation procedure were reviewed and 12-lead ECG data corresponding to known left ventricular pacing sites for all patients were pooled. Mean age of these patients was 62 $\pm$ 14 years; 37/38 were male; 77% had ischemic heart disease; 58% underwent previous coronary bypass graft operation; 89% had clinical VT and the remaining 11% had multiple PVCs; mean ejection fraction was 35%. Pacing sites that captured with delay $>$ 40 ms were excluded, because of the possibility of local capture with remote exit; a total of 1,012 LV pacing sites with known coordinates and their corresponding 12-lead ECG constituted a dataset for the present study.

C.1.2 Epicardial ablation patients

The clinical study was approved by the Capital Health Research Ethics Board (Halifax, N.S., Canada), and patients gave written informed consent. The population consisted of

Table C.1: Clinical Characteristics of Patient Population

Pt	Age	Sex	SHD	Prior CV Surgery	Clinical Arrhythmia	EF(%)	AAD	LV Aneurysm
1	77	M	AMI	CABG	SMVT	41	Amiodarone	None
2	59	M	IMI	CABG	SMVT	15	None	None
3	61	M	IMI	CABG	SMVT	25	Amiodarone	None
4	62	M	IMI	CABG	SMVT	43	Sotalol	None
5	53	M	IMI	CABG	SMVT	15	Amiodarone	None
6	60	M	IMI	CABG	SMVT	34	None	Basal inferior
7	81	M	IMI	CABG	SMVT	18	None	None
8	67	M	IMI	None	SMVT	26	Sota+Amio	None
9	61	M	IMI	CABG	SMVT	55	Amiodarone	None
10	49	M	IMI	MVR	SMVT	27	None	None
11	76	M	AMI	CABG	SMVT	25	Sotalol	None
12	26	M	DCM	None	SMVT	40	None	None
13	61	M	AMI	None	SMVT	25	Amiodarone	None
14	43	M	ARVC	None	SMVT	30	Amiodarone	None
15	76	M	IMI	CABG	SMVT	33	Amiodarone	Basal inferior
16	37	M	HCM	Myectomy	SMVT	45	Amiodarone	None
17	66	M	DCM	None	PVCs	45	None	None
18	60	M	VHD	AVR	SMVT	40	Sotalol	None
19	76	F	IMI	CABG	SMVT	42	None	None
20	68	M	MI	CABG	VT	30	None	None
21	59	M	MI	None	SMVT	50	Amiodarone	None
22	46	M	ARVC	None	SMVT	41	Amiodarone	None
23	51	M	MI	None	PVCs	55	None	None
24	74	M	MI	CABG	SMVT	30	Amiodarone	None
25	81	M	MI	CABG/MVR	SMVT	35	Amiodarone	Apical septal
26	71	M	IMI	CABG	PVCs	50	None	None
27	75	M	MI	None	SMVT	40	Amiodarone	None
28	79	M	MI	CABG	SMVT	25	None	None
29	72	M	IMI	CABG	SMVT/storm	30	Sotalol	None
30	78	M	AMI	None	SMVT	15	Amiodarone	Apical & Antsept
31	68	M	IMI	CABG	SMVT	40	Sota+Amio	None
32	47	M	ARVC	None	SMVT	35	Sota+Amio	None
33	66	M	IMI	None	SMVT	30	Sota+Amio	None
34	73	M	MI	CABG	SMVT	30	Sota+Amio	Anterior
35	60	M	None	None	SMVT	60	Sotalol	None
36	63	M	AMI	None	SMVT	49	Amiodarone	None
37	69	M	MI	CABG	SMVT/storm	35	Amiodarone	None
38	80	M	IMI	CABG	SMVT	35	Amiodarone	None

SHD, type of structural heart disease; AMI, anterior myocardial infarction; IMI, inferior myocardial infarction; DCM, dilated cardiomyopathy; ARVC, arrhythmogenic right ventricular cardiomyopathy; HCM, hypertrophic cardiomyopathy; VHD, valvular heart disease; CABG, coronary artery bypass graft; AVR, aortic valve replacement; MVR, mitral valve replacement; SMVT, sustained monomorphic VT; PVCs, premature vetricular complexes.

four patients undergoing epicardial catheter mapping and ablation of VT. Patients underwent CT scanning before the procedure for registration with electroanatomic mapping and generation of patient-specific geometry, and 120-lead BSPM was performed, using our Dalhousie standard methodology [99, 100]. The Dalhousie standard torso consists of 352 nodes [60], which were aligned with the patient-specific locations of the 120 electrodes to customize the standard torso. The clinical data of 4 patients are shown in Table C.2.

Table C.2: Clinical data of VT recordings for the 4 patients

No.	Sex	Age	Etiology	No. of Pacing Sites	Mapped VT	VT Exit/ Ablation Site	CT Slices
1	M	70	CAD	23	VT1	epi. basal inferior LV	0.8
2	M	30	CAD	24	VT2	epi. basal inferior LV	3
3	M	65	CAD	21	VT3	endo. basal inferolat LV	0.8
					VT4	endo. LV mid septum	
4	M	75	CAD	10	VT5	endo. basal lateral LV	0.8
					VT6	endo. basal superior LV	

VT, ventricular tachycardia; CAD, coronary artery disease; CT Slices, thickness of CT slices (mm); epi, epicardial; endo, endocardial; LV, left ventricle.

C.2 EP Studies Protocols

C.2.1 Endocardial electrophysiology study and ablation

Access to the LV was achieved via a retrograde aortic or trans-septal approach. Programmed stimulation for VT induction was done with conventional catheters at two intracardiac sites (RV apex and the RV outflow tract). Intracardiac bipolar and unipolar electrograms were digitized and stored (by CardioLab, GE Healthcare, Piscataway, NJ) and three-dimensional (3D) electroanatomic maps were acquired by the Carto© XP and Carto© 3 systems (Biosense Webster, Diamond Bar, CA, USA). Pace-mapping and entrainment mapping (if possible) were performed as part of the clinical protocol. If VT was inducible and tolerated, a combination of activation and entrainment mapping was used to identify a target for ablation. If the VT was not inducible, non-sustained or hemodynamically unstable, substrate-based mapping and pace-mapping were used to identify parts of scar border targeted for ablation. For focal VTs, ablation was targeted at the site of earliest activation identified by point-by-point mapping. An irrigated 3.5-mm tip deflectable ablation catheter (Thermocool Navistar, Biosense Webster, Diamond Bar, CA, USA) was

used for mapping and ablation. Pacing was performed with stable catheter position at multiple endocardial sites at minimum pacing output that ensured consistent focal myocardial capture. Lesions were created by delivering RF energy at the target sites.

C.2.2 Epicardial electrophysiology study and ablation

In 1996, Sosa and co-workers modified the pericardiocentesis technique to enable percutaneous access to the pericardial space for mapping and catheter ablation of ventricular tachycardia [159]. The same mapping maneuvers described above for endocardial mapping and ablation of ventricular tachycardia are applied in epicardial mapping. During epicardial substrate mapping it has to be considered that low bipolar voltage occurs in areas of epicardial fat accumulation; also, these fat pads limit creation of deep lesions during ablation. Extra precaution has to be taken during epicardial ablation to avoid injury to coronary arteries and veins on the epicardial surface.

Appendix D

Sweep-operator engine

A great variety of statistical computations can be facilitated by the application of a simple operator called the sweep operator, introduced by A.E. Beaton in 1964 [155].

Let $A = (a_{ij})$ be a square matrix whose kth diagonal element $a_{ij} \neq 0$. The result of sweeping A on its kth diagonal element is a new matrix $\tilde{A} = (\tilde{a}_{ij})$of the same size given by:

$$\begin{aligned} \tilde{a}_{kk} &= -1/a_{kk} \\ \tilde{a}_{ik} &= a_{ik}/a_{kk} \\ \tilde{a}_{kj} &= a_{kj}/a_{kk} \\ \tilde{a}_{ij} &= a_{kj} - a_{ik}a_{kj}/a_{kk} \end{aligned} \tag{D.1}$$

for $i \neq k$ and $j \neq k$. A sweep operation can be undone by means of an inverse sweep. The sweep operator can be used to carry out regression computations [160]. The Fortran implementation below illustrates how the sweep operator is used in this project to calculate patient-specific regression coefficients off line. Subroutine doreg.f takes an $8 \times n$ input matrix ($n = 12$, usually), where each row consists of the following string pertaining to the specific pacing site: 1., $area(aVF), area(V1), area(V4), area(V6), Xcarto, Ycarto, Zcarto$, where area variables are time-integrals of respective ECG leads and carto variables are X, Y, Z coordinates of pacing catheter. From this input is computed an 8×8 SCP (Sum of Cross Products) matrix. The first 5 columns are then "swept" by calling subroutine sweep. The SCP matrix is destroyed in the process, but 3 regressions can be extracted from the remains, resulting in a 5×3 matrix of coefficients, where $coef(1, i)$ is an intercept and $coef(2, i)$ through $coef(5, i)$ are slopes for variables $area(aVF), area(V1), area(V4), area(V6)$, respectively, with i running through $Xcarto$, $Ycarto$ and $Zcarto$. The Fortran code shown for illustration below does also other non-essential tasks, to compare results with those obtained by SAS package. A stripped-down and more generalized Java version of subroutine $doreg.f$, used for on-line applications on Android tablet, is listed below Fortran code. It takes an input matrix dimensioned $(nx + ny) \times numRecordings(n \geq 12, usually)$, where each row consists of the string: 1., $(nx - 1)$ measurements, ny measurements. From this is computed an $(nx + ny) \times (nx + ny)$ SCP matrix. The first nx columns are then "swept" by

calling subroutine sweep. The SCP matrix is destroyed in the process, but 3 regressions can be extracted from the remains, resulting in a $3 \times nx$ matrix of coefficients, where $coef[i][0]$ is an intercept and $coef[i][1]$ through $coef[i][nx-1]$ are slopes for the remaining $(nx-1)$ measurements, respectively, with i running from 0 to $(ny-1)$.